Forschungszentrum Karlsruhe
in der Helmholtz-Gemeinschaft

Wissenschaftliche Berichte
FZKA 7362

Muon Production in Extensive Air Showers and Fixed Target Accelerator Data

C. Meurer

Institut für Kernphysik

März 2008

Forschungszentrum Karlsruhe

in der Helmholtz-Gemeinschaft

Wissenschaftliche Berichte

FZKA 7362

Muon production in extensive air showers and fixed target accelerator data

Christine Meurer

Institut für Kernphysik

Von der Fakultät für Physik der Universität Karlsruhe (TH)
genehmigte Dissertation

Forschungszentrum Karlsruhe GmbH, Karlsruhe

2008

Forschungszentrum Karlsruhe GmbH
Postfach 3640, 76021 Karlsruhe

Mitglied der Hermann von Helmholtz-Gemeinschaft
Deutscher Forschungszentren (HGF)

ISSN 0947-8620

urn:nbn:de:0005-073622

Muon production in extensive air showers and fixed target accelerator data

Zur Erlangung des akademischen Grades eines
DOKTORS DER NATURWISSENSCHAFTEN
von der Fakultät für Physik der
Universität Karlsruhe (TH)

genehmigte

DISSERTATION

von

Diplom-Physikerin Christine Meurer
aus Ludwigshafen am Rhein

Tag der mündlichen Prüfung: 29.06.2007

Referent: Prof. Dr. Johannes Blümer

Korreferent: Prof. Dr. Günter Quast

Abstract

The aim of this thesis is to improve the reliability of EAS simulations by investigating the role of hadronic interactions for muon production. The importance of low energy interactions is studied and it is argued that current fixed target experiments can help to reduce uncertainties in the low energy range. This is demonstrated by analyzing data of the CERN fixed target experiment HARP on proton and pion interactions with a carbon target and by comparing the obtained production spectra with model predictions. The simulation studies of the relevant energies and phase space regions of hadronic interactions in EAS form the basis on the cosmic ray part of a proposal for a new fixed target experiment. Early 2007 the proposal was accepted by CERN and the new NA61 experiment will take first p+C data at 30 GeV in autumn of 2007.

Myonerzeugung in ausgedehnten Luftschauern und niederenergetische Beschleunigermessungen

Das Ziel dieser Arbeit ist die Verbesserung der Zuverlässigkeit von Luftschauer-Simulationen, indem man die Bedeutung von hadronischen Wechselwirkungen untersucht, die für die Myonproduktion relevant sind. Der Einfluss von niederenergetischen Wechselwirkungen wird betrachtet und es wird gezeigt, dass gegenwärtige Fixed-Target-Experimente dazu beitragen können, die Unsicherheiten im Niederenergiebereich zu reduzieren. Dies wird an Hand einer Datenanalyse des Fixed-Target-Experiments HARP am CERN demonstriert. Bei diesem Experiment wurde sowohl ein Proton- als auch Pion-Strahl auf ein Kohlenstoff-Target geschossen. Die aus dieser Analyse gewonnenen Produktionsspektren werden mit Modellvorhersagen verglichen. Die Simulationsstudien der relevanten Energie- und Phasenraumbereiche der hadronischen Wechselwirkungen in Luftschauern bilden die Grundlage für den aus der Astroteilchenphysik motivierten Beitrag eines Antrags für ein neues Fixed-Target-Experiment. Anfang 2007 wurde der Antrag vom CERN genehmigt und das neue Experiment NA61 wird die ersten p+C-Daten bei einer Energie von 30 GeV im Herbst 2007 nehmen.

Contents

1 Introduction

The earth is permanently exposed to an almost isotropic flow of charged particles, called cosmic rays. These particles are the only baryonic matter which reaches the earth from outside our solar system. Cosmic rays provide important information on our Milky Way and even about more distant regions. However, even after more than 90 years after the discovery of cosmic rays, their sources, acceleration mechanisms and propagation is not yet understood. Many astrophysical models of sources of cosmic ray particles and their acceleration processes have been proposed. To distinguish between the different models, energy and elemental composition measurements are of central importance.

The all-particle flux of cosmic rays is relatively well known over a large energy range. However, the investigation of the composition of cosmic rays is much more difficult. Below 10^{15} eV cosmic ray particles are measured directly by balloon and satellite borne experiments. Above this energy the particle flux becomes so low that large detection areas on the surface of the earth are necessary. Large array experiments like the KASCADE experiment [1] at the Forschungszentrum Karlsruhe and the Pierre Auger Observatory [2] in Argentina apply an indirect measurement method to study cosmic rays at these energies. They detect secondary particles produced in extensive air showers (EAS), which are initiated by interactions of cosmic ray particles with air nuclei (nitrogen or oxygen) in the earth's atmosphere. For example, a proton with an energy of 10^{15} eV produces an EAS of more than one million secondary particles. Three components of EAS can be distinguished: the hadronic component (pions, kaons, nucleons), the muonic component and the electromagnetic component (photons, electrons and positrons).

One method to derive the energy and particle type of a primary particle of an EAS is to identify muons and electrons separately on the ground. Especially the number of muons in an EAS is an important observable to infer the particle type and the energy of the primary particle. Due to the fact that muons are decay products of mesons and decouple from the shower cascade, they are very sensitive to the characteristics of the hadronic component and to the primary particle type. An additional method is the detection of fluorescence light emitted by interactions of charged particles with nitrogen molecules in the atmosphere.

To derive information on the primary cosmic ray particle from the measured secondary particles at the ground, detailed EAS simulations are necessary. Quantum Chromodynamics (QCD), the theory of the strong force, does not provide a framework for analytical calculations of the hadronic interactions in an EAS. Instead various kinds of phenomenological models with many free parameters have to be applied in EAS simulations. To improve the reliability of the model predictions, the models are tuned to describe accelerator data. In modern EAS experiments, the modeling of hadronic interactions in simulations of EAS is the main source of systematic uncertainty and, therefore, the interpretation of EAS data depends strongly on the applied simulation models.

For example, KASCADE measurements of the cosmic ray composition in the energy region of about $3 \cdot 10^{15}$ eV are derived from the electron and muon numbers measured at the ground [3]. In this energy range the decrease of the particle flux with increasing energy becomes stronger, a feature which is called the *knee* in the cosmic ray spectrum. Astrophysical models predict for this behaviour a characteristic change of the elemental composition of cosmic rays. A shift in the elemental composition of cosmic rays to heavier elements at higher energies is expected in this energy range. The model predictions differ on whether this behaviour scales with the particle mass or the charge. Thanks to the very high data statistics and high data quality of the KASCADE experiment, it should be possible to make a decision on this question. However, dependent on the used hadronic interaction model for simulating reference showers, different results are obtained.

The aim of this thesis is to improve the reliability of EAS simulations by investigating the role of hadronic interactions for muon production. The importance of low energy interactions is discussed and it is argued, that current fixed target experiments can help to reduce uncertainties in the low energy range. This is demonstrated by analyzing data of one fixed target experiment on proton and pion interactions with a carbon target and by comparing the obtained production spectra with model predictions.

The outline of the thesis is as follows. After introducing the astrophysical motivation of EAS measurements in chapter 2, the low energy hadronic interactions are specified which are important for the muon production in EAS. For this study EAS are simulated with a modified version of the simulation package CORSIKA [4]. In particular the energy and the phase space regions of secondary particle production, which are most important for muon production, are investigated in detail and possibilities to measure relevant quantities of hadron production in existing and planned accelerator experiments are discussed (chapter 3).

The fixed target experiment HARP at the PS accelerator at CERN covers the energy and phase space region of importance for muon production in EAS. In the second part

of this thesis, the HARP spectrometer is introduced (chapter 4) and the analysis of momentum spectra of secondary π^+ and π^- in p+C and $\pi^{\pm}$+C collisions at 12 GeV/c is presented in chapter 5. In chapter 6 these data are used to test the predictions of hadronic interaction models for muon production in EAS and the p+C data are compared to very preliminary HARP results on p+N_2 and p+O_2 reactions. A summary and conclusions are given in chapter 7.

2 Cosmic rays and extensive air showers

2.1 Cosmic ray flux

Cosmic ray particles are the only available extrasolar baryonic matter which reaches the earth and can be studied. Therefore the analysis of cosmic ray particles is a key for getting information about distant regions in our galaxy or even from outside of our galaxy. Origin, acceleration, energy and elemental composition of cosmic ray particles are central questions of astroparticle physics today.

One of the main problems of determining the origin of charged cosmic ray particles is the influence of structured as well as irregular magnetic fields in our galaxy and in the intergalactic space on moving charged particles. Therefore cosmic ray particles move on chaotic paths. Any information on their direction is lost and the trajectories do not point back to their sources. Only at ultra-high energies protons with energies of about 10^{20} eV have a very strong magnetic rigidity and they can possibly provide information on their original direction. However, these studies are very hampered by an inadequate statistics of high energetic protons.

In contrast, gamma-rays and neutrinos are not influenced by magnetic fields and hence carry information on their origin. In the energy range up to 100 TeV gamma rays, produced as decay products of particles which interact with accelerated cosmic ray particles in the sources, could be used to detect cosmic ray sources. Favoured sources of cosmic ray particles are supernova explosions, pulsars, active galactic nuclei and quasars, but a proof of this assumption is not yet made.

A common assumption is that the cosmic ray particles gain their energy due to acceleration in the sources [5]. Additionally, an reacceleration of charged particles by interactions with extensive magnetic clouds during their propagation from the sources to the earth is possible. The favoured model for energy gaining processes is acceleration by magnetic shock fronts in supernova remnants [6]. To accelerate particles

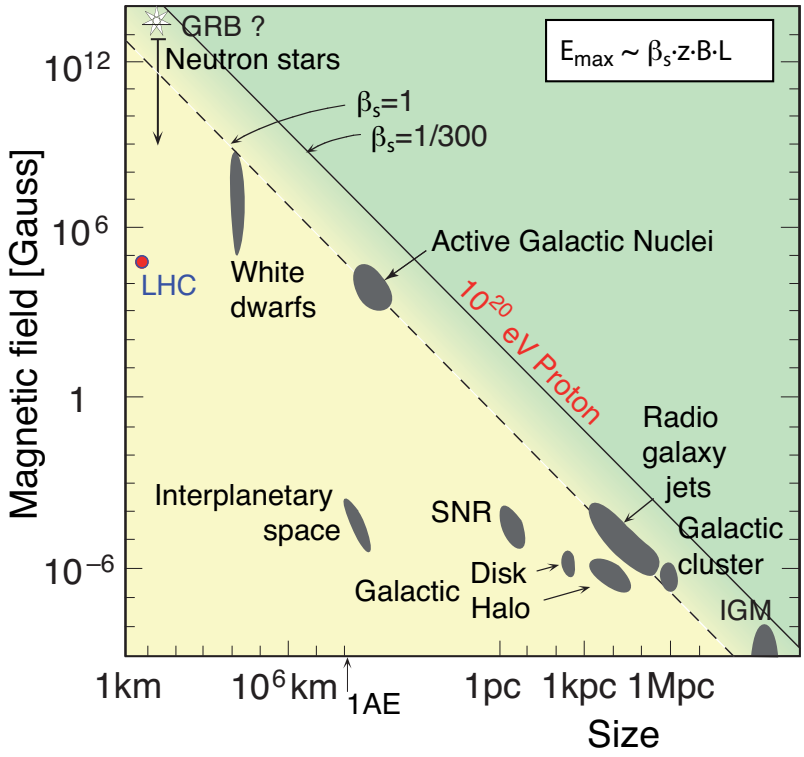

Figure 2.1: Relation of magnetic field strength in possible cosmic ray sources and the size of the corresponding acceleration region [9, 10]. For comparison the characteristics of the large hadron collider (LHC) at CERN are added.

they have to be confined into some 'acceleration region'. Considering the acceleration mechanism by relativistic shock waves similar to the process in supernova explosions the maximum acceleration energy of a particle with charge Z is given by

$$E_{\max} \;\cong\; 10^{18}\,\mathrm{eV}\;\; Z\beta \left(\frac{R}{\mathrm{kpc}}\right)\left(\frac{B}{\mu\mathrm{G}}\right) \quad , \tag{2.1.1}$$

where β is the shock velocity in units of c, B is the magnetic field strength in the source and R the size of the acceleration region. The relation between magnetic field in the source and size of acceleration region for various possible sources is shown in Fig. 2.1. All possible source objects are below the diagonal line and are not able to accelerate protons up to 10^{20} eV. Supernova remnants (SNR), for example, are believed to provide proton acceleration up to 10^{15} eV [7]. Recently, Lucek and Bell [8] proposed a nonlinear magnetic field instability that could explain energies up to 10^{18} eV.

The particle flux (selected measurements) of cosmic rays known to date is shown in Fig. 2.2. The flux is scaled by a factor $E^{2.5}$ to visualize specific structures in the spectrum. The energy range is chosen from 10^{12} eV up to the highest energies of the cosmic rays of about 10^{20} eV. At the lower edge of the energy spectrum particles are

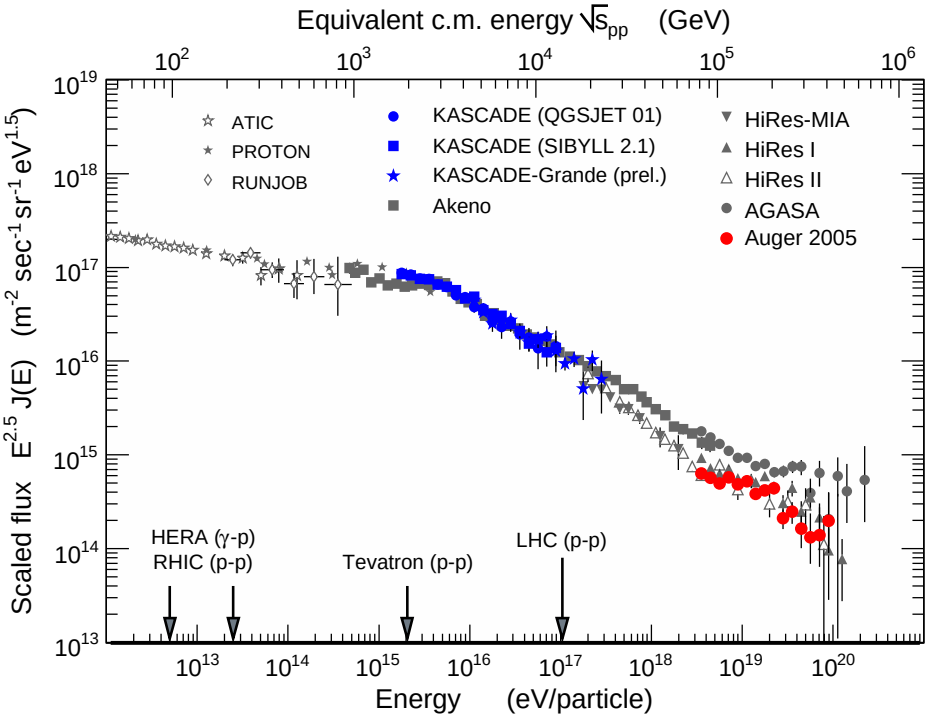

Figure 2.2: Cosmic ray flux scaled by the factor $E^{2.5}$. The measurements from KASCADE, KASCADE-Grande and Auger are highlighted by coloured marks [11, 12, 13, 14].

detected directly by satellite or balloon borne experiments. Since the particle flux becomes very weak at higher energies a large detection area is needed. Therefore, secondary particles, produced in a cascade initiated by an interaction of a cosmic ray particle with an air nucleus of the earth's atmosphere, are measured by large array ground based experiments (see chapter 2.2). The upper scale of the abscissa shows the corresponding center of mass energy of collider experiments. If one keeps in mind that the highest energy reached by accelerators today (Tevatron) is $E_{\text{lab}} = 1.92 \cdot 10^{15}\,\text{eV}$, this gives an impression of the highest energies of the cosmic rays. The spectrum mainly follows a power law, $dN(E)/dE \sim E^{\gamma}$. Three special features of the cosmic ray spectrum are in particular noteworthy. All these structures are characterized by changes in the slope of the spectrum.

The structure at $3 \cdot 10^{15}\,\text{eV}$ is called the *knee*. At this energy the index γ of the power law changes from approximately -2.7 to -3. Two different interpretations of this phenomenon exist and are supported by various models. The possible explanations have in common that the energy where the slope is changing depends on the particle composition of the cosmic rays.

- One class of models assumes a dependence on the charge of the cosmic ray particle. This can be understood in the sense of a rigidity effect. Particles with a small charge number Z (e.g. protons) are less strongly bound in the magnetic field of our galaxy and can easier escape from the galaxy than particles with a larger charge number (e.g. iron nuclei). Additionally, the acceleration process of charged particles is not as efficient for particles with smaller charge number as it is for particles with larger Z. According to this interpretation this leads to a knee structure for iron nuclei at a 26 times higher energy than for protons.

- In contrast, the second class of models predicts a dependence of the knee on the particle mass. These models consider new interaction channels, changes in the characteristics of multiparticle production at these energies, or new energy loss processes. The cannon ball model [15] provides an alternative explanation. This model is based on the assumption that blobs of matter (called cannon balls) are ejected in jets of supernova explosions. Following this idea cosmic ray particles get their energy mainly from elastic scattering. These explanations lead to a knee structure at a 56 times higher energy for iron nuclei than for protons.

At energies above $3 \cdot 10^{18}$ eV the spectrum flattens again. This feature is called the *ankle*. One interpretation of the ankle is the transition from galactic to extragalactic cosmic rays. At these energies particles with small charge number are no longer confined to the galaxy by the magnetic field. Heavier nuclei with larger Z are bound up to higher energies, which leads to an enhancement of heavier particles in the cosmic ray flux at these energies. If the extragalactic composition of cosmic ray particles consists mostly of protons, the transition from galactic to extragalactic cosmic rays results in a transition from heavier to lighter elements.

At ultra-high energies it seems that the cosmic particle flux is suppressed [16]. One possible explanation is the theoretically predicted Greisen-Zatsepin-Kuzmin (GZK) cut-off [17, 18], which describes the inelastic interaction of ultra-relativistic protons with gamma quanta of the 2.7 K cosmic microwave background, whereby the protons lose part of their energy by the production of pions. Alternatively, the suppression of the flux at highest energies could be a consequence of missing sources providing a mechanism to accelerate particles at such high energies, see Fig. 2.1.

To answer these questions about the phenomena behind the structures of the cosmic ray spectrum a detailed study of the elemental composition of the cosmic ray particles at the corresponding energies is necessary. Due to the low particle flux of cosmic rays with energies above 10^{15} eV, the indirect study of cosmic rays by analyzing extensive air showers becomes important at high energies.

2.2 Extensive air showers

If a cosmic ray particle enters the earth's atmosphere, an interaction with a nucleus of an air molecule (mostly nitrogen or oxygen) in the upper atmospheric layers occurs. Hereby many secondary particles are produced, most of them are mesons but also baryons and leptons are produced. The mean free path of these particles depends on their cross-section, their lifetime and the density of the atmosphere. The secondary particles undergo collisions with air nuclei or decay into lighter particles. This leads to a cascade of a multitude of particles. This phenomenon is known as extensive air shower (EAS). In an EAS initiated by a primary proton with an energy of 10^{15} eV, about one million charged secondary particles are produced. The development of particles in an EAS is depending on the relation between the interaction frequency of a particle and its life time. Hereby typically Lorentz factors of about 10^4 to 10^5 have to be considered. The particles in an EAS penetrate the atmosphere with nearly the speed of light while they are concentrated in a slightly parabolic disc of about 1 m thickness near the shower axis. Due to the time delay of multi-scattered particles the thickness of the disc is broader to the outer regions. During shower development through the atmosphere, first the number of particles increases until a maximum number of particles is reached. The shower maximum occurs typically at a height of about 5000 m over sea level for a vertical proton induced shower of 10^{15} eV, whereas the maximum of a 10^{20} eV proton shower can reach the ground at the detection level of the Auger detector array (1500 m). After the shower has reached its maximum the particle production in an EAS is less efficient than the decrease of the number of particles by ionisation energy loss and decays.

Three main components of an EAS are distinguished, the electromagnetic, muonic and hadronic components, which are schematically indicated in Fig. 2.3.

- The hadronic component mainly consists of charged pions as well as of a smaller part of kaons and also baryons, in particular neutrons. In an EAS initiated by an atomic nucleus also fragments of nuclei are part of the hadronic shower component.
- Electrons, positrons and gamma quanta constitute the electromagnetic shower component. The main contribution to the electromagnetic shower component stems from the decay of neutral pions. π^0 mesons have a short life time ($8.4 \cdot 10^{-17}$s [19]) and decay mainly (branching ratio of 98.798% [19]) into two gamma-quanta, which produce electron-positron pairs. An alternative decay channel is $\pi^0 \rightarrow \gamma + e^+ + e^-$. These particles undergo inelastic scattering and produce again gamma-quanta (Bremsstrahlung).
- The muonic shower component is fed by the decay of charged mesons, namely

$\pi^+ \rightarrow \mu^+ \nu_\mu$ (branching ratio of 99.9877% [19]), $K^+ \rightarrow \mu^+ \nu_\mu$ (branching ratio of 63.44% [19]). Muons loose their energy mainly by ionisation processes in the atmosphere and have therefore a long range and many of them reach the ground. Only the low energy muons (few GeV) decay into electrons or positrons and neutrinos ($\mu^- \rightarrow e^- \bar{\nu_e} \nu_\mu$, $\sim 100\%$) and thereby contribute to the electromagnetic component.

Detailed air shower simulations are used to study the various characteristics of EAS. The Monte Carlo based CORSIKA [4] program complex is frequently used for air shower simulations. A detailed description on CORSIKA is given in the additional chapter 2.3.

In Fig. 2.4 a comparison of the electromagnetic and muonic shower component of showers with a primary energy of 10^{19} eV is shown in a longitudinal shower profile as well as in the lateral particle distribution on ground [20]. The total number of shower particles is dominated by the shower electrons. After the shower maximum is reached the electromagnetic component is absorbed much faster than the muonic one. Comparing proton and iron induced showers the larger total number of muons in an iron induced shower might be understandable by the smaller energy per nucleon, that leads to lower energetic pions. This favours a pion decay into muons. However, an additional influence is the fact, that the first interaction of an iron shower happens at higher altitudes, where the density of the atmosphere is smaller. This favours inelastic collisions with air nuclei. Also the lateral distributions of the different shower components of an EAS deviate from each other. Due to the higher altitude of the muon origin muons can reach larger lateral distances on the ground. In contrast, electrons reaching the ground are produced at smaller altitudes. This leads to a flatter lateral distribution for muons than for electrons.

The number of muons and the number of electrons reaching the ground in an EAS are ingredients to infer the type of the primary particle and its energy. The muon component is very sensitive to the characteristics of hadronic interactions. Once the hadronic shower particles have reached an energy at which charged pions and kaons decay, they produce muons which decouple from the shower cascade and hence carry information on hadronic interactions in EAS. Thats why the muonic component is a composition-sensitive observable. The electromagnetic component of a shower is well determined by the altitude of the shower maximum in the atmosphere and in this way by the energy of the primary particle. Due to the electromagnetic cascade, having a short radiation length of $\sim 36\,\mathrm{g/cm^2}$, most of the information on the initial distribution of photons produced in π^0 decays is lost.

An air shower simulation with the implemented low energy hadronic interaction model GHEISHA [21] and the high energy model QGSJET [22] shows the correlation of

electrons and muons depending on the primary particle and energy, see Fig. 2.5. The simulation is done for different primary energies starting from 10^{14}eV up to 10^{19}eV. This is indicated by "islands" in the diagram. This correlation of number of muons and electrons to the properties of the primary particle is used for a main method to extract the primary mass and energy by measuring secondary particles on the ground.

This method is applied by the KASCADE experiment [1] located at the Forschungszentrum Karlsruhe. An array of ground detectors measures muons and electrons separately for each shower by using scintillators below a 10 cm lead layer for measuring muons and scintillators above the layer for electrons. The energy threshold for muons is 250 MeV. KASCADE is designed for measuring EAS in the energy range around the knee ($3 \cdot 10^{15}$ eV). The results of an unfolding analysis of KASCADE data [3] is shown in Fig. 2.6. For some of the five element groups individual knees can be clearly seen. However, no decision can be made concerning the dependence of the knee either on the charge of the primary particle or its mass.

For the unfolding used reference showers are simulated with the Monte Carlo air shower simulation package CORSIKA (see chapter 2.3). The data analysis is done using three different combinations of implemented hadronic interaction models. For the two upper plots the hadronic interaction model GHEISHA is used for energies up to 80 GeV and QGSJET for higher energies. Replacing QGSJET in the simulation for the reference showers with SIBYLL [23, 24] clear differences in the resulting spectra become remarkable (middle plots). However, the analysis is not only dependent on the high-energy hadronic interaction model but also on the low-energy interaction model, what can be seen in the bottom plots. Therefore the high-energy model QGSJET is used and the low-energy models GHEISHA and FLUKA [25], respectively.

A second method to get information about the energy and mass of the primary particle of an EAS is the measurement of the fluorescence light emitted by nitrogen molecules in the atmosphere, which are excited by charged secondary particles in an EAS. The Pierre Auger Observatory in the pampa of Argentina detects the fluorescence light of EAS with a primary energy in the range of 10^{19} eV with four telescope buildings, each housing six mirror segments. The result of this measurement is a longitudinal shower profile shown in Fig. 2.7. In order to interpret this measurements, for this method it is also necessary to have precise and reliable EAS simulations.

Concluding from both methods the largest source of uncertainty in determining the primary mass of cosmic ray particles is the limited knowledge of simulating low-energy as well as high-energy hadronic interactions in EAS.

Furthermore, the comparison of the results of both methods lead to inconsistencies as seen in the measurements of EAS with energies in the ankle region by the HiRes-

MIA Collaboration [27]. The HiRes prototype fluorescence telescope and the MIA muon detector array are operated in coincidence. In Fig. 2.8 the mean depth of the shower maximum and the muon density at 600 m from the shower core at the ground depending on the primary energy are shown. Additionally, the predictions of shower simulations for proton and iron showers are included. Comparing the data with the predictions the behaviour of mean depth of the shower maximum leads to conclusion of a rapid change of the composition at this energy range from a mixture of elements to very light elements. However, looking at the dependence of muon density on the energy, the composition also changes from heavier to lighter elements, but starting at much higher element number and corresponding to elements heavier than iron for the higher end of the energy range.

In order to provide an improvement on the understanding of EAS measurements it is essential first to improve the precision and reliability of the hadronic interaction models used for the simulation of EAS. To tune and modify these models measurements of accelerator experiments are important. However, experiments reaching high energies are collider experiments, which do not cover the phase space of importance (forward direction) for interactions in EAS. Fixed target experiments cover an energy range up to several hundred GeV and have a good acceptance in the forward direction. Therefore, these experiments are suitable for tuning hadronic interaction models at lower energies.

As already mentioned muons carry an important information on hadronic interactions in an EAS and hence provide a contribution of the knowledge on the primary mass and energy. Due to the competition between interaction and decay, most of the muons are decay products of mesons that are particularly produced in low-energy interactions. Recent model studies show that even at ultra-high shower energies (10^{19} eV) the predictions on the lateral distribution of shower particles depend strongly on the applied low-energy interaction model [28, 29], see Fig. 2.9. The deviations of the models are especially large in the prediction of number of muons on the ground and for lateral distances above 500 m. Latter has to receive attention due to limited acceptance at small lateral distances of large array experiments.

2.3 Air shower simulation with CORSIKA

2.3.1 Simulation package CORSIKA

CORSIKA [4] is the world wide most used program package for a detailed Monte Carlo simulation of EAS initiated by cosmic ray particles. CORSIKA generates the hadronic and the muonic components as well as the electromagnetic component of a shower. The user can choose between various primary particle types (proton, light nuclei up to iron, photons, and other particles), the energy and the angle of the primary particle. All particles are propagated through the atmosphere until they interact with a nucleus of an air molecule, unstable particles decay or even reach the detection level or a defined energy threshold, below which they are discarded. For each particle the decision between interaction and decay is made by a random generator chosen from distributions and considering the corresponding probabilities predicted by the implemented models. All decay channels are considered if they have a branching ratio larger than 1%. In order to save computing time it is possible to thin out a shower in such a way, that only a randomly chosen fraction of secondary particles in an EAS is followed and stored.

With CORSIKA, a detailed simulation code modeling most of the physical processes that occur during the shower evolution is available on the market. The magnetic deflexion of the charged particles in the earth‘s magnetic field is considered as well as energy lost by ionization or radiation and multiple scattering of muons in the atmosphere. An additional option is the description of nucleus fragmentation, by default given by a realistic parameterization. Simulations with CORSIKA can also be calculated with total fragmentation and the evaporation of spectator nucleons, but also without any fragmentation.

The earth's atmosphere is by default described by the US standard atmosphere parameterization [30], which is arranged in layers and consists of 78% nitrogen, 21.0% oxygen and 0.9% argon. Additionally, other atmospheric models for different climatic latitudes are implemented. For steeply inclined showers also the curvature of the earth's surface is considered.

The electromagnetic processes are by default described by the EGS4 model [31], which is a full Monte Carlo simulation program based on Quantum Electrodynamics (QED). EGS4 treats all common electromagnetic processes, which are important for such a simulation. For electrons and positrons annihilation, bremsstrahlung, multiple scattering etc. are considered. Gamma-rays may undergo Compton scattering, e^+e^- pair production and photoelectric reactions. Additionally, photo-nuclear interactions

are implemented as well as $\mu^+\mu^-$ pair creation.

Due to the fact that hadronic interactions can not be calculated analytically like the electromagnetic reactions (see section 2.3.2), the CORSIKA user may choose between several phenomenological hadronic interaction models. These models are divided into two classes depending on the energy range, where they can be used. For low energies (typically below 80 GeV) the GHEISHA [21] interaction routines, the FLUKA model [25] and the microscopic UrQMD model [32] are available. Because the uncertainties in hadronic interaction model predictions increase with the energy there exists a larger sample of hadronic interaction models which are optimized for higher energies. These models differ from each other in their approaches and methodical structure. Where HDPM [33] is a pure phenomenological model with low prediction power, QGSJET [22, 34, 35], DPMJET [36] and VENUS [37] are based on the Gribov-Regge theory [38]. In the case of the minijet model SIBYLL [23, 24] the inelastic cross-section is described by the rising number of produced minijets with increasing energy.

In Fig. 2.10 the x_{lab}-distributions of charged pions produced in p+N interactions with a beam energy of 20 GeV (top panel) and 100 GeV (bottom panel) are shown for different hadronic interaction models. x_{lab} is defined as ratio of the secondary particle energy and the maximum reachable energy which corresponds mainly to the beam energy. These distributions differ distinctly for the different models especially at low x_{lab}.

2.3.2 Hadronic multiparticle production and interaction models

Hadronic interactions

The theoretical description of hadronic interactions is based on Quantum Chromodynamics (QCD). The main differences between the quantum field theory of the strong force (QCD) and the field theory of the electromagnetic force (QED) are the differences of their exchange particles and their coupling constants. The exchange particle of the QED is the photon which does not carry electric charge itself. Therefore photons do not interact with each other. This is different for the gluon, the exchange particle of the strong force. Gluons are carrier of one colour charge and one anti-colour charge in such a way that they are colour charge neutral objects. Nevertheless, gluons interact with each other and hence provide the typical characteristics of the strong force. The coupling constants of the QED, α, and of the QCD, α_S, show very different be-

haviours. Where α allows the calculation of electromagnetic processes up to highest energies, α_S makes a calculation of hadronic interactions only possible for extreme high momentum transfer caused by its magnitude and strong energy dependence. But hadronic processes with a small momentum transfer are the dominating processes in extensive air showers.

In accelerator experiments hadronic cross-sections and particle production can only be measured at relatively low energies. The particles with the highest energies, which could be reached in accelerators at the moment, are produced in the Tevatron collider at Fermilab near Chicago with a center of mass energy of $\sqrt{s} = 1.96\,\text{TeV}$ and the laboratory energy $E_{\text{lab}} = 1.92 \cdot 10^{15}\,\text{eV}$, respectively. In the near future a center of mass energy of about $\sqrt{s} = 14\,\text{TeV}$, which is equivalent to $E_{\text{lab}} = 9.8 \cdot 10^{16}\,\text{eV}$, will be reached by the large hadron collider at CERN in Geneva, Switzerland. Nevertheless, this energy is three orders of magnitude lower than the highest energies of cosmic ray particles which produce air showers in the earth's atmosphere. An additional limitation of accelerator measurements is the accessible phase space. Experiments which provide the highest energies are collider experiments and therefore are not able to measure secondary particles in the very forward direction. However, particle production in an EAS is focused in the forward direction. Only fixed target experiments can cover this phase space region. But these experiments use only beam energies of maximal several hundred GeV.

Due to the limitations of QCD calculations it is not possible to reliably extrapolate the results of accelerator measurements to higher energies and in the forward phase space. Additionally, it is not known, if new physical processes are existing or unknown particles are produced at the high energies of air shower interactions.

For the air shower simulations described in chapter 3, the GHEISHA model is implemented as the low energy hadronic interaction model and the QGSJET model is used for the high energetic range. Therefore these two models are described in more detail in the following.

Low energy model GHEISHA

Implemented in the GEANT3 package [39] the GHEISHA model [21] has been used for many years by high energy physicists to simulate their data and to determine the detection efficiency of their detectors. In this way it has become a reference standard for high energy data simulation. GHEISHA is a purely phenomenological model based on the parameterization in energy and mass number of accelerator data. The mainly used data are from p+p collisions and also some from p+A and A+A collisions. Sec-

ondary particle distributions are parameterized in dependence on projectile particle type, target and energy. Proceeding from the used accelerator data the particle distributions and cross-sections are interpolated and extrapolated to further phase space and energy regions. The given application energy range of GHEISHA is from 0.1 GeV to 1000 GeV.

High energy model QGSJET

The hadronic interaction model QGSJET [22, 34, 35] is based on the Gribov-Regge theory [38] and takes into account the production of minijets. The Gribov-Regge theory is a relativistic field theory of quasi-particles called Pomerons. Pomerons are effective exchange particles which carry the quantum numbers of the vacuum. The cross-section as function of energy could be calculated within good agreement with accelerator measurements by the exchange of these particles. In the QGSJET model, an interaction is described by a multi-Pomeron-exchange of super critical Pomerons. Nucleus-nucleus and hadron-nucleus cross-sections are extrapolated from nucleon-nucleon cross-sections by using the Glauber theory [40]. The Glauber formalism takes into account the geometrical distribution of the nucleons in a nucleus and, for example, the complex interaction of a projectile with several nucleons of a target nucleus. Interactions of secondary particles with each other or with spectator nucleons are not considered in the QGSJET model.

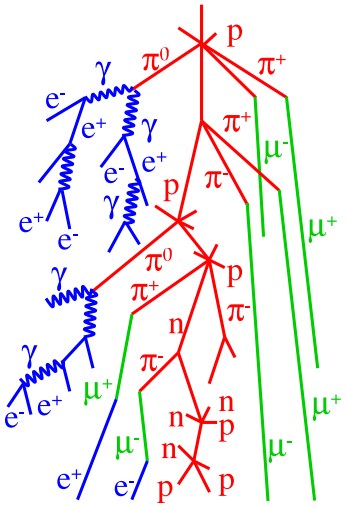

Figure 2.3: Sketch of an extensive air shower. The three different shower components are shown in a schematic way and highlighted by colours (electromagnetic = blue, muonic = green, hadronic = red).

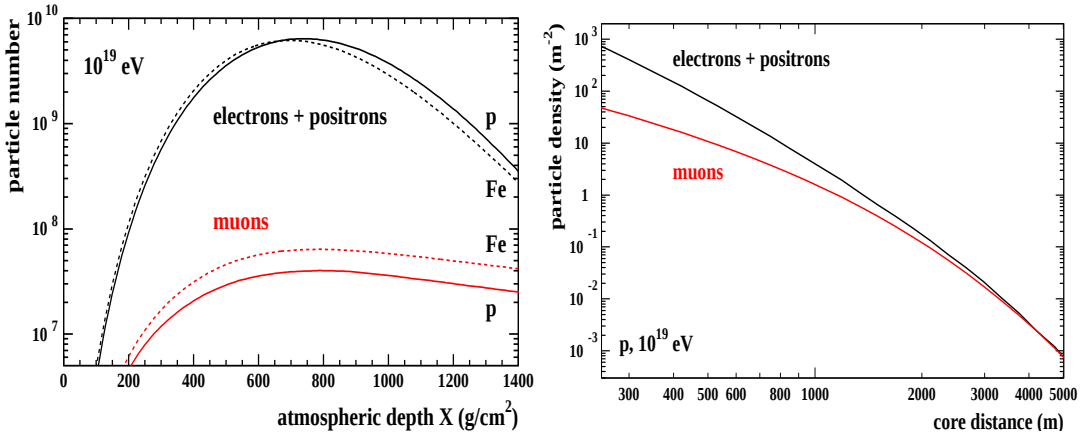

Figure 2.4: Comparison of electromagnetic and muonic shower components [20]. Left panel: longitudinal shower profile of proton and iron induced showers with a primary energy of 10^{19} eV. Right panel: lateral shower particle distribution on ground of a 10^{19} eV proton shower. Shown are the number of electrons with $E_{\mathrm{kin}} \geq 250$ keV and muons with $E_{\mathrm{kin}} \geq 250$ MeV.

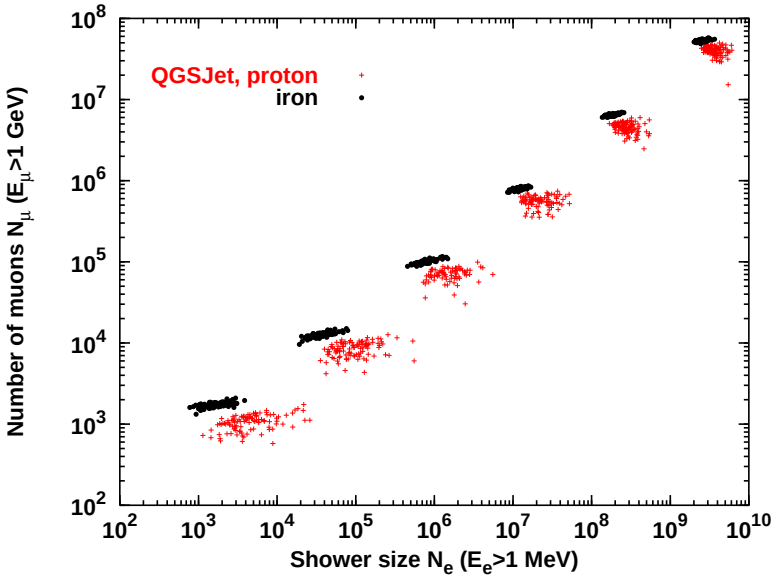

Figure 2.5: Distribution of total muon and electron number on ground for proton and iron induced showers of different primary energies starting from 10^{14}eV (lower left) up to 10^{19}eV (upper right).

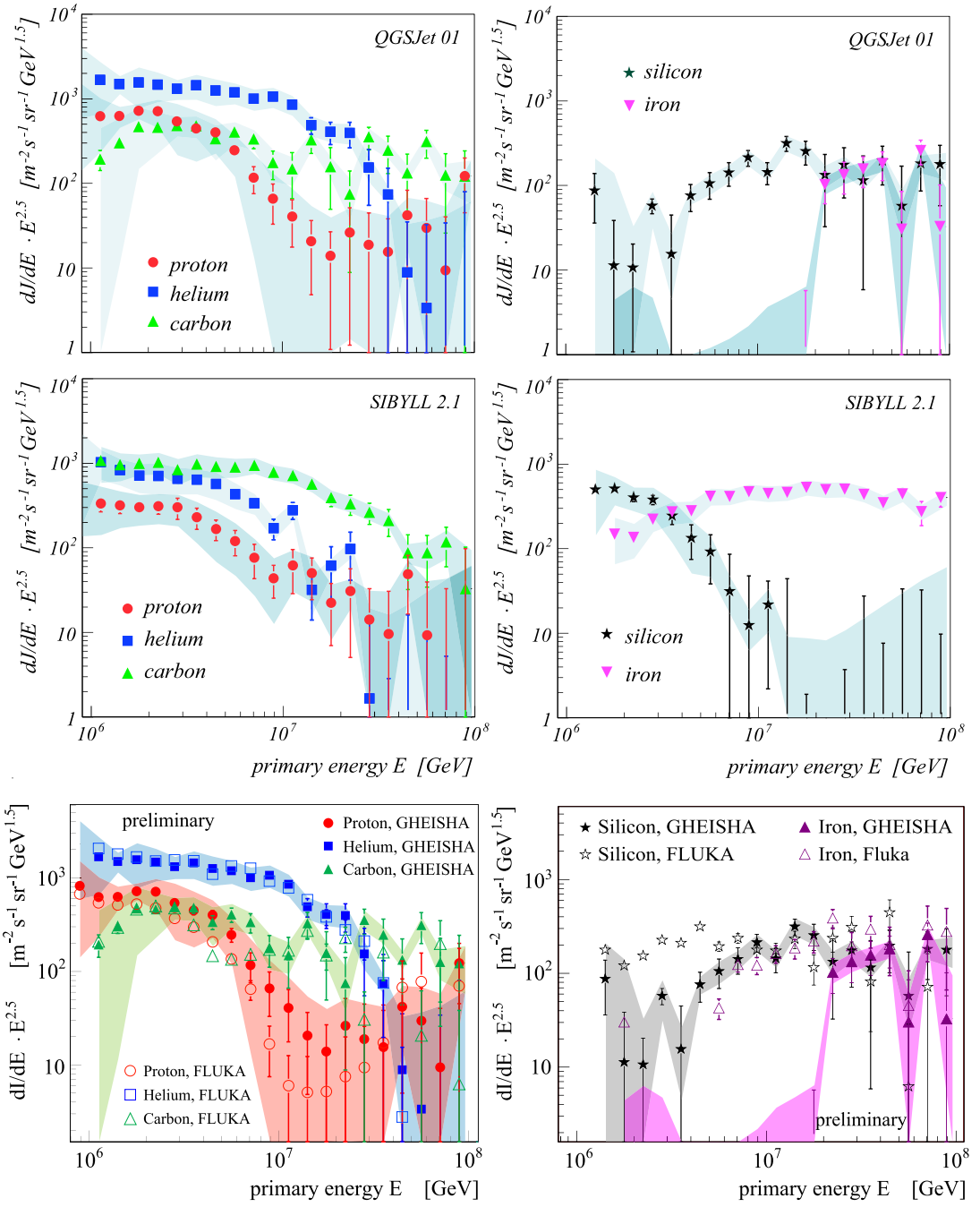

Figure 2.6: Cosmic particle flux for five groups of primary particle types at the knee energy region derived from electron and muon number measured at the ground with the KASCADE shower array [3]. The shaded bands indicate the systematic uncertainty of the unfolding method.

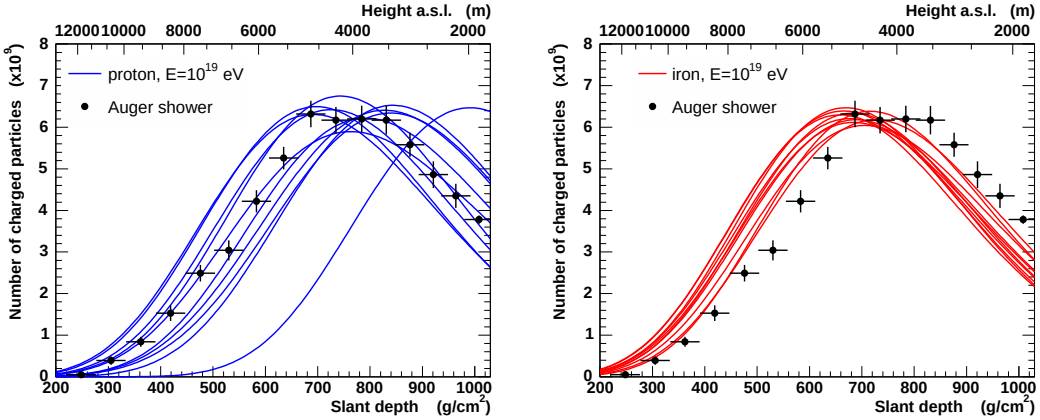

Figure 2.7: Longitudinal shower profile derived from the measurement of the fluorescence light detected by the Auger Observatory [26]. For comparison proton (left panel) as well as iron (right panel) induced showers simulated with CORSIKA (GHEISHA and SIBYLL are implemented) are drawn.

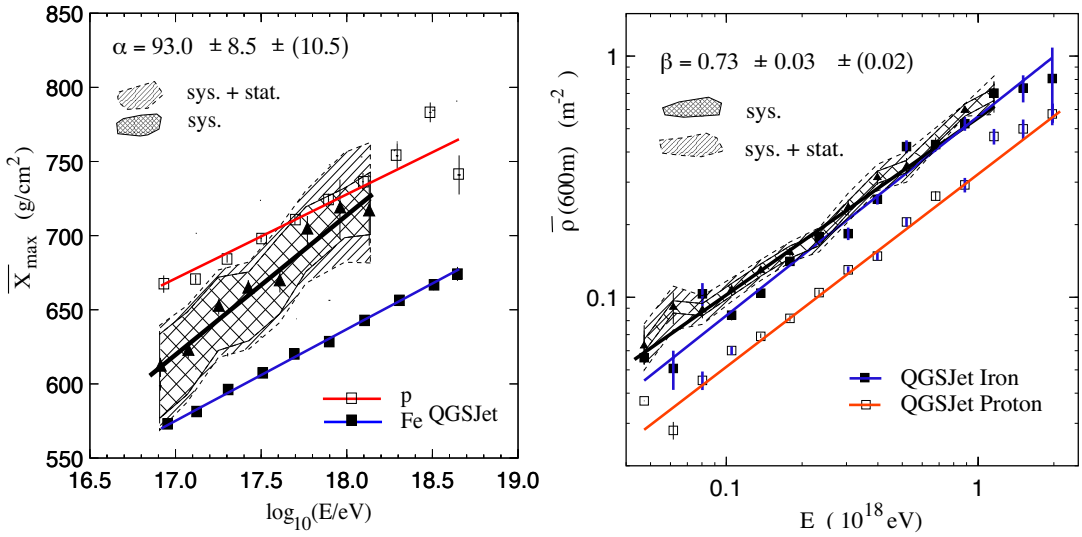

Figure 2.8: Mean depth of shower maximum (left panel) and muon density at 600 m from the shower core (right panel) measured by the HiResMIA collaboration [27]. Additionally, model predictions are included and a fit to the data is indicated by black solid lines.

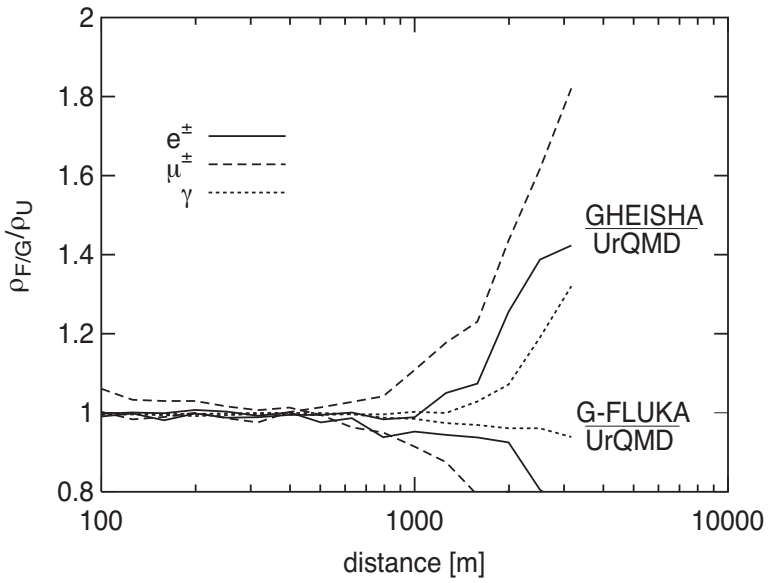

Figure 2.9: Lateral distribution of particle densities for $e^{\pm}$, $\mu^{\pm}$ and γ in a vertical 10^{19} eV proton shower predicted by EAS simulations using either GHEISHA or FLUKA as low-energy hadronic interaction model in relation to the UrQMD model [28]. For energies higher than 80 GeV QGSJET is used.

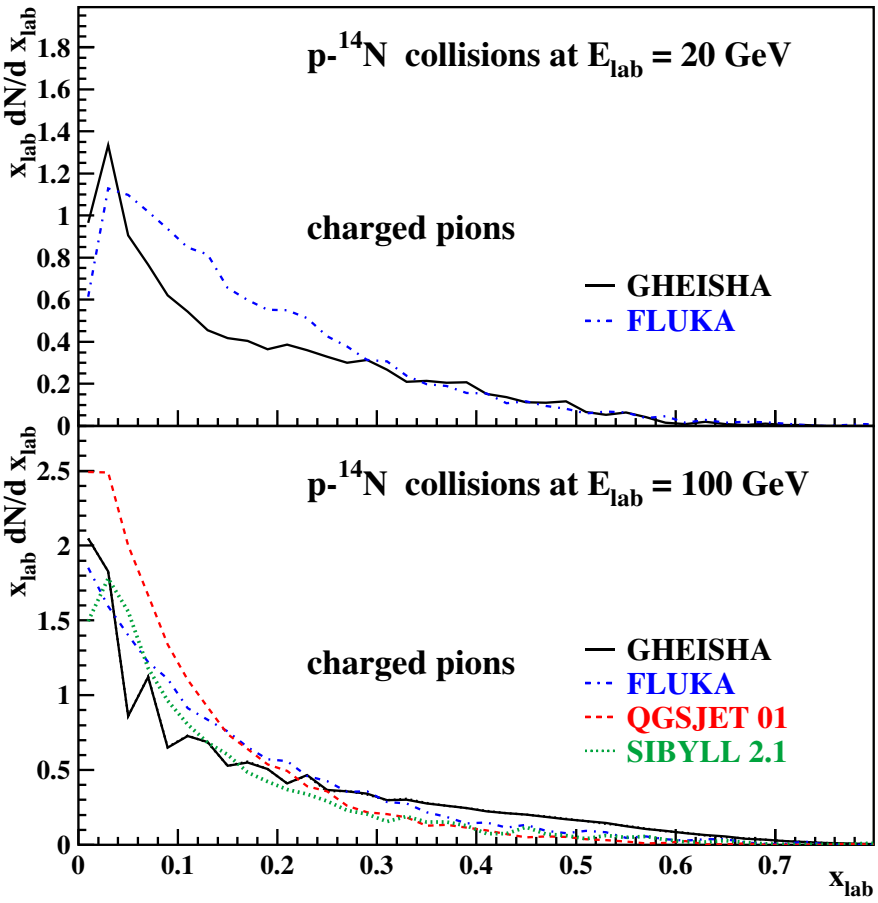

Figure 2.10: Predictions of different hadronic interaction models for pion production in p+N interactions at 20 and 100 GeV lab. energy [29].

3 Muon production in extensive air showers

3.1 General characteristics of muon production

Motivated by the measurement conditions of the KASCADE array [1], showers with a primary energy of 10^{15} eV are considered and a muon detection threshold of 250 MeV is applied. Using a modified version of the simulation package CORSIKA [4] two samples of 1500 vertical and inclined (60°) proton and 500 iron induced showers are simulated. This special version of CORSIKA stores the information of the *last hadronic interaction* where mesons are produced which decay into muons. Below 80 GeV the low-energy hadronic interaction model GHEISHA 2002 [21] and above 80 GeV the high-energy model QGSJET 01 [22] are applied. In this chapter vertical proton induced air showers are considered, but 60° inclined proton showers as well as iron induced showers were also analysed. The results are very similar to that of proton induced vertical showers [41].

First, several general characteristics of the muon production in EAS are investigated to answer the questions where and with what energy the muons are produced in an air shower and where they reach the ground. In the following only those muons are considered that reach the ground level with an energy above the detection threshold.

In Fig. 3.1 the production height of muons, which reach the detection level at different lateral distances (top panel) and with various detection energies (bottom panel) is shown. Many muons are produced in a height of about 5 km above the detection level, which is corresponding with the shower maximum, where most of the particles in an EAS initiated by a 10^{15} eV proton are produced.

But also a lot of muons reaching the ground near the shower center with relatively low energies are generated in a minor height above the detection level. This behaviour could be explained in the sense that close to the detection level many mesons have lost most of their energy and decay into muons.

Energy independent secondary particles produced in hadronic interactions have a typically mean transverse momentum of $p_t \cong 350\,\mathrm{MeV}$. Therefore, muons reaching the ground near the shower center with relatively high energies are produced at high altitudes, whereas muons produced at a similar hight and detected at larger lateral distances have less energy.

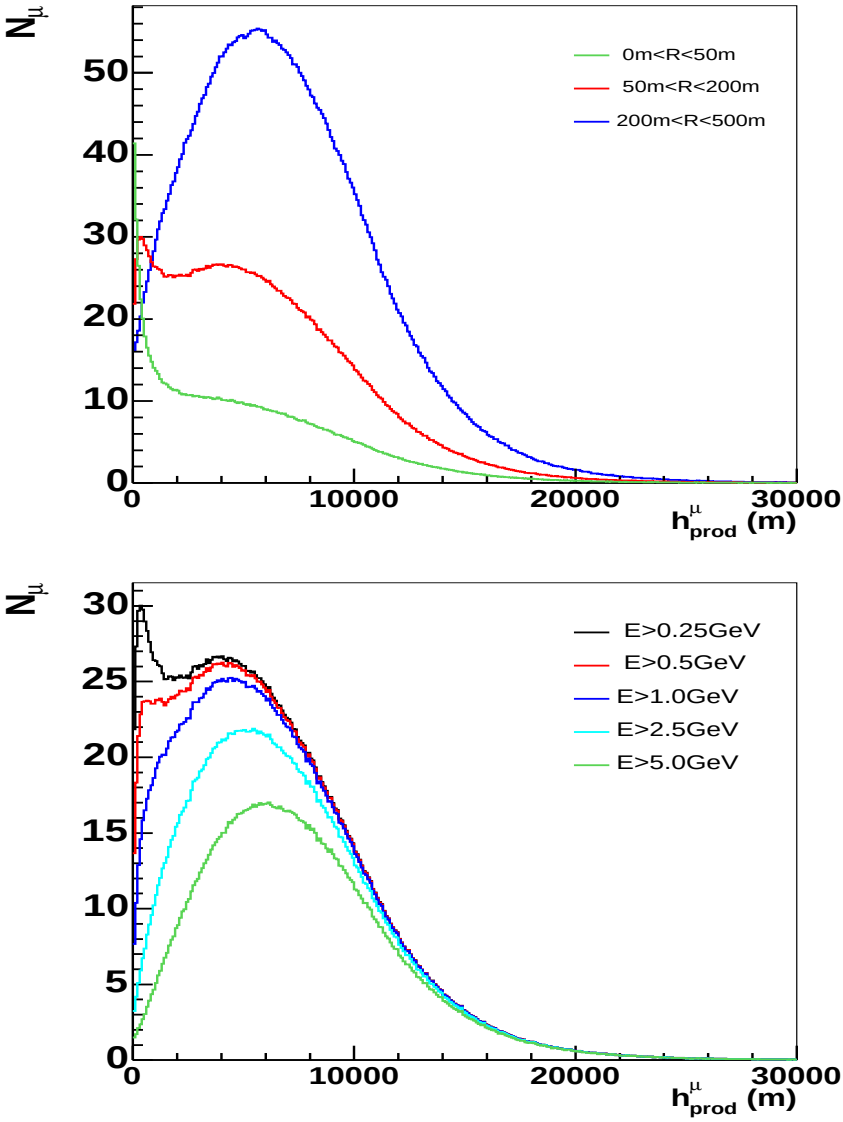

Figure 3.1: Production height of muons for different lateral distance ranges (top panel) and dependent on the muon energy at detection level (bottom panel). For the upper plot a muon energy threshold at detection level of $E > 250\,\mathrm{MeV}$ is assumed. For the bottom plot the muon production height is shown for the limited lateral distance range from 50 m to 200 m apart from the shower center.

Most likely five consecutive hadronic interactions (number of generations) take place before a hadron decays into a muon, see Fig. 3.2 [42]. The number of generations show only a weak dependence on the lateral distance and also on the detection energy of the muon. A weak trend could be noticed that a fewer number of previous hadronic interactions take place for muons in the shower core and also for muons with higher energies. Additionally, it can be mentioned, that the distribution of the number of generations show a long tail to a higher number of generations.

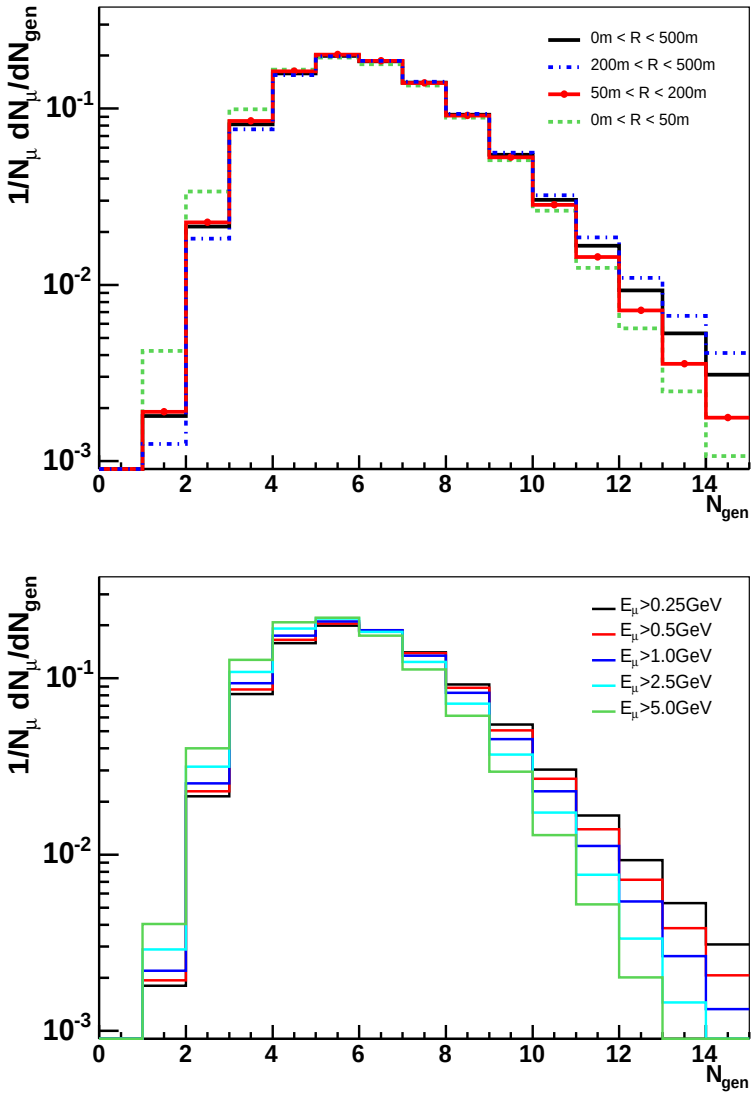

Figure 3.2: Number of generations before producing a muon visible at ground level for various lateral distances (top panel) and for different muon energy thresholds (bottom panel) [42].

To study the hadronic *ancestors* of muons in EAS, the terms *grandmother* and *mother particle* are introduced for each observed muon. The grandmother particle is the hadron inducing the *last* hadronic interaction that finally leads to a meson (mother particle) which decays into the corresponding muon. Fig. 3.3 illustrates the relation of these particles to each other. Most of the grandmother and mother particles are pions, but also about 20% of the grandmother particles are nucleons and a few are kaons. Details of the composition of mother and grandmother particles are given in Tab. 3.1 [41].

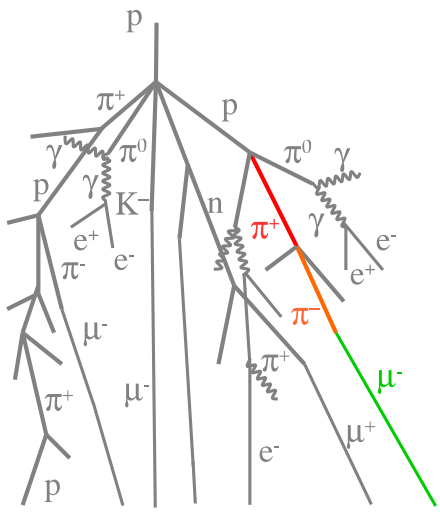

Figure 3.3: Sketch of the air shower development. The coloured particles represent the ancestors (red = grandmother and orange = mother particle) and the decay muon (green), respectively.

Table 3.1: Particle types of mother and grandmother particles in a vertical proton induced shower at 10^{15}eV [41].

	mother	grandmother
pions	89.2%	72.3%
kaons	10.5%	6.5%
nucleons	–	20.9%

In Fig. 3.4 (top) the energy distribution of muons at detector level (1030 g/cm^2) is shown for several lateral distance ranges. The muon energy spectrum has a maximum at energies of approximately 4 to 11 GeV depending on the lateral distance. For lower energies the number of muons on ground is getting smaller, because either muons decay into electrons and neutrinos or their energy is below the detection threshold. In both cases these muons are not counted. Due to the typical transverse momentum

of secondary particles in a hadronic interaction the maximum of the muon energy spectrum shifts to lower energies for larger lateral distances.

The energy spectrum of the mother particles of the muons has a distribution similar to the muon spectrum. In Fig. 3.4 (bottom) the mother energy spectrum is shown for pions as well as for kaons. In average kaons, which decay into muons, have a higher energy than pions as mother particles, due to their shorter life time. Most of the kaons have an energy of about 10 GeV and most of the pions of about 5 GeV. Also the energy fraction given to muons in the decay is important. At low energies, mother particles are not taken into account, if the produced muons either decay or their energy is below the detection threshold. At high energies some mother mesons are lost because they undergo further interactions and do not decay into muons.

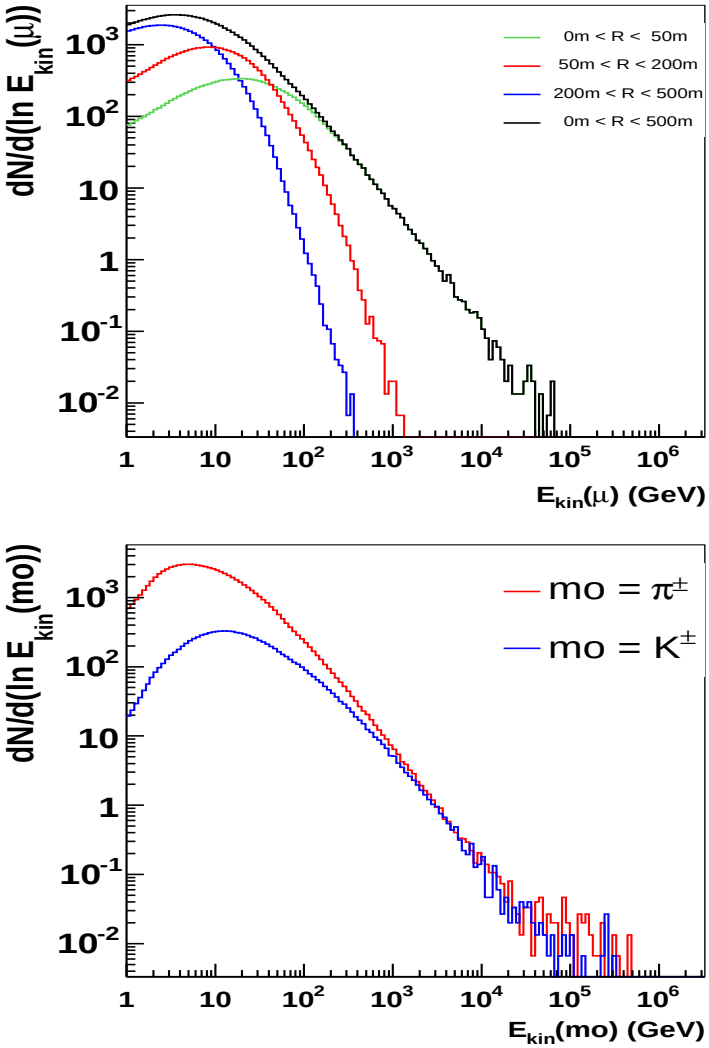

Figure 3.4: Top panel: Energy distribution of muons for different lateral distances. Bottom panel: Energy distribution of pions and kaons as mother particles. Particle type of grandmother particle is not specified.

3.2 Relevant interaction energies and phase space

3.2.1 Energy range

Comparing the *last* interaction in EAS with collisions studied at accelerators, one has to keep in mind that the grandmother particle corresponds to the beam particle and the mother particle is equivalent to a secondary particle produced in e.g. a minimum bias p-N interaction.

The energy spectra of different grandmother particles produced in vertical proton showers are shown in Fig. 3.5 (top). They cover a large energy range up to the primary energy with a maximum at about 100 GeV. The peak at 10^6 GeV in the nucleon energy spectrum shows that also a fraction of muons stems from decay of mesons produced in the first interaction in a shower. Furthermore, the step at 80 GeV clearly indicates a mismatch between the predictions of the low-energy model GHEISHA and the high-energy model QGSJET. In Fig. 3.5 (bottom) the grandmother particle energy spectrum is shown for different ranges of lateral muon distance. The maximum shifts with larger lateral distance to lower energies.

The most probable energy of the grandmother particle is within the range of beam energies of fixed target experiments e.g. at the PS and SPS accelerators at CERN.

3.2.2 Phase space regions

The further study of the relevant phase space of the mother particles is done for two different grandmother energy ranges and muon lateral distance ranges at ground level, see Tab. 3.2. The lateral distance ranges are chosen to resemble typical lateral distances measured at KASCADE and KASCADE-Grande, respectively [13].

Table 3.2: Energy ranges, equivalent average energy and beam rapidity as well as lateral distance ranges used for this analysis.

	energy range	average energy	beam rapidity	lateral distance range
KASCADE	80-400 GeV	160 GeV	5.83	50-200 m
KASCADE-Grande	30-60 GeV	40 GeV	4.45	200-600 m

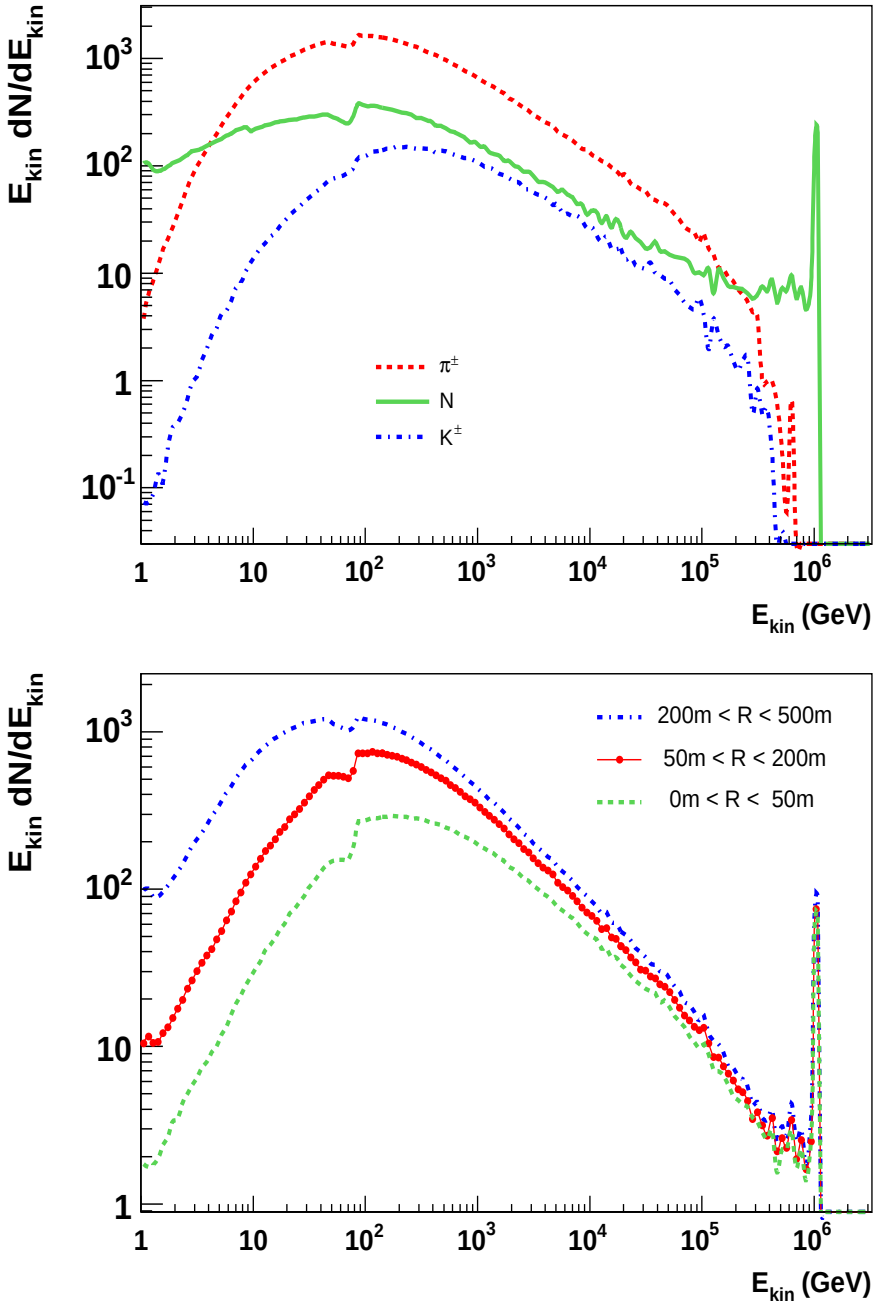

Figure 3.5: Energy distribution of grandmother particles in vertical proton showers [41]. Top panel: different grandmother particle types for a muon lateral distance range of 0-500 m at ground level. Bottom panel: different lateral distances, all particle types are summed up.

For comparison with fixed target experiments the equivalent average energy, corresponding to the beam energy, is given as well as the rapidity y, an observable often used in high energy physics which is defined as

$$y = \ln\left(\frac{E_{\mathrm{tot}} + p_{\mathrm{z}}}{m_{\mathrm{t}}}\right) \quad , \tag{3.2.1}$$

where E_{tot} is the total energy, p_{z} is the momentum component parallel to the beam direction and $m_{\mathrm{t}} = \sqrt{p_{\mathrm{t}}^2 + m^2}$ is the transverse mass and p_{t} the transverse momentum. For the calculation of the beam rapidity the approximation $y_{\mathrm{beam}} \cong \ln(2E_{\mathrm{beam}}/m_{\mathrm{beam}})$ is used.

The reference frame of particle momentum vectors of muons, mother and grandmother particles is chosen in such a way that the momentum vector of the grandmother particle points in z-direction. The momentum vectors are transferred to this system by rotation, where the following matrix is applied to the original momentum vector

$$\begin{pmatrix} \cos\phi & -\sin\phi & 0 \\ \cos\theta\sin\phi & \cos\theta\cos\phi & -\sin\theta \\ \sin\theta\sin\phi & \sin\theta\cos\phi & \cos\theta \end{pmatrix} = \begin{pmatrix} p_y/p_t & -p_x/p_t & 0 \\ p_z p_x/|p|p_t & p_z p_y/|p|p_t & -p_t/|p| \\ p_x/|p| & p_y/|p| & p_z/|p| \end{pmatrix} \quad .$$

This transformation corresponds to a rotation in two steps. First, the momentum vector is rotated around the z-axis with the angle ϕ and in a second step with the angle θ around the x-axis. p_x, p_y and p_z are the momentum components before the rotation, $p_t = \sqrt{p_x^2 + p_y^2}$ the transverse momentum and $|p| = \sqrt{p_t^2 + p_z^2}$ the norm of the momentum vector.

For this analysis the *last* hadronic interactions in EAS are distinguished dependent on the particle type of the grandmother and mother particle. In Fig. 3.6 the rapidity spectra as well as the transverse momentum spectra of different types of mother particles and for different types of grandmother particles are shown. The energy range for grandmother particles and the lateral distance range of muons is chosen to corresponding measurement conditions of KASCADE. In order to compare these rapidity distributions in a next step with simulations of fixed target data, the mother rapidity is divided by the rapidity of the grandmother labeled with y_{beam}. The rapidity spectra do not have a clear dependence on the particle types of mother or grandmother particles. The transverse momentum spectra show a clear dependence on the mother particle type. The transverse momentum spectra for kaons as mother particles are harder than for the pion p_{t}-spectra.

In the following the investigation on the phase space is focused on interactions in EAS initiated by nucleons. In Fig. 3.7 the rapidity spectra of mother particles (top: pions,

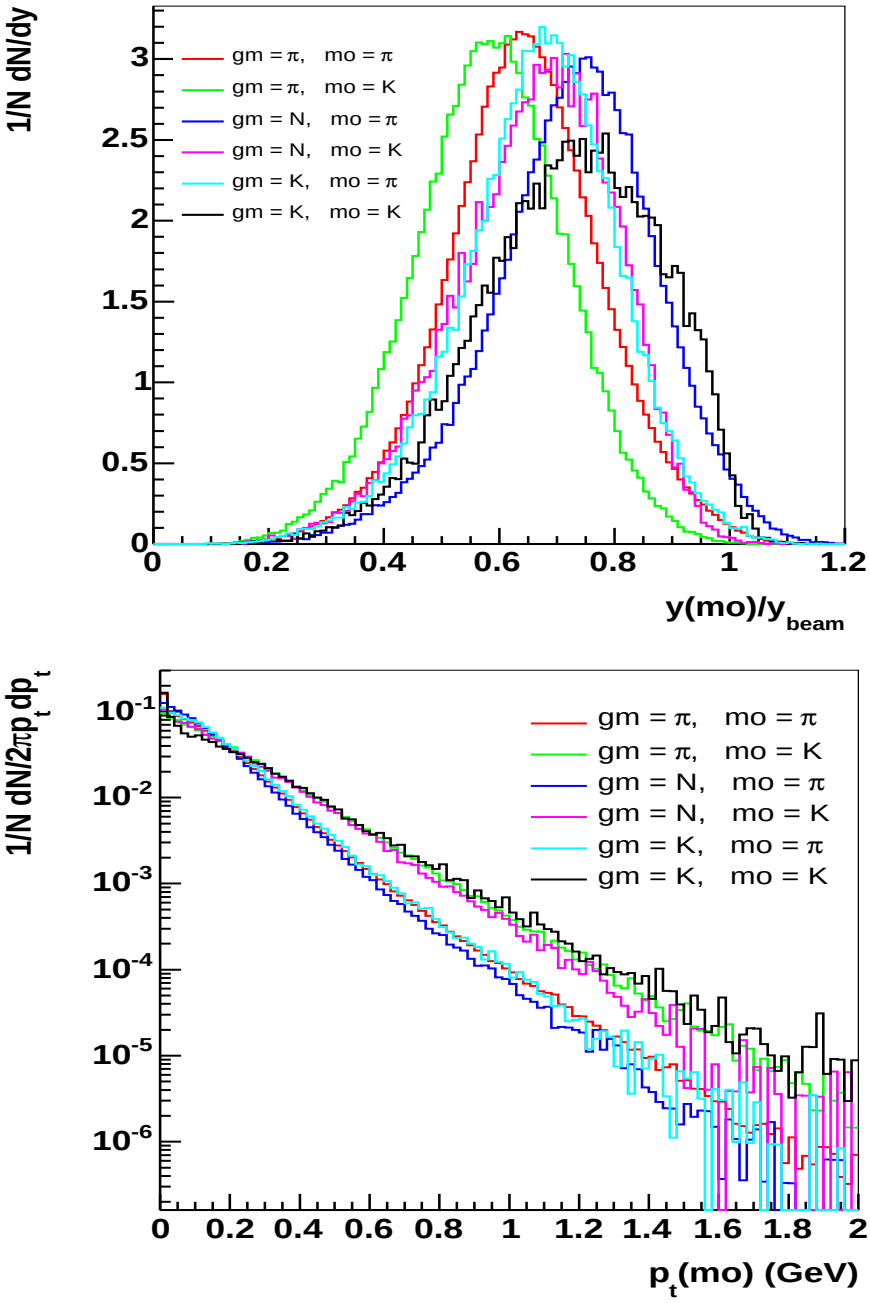

Figure 3.6: Rapidity distributions (top panel) and transverse momentum spectra (bottom panel) of mother particles for different mother and grandmother particle types. Energy range of grandmother particles and lateral distance range of muons are chosen to match experimentally accessible regions of KASCADE.

bottom: kaons) are compared to the spectra of secondary particles of minimum bias proton-carbon and proton-air collisions with a fixed energy simulated with QGSJET labeled as *fixed target*. The rapidity distribution found for the mother particles of muons in EAS are very similar to the rapidity spectra calculated for single particle collisions, if the spectra are scaled to the number of events.

As a consequence of the different selection criteria, the forward hemisphere in the mother rapidity spectra is clearly favoured compared to the spectra of secondaries in minimum bias collisions. The reason for this behaviour is the fact that the secondary particles (pions, kaons) are measured directly in fixed target experiments whereas in EAS an additional condition for the mother mesons is applied. In order to get the information of the mother meson, it has first to decay into a muon which is detectable. At low rapidity the mother mesons are missing in the EAS distribution because the energy of the daughter muon is lower than the applied detection threshold or the muon decays and it is not visible.

The reason for the missing pions in the EAS distribution at the highest rapidities is the interplay between decay and further interactions. High energy pions do not decay but undergo further interactions. This effect is less pronounced for the kaon distribution, because the energy, for which the probability of decay and interaction is of the same order, is much higher for kaons than for pions.

No significant differences are found comparing the rapidity distributions of secondary particles in proton-carbon and proton-air collisions. This is mainly caused by the similar number of nucleons in carbon and air (oxygen, nitrogen) nuclei. Therefore, carbon targets, which are easier to handle in an experimental apparatus, can be used instead of gas or fluid oxygen or nitrogen targets.

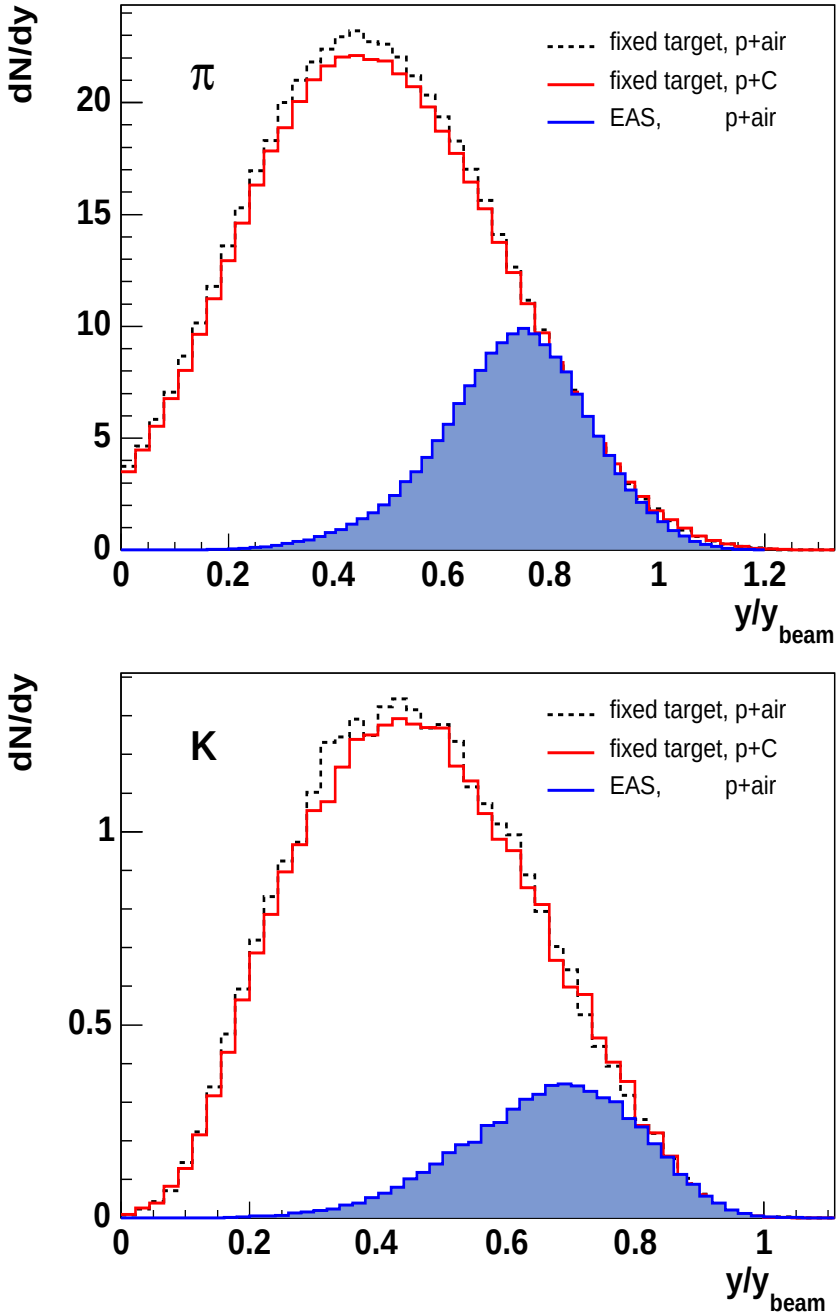

Figure 3.7: Rapidity distributions of mother particles (filled curves) compared with rapidity distributions of secondary particles in simulated single p+C (solid line) and simulated p+air (dashed line) collisions [41]. Top panel: pions, bottom panel: kaons. The energy range of the grandmother particle is limited to 80-400 GeV and the lateral distance of the muons to 50-200 m to match experimentally accessible regions. The fixed target collision simulation is done at 160 GeV, corresponding approximately to the mean grandmother energy. The rapidity is normalized to the rapidity of the beam and grandmother particles, respectively.

In Fig. 3.8 the transverse momentum spectra of pions (top) and kaons (bottom) as mother particles in EAS are compared to p_t-distributions calculated for p+C and p+air single collisions. The p_t-distributions in EAS as well as the spectra for the two versions of single collisions are very similar to each other. Only a small bending of the EAS spectra is visible to larger transverse momentum due to the applied lateral distance cut.

The phase space regions of mother particles produced in the *last* interaction in EAS are shown in Fig. 3.9. As the grandmother particle a nucleon with a mean energy of 160 GeV (Fig. 3.9 (top)) and 40 GeV (Fig. 3.9(bottom)) is chosen, respectively. The transverse momentum of the mother particle is plotted vs. its rapidity divided by the rapidity of the grandmother particle which is equivalent to the beam rapidity in fixed target reactions. On the left hand side these distributions are shown for pions as mother particles, on the right hand side for kaons. The maximum of these distributions, which shows the most important phase space region for the muon production in EAS, is from $p_t \approx 0.1$ GeV to 0.7 in relative rapidity units (for a mean grandmother energy of 160 GeV) and shifts to slightly higher p_t but stays at the same rapidity for a mean grandmother energy of 40 GeV. In both cases the distributions of pions and kaons are similar. For kaons higher particle transverse momenta are more important than for pions. The phase space regions of relevance to EAS are summarized in Tab. 3.3 and indicated with the dashed (red) boxes in Fig. 3.9.

Table 3.3: Phase space regions of hadronic interactions relevant for muon production in EAS [41].

average energy (GeV)	y/y_{beam}	p_t (GeV/c)
160	0.3 - 1.1	0.0 - 0.7
40	0.3 - 1.1	0.0 - 1.0

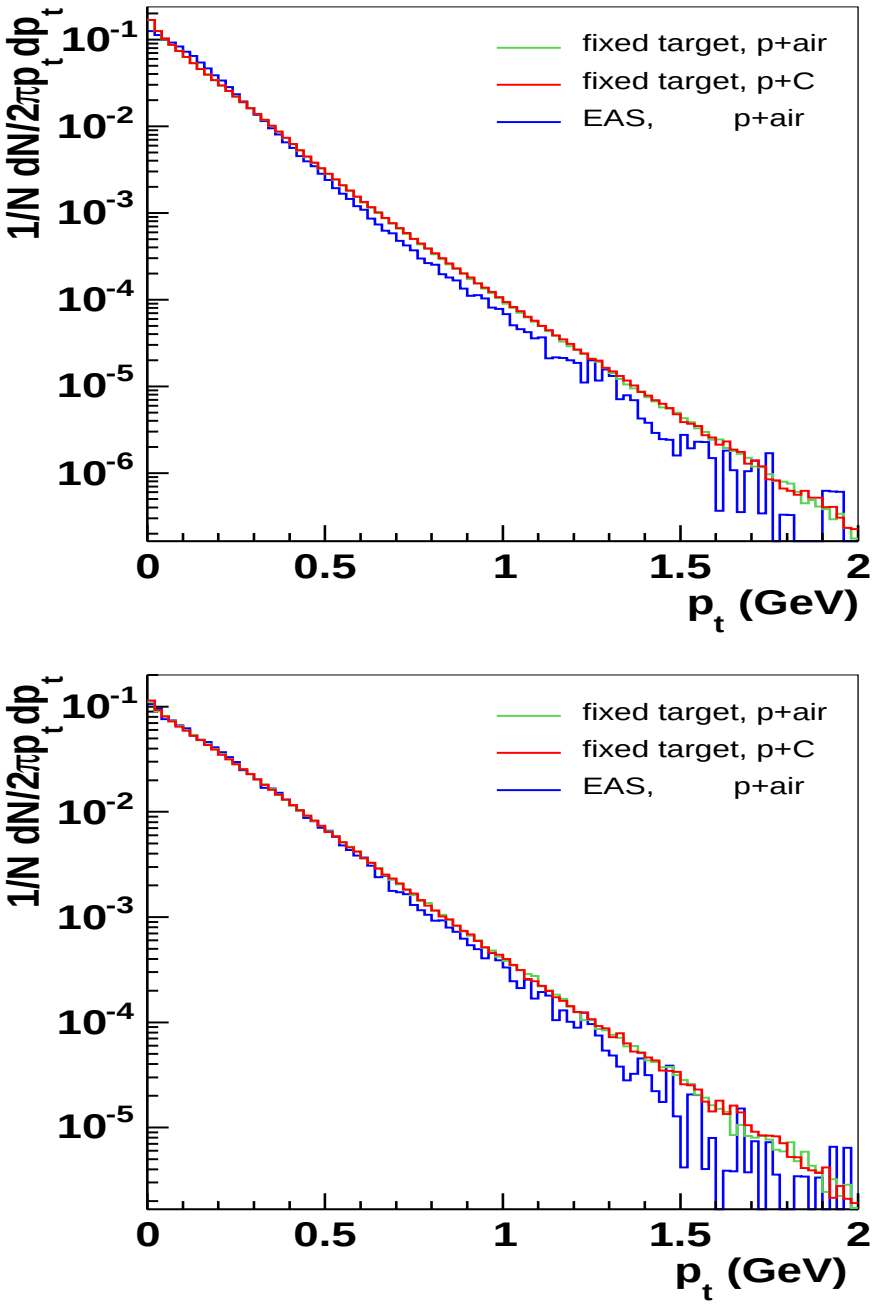

Figure 3.8: Transverse momentum spectra of pions (top panel) and kaons (bottom panel) as mother particles compared to p_t-spectra of secondary particles in p+C and p+air collisions.

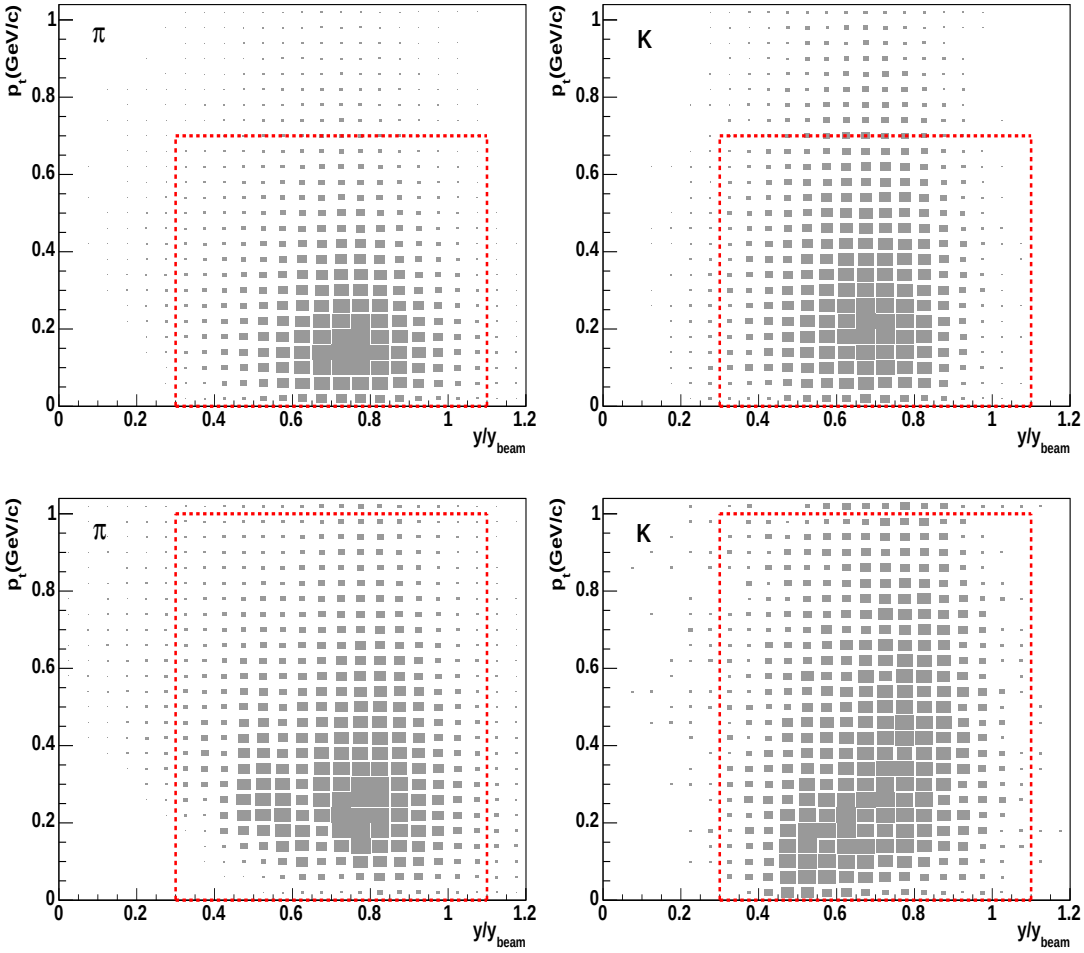

Figure 3.9: Phase space of mother particles [41]. Grandmother energy range: 80-400 GeV (top panels), 30-60 GeV(bottom panels). Left panels: pions, right panels: kaons. The dashed box (red) indicates the most interesting phase space region which includes more than 90% of these particles.

3.3 Phase space coverage of fixed target experiments

In the following the possibility of the experimental accessibility of the energy and phase space regions of most importance for the muon production in EAS is discussed. The results of the simulation studies can be summarized as follows. The beam energy should be in the range of about 10 GeV to 1000 GeV. A reaction of protons or even better pions with light nuclei (similar to oxygen and nitrogen nuclei in the air) should be investigated. The required experiment should be able to measure secondary particles in forward direction and provide a good separation of secondary pions and kaons. On the basis of these requests collider experiments are excluded due to their limitation of measuring particles in very forward direction. Therefore, fixed target experiments are more suitable than collider setups. They cover the lower part of the needed energy range, have a good acceptance in forward direction, especially proton beams are very common (also pion are kaon beams can be extracted by using an additional target) and various kinds of targets also of light nuclei can be inserted in fixed target experiments. The most used light nuclei target is a beryllium target but also a few experiments are using carbon targets which are more comparable with air nuclei than beryllium.

In Fig. 3.10 the relevant phase space for pions produced in reactions in EAS which are initiated by nucleons is shown as box histogram. Only pions which decay to a observed muon are considered. The grandmother momentum is given as abscissa (labeled as p_{beam}) and the mother particle observable as ordinate. On the left hand side the momentum of the mother particle (labeled as p_π) is chosen as mother observable, on the right hand side the mother observable is the angle between mother and grandmother momentum (labeled as θ). The size of the boxes indicates the relative importance of the phase space region.

3.3.1 Existing p+Be data

A number of fixed target measurements with a good phase space coverage are existing for beryllium targets and a proton beam with low energy ($\leq$20 GeV). However, data at higher energy and in particular for pion projectiles are very sparse. A compilation of existing p+Be target data is given covered by the shaded (colored) regions in Fig.3.10 (top), whereas the beam momentum, the secondary momentum range as well as the production angular range are added to the box diagrams for EAS.

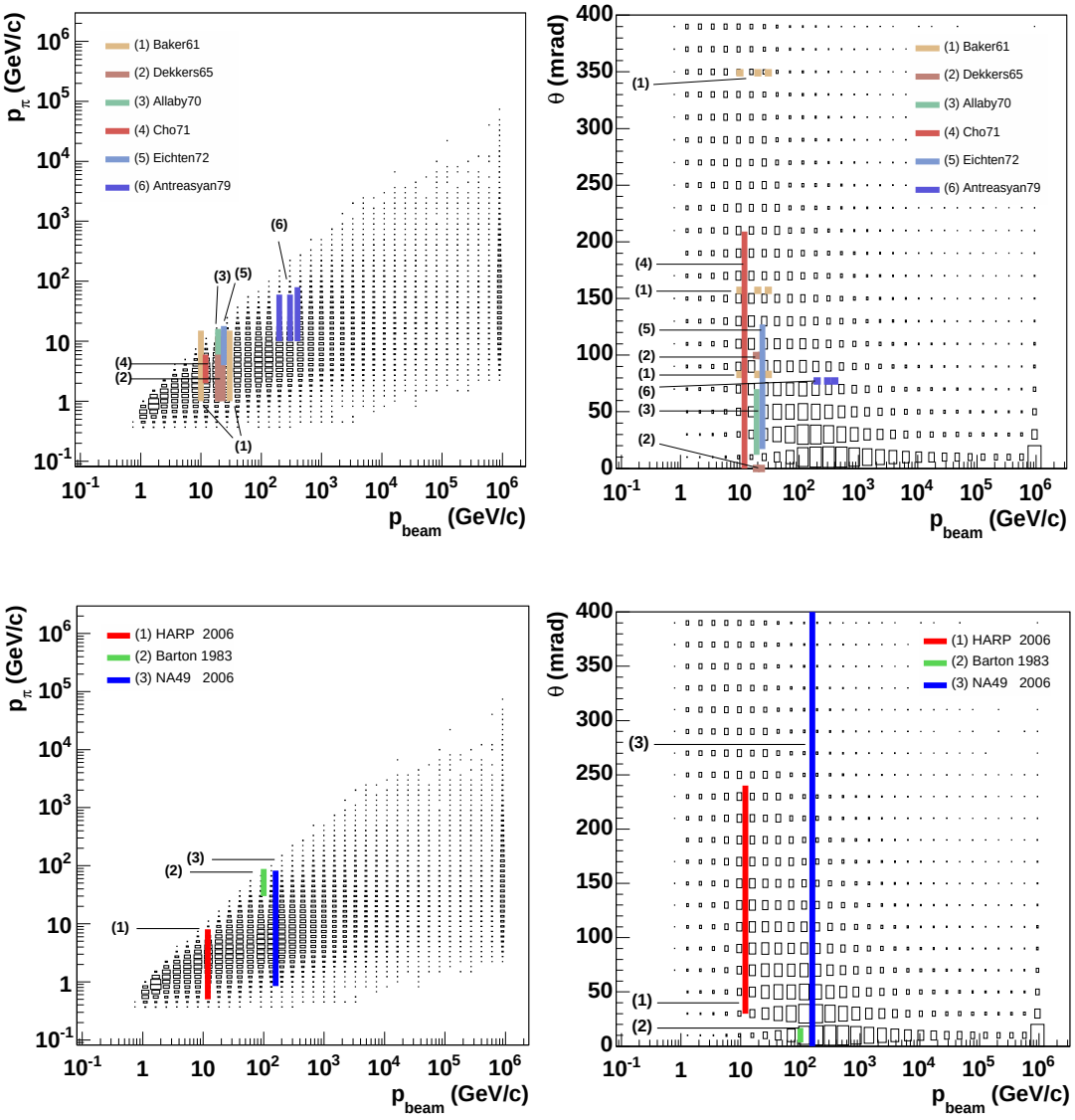

Figure 3.10: Coverage of the phase space regions of relevance to EAS (box histograms) by existing fixed target data using a proton beam and a beryllium (top panels [41]) or a carbon (bottom panels [43]) target (shaded/colored regions). Left panels: total momentum of secondary pions vs. total momentum of proton projectiles. Right panels: angle between beam and secondary particle momentum vs. beam momentum.

The compiled data were taken by single arm spectrometer experiments at CERN [44, 45, 46], Fermilab [47], at the Brookhaven Alternating Gradient Synchrotron (AGS) [48] and at the Zero Gradient Synchrotron (ZGS) [49] at the Argonne National Laboratory, near Chicago, some decades ago. These experiments measure secondary particles with a string of magnets and threshold Cherenkov counters tuned to transmit particles of a given momentum at a time. This method leads to a very good particle separation but a big disadvantage is that only one angle and one momentum of secondary particles can be measured at a time. Therefore, data taken by these experiments are often restricted to a few fixed angles and have a limited statistics.

The work of Eichten et al. [46] has become a widely used standard reference data set. This experiment used a proton beam with a beam momentum of 24 GeV and a beryllium target. The secondary particles (pions, kaons, protons) are measured in a broad angular range (17 mrad $< \theta <$ 127 mrad) and in a momentum region from 4 GeV/c up to 18 GeV/c. Other measurements cover only a smaller part of the phase space of interest to EAS [48, 44, 45, 49, 47]. A measurement for preparing the CERN neutrino beam experiments was performed by SPY/NA56 (NA52) [50, 51]. Therefore, a 450 GeV proton beam and a thick, pencil-shaped beryllium target was used. Because of the very limited angular range ($\theta \approx 0°$) it is not included in Fig. 3.10 (top).

3.3.2 Existing p+C data

As simulations with hadronic interaction models show, the particle production in p+air collisions is more similar to p+C collisions than to p+Be reactions because of the smaller difference in the atomic mass. Fig. 3.10 (bottom) shows the p+C data which were available up to the time of writing this thesis.

In the past the only measurement of p+C collisions, which was not limited to a fixed angle, was the experiment done by Barton et al. [52]. These data were collected using the Fermilab Single Arm Spectrometer facility in the M6E beam line. A proton beam with a momentum of 100 GeV/c and a thin carbon target (1.37 g/cm^2) was used. However, the phase space of the secondary particles (pions, kaons, protons) covers only a very small part of the phase space of interest to EAS.

New p+C data at 12 GeV/c and 158 GeV/c, taken by the CERN experiments HARP [53] at the PS accelerator and NA49 [54] at the SPS accelerator, are available since 2006. Both experiments consist of large acceptance detectors and therefore a large fraction of the secondary phase space is measured.

The HARP experiment is designed to measure hadron production using proton and pion beams with momenta between 1.5 and 15 GeV/c and various targets (liquid as well as solid) from light to heavier elements. It consists of two main parts, a forward and a large angle spectrometer and hence covers nearly the complete phase space. At 12 GeV/c the HARP p+C data cover secondary momenta of π^+ and π^- from 0.5 GeV/c to 8 GeV/c and an angular range from 30 mrad to 240 mrad. A detailed description of the HARP detector is given in chapter 4 and more information about the analysis of p+C, π^++C and π^-+C data at 12 GeV/c can be found in chapter 5.

The NA49 experiment is a large acceptance hadron spectrometer which consists of four time projection chambers (TPCs). The two vertex TPCs are located in a strong magnetic field. They allow the measurement of charge and momentum of the detected particles. The two main TPCs are outside the magnetic field. They are used for particle identification via dE/dx measurement. NA49 is optimized to measure the extremely high multiplicity of secondary particles in e.g. a lead-lead interaction at 158 GeV per nucleon, whereby about 1500 charged secondary particles are produced. Also a lot of combinations of beam types (p, C, Si, S, Pb) and targets (p, C, Si, S, Pb) are used at different beam energies (20 to 200 GeV per nucleon [55]). The secondary particles (π^+, π^-) produced in p+C collisions at 158 GeV are measured in a broad momentum range (0.85 GeV/c $\lesssim p \lesssim$ 82.6 GeV/c) and from very small angles up to 440 mrad [56].

3.3.3 Proposed experiments

An upgrade of the existing NA49 setup is planned [55] as a future project NA61. In summer 2006 a 7 day test run with a 200 GeV proton beam was performed to check the system. In autumn 2007 the first data will be taken using a 30 GeV proton beam on a carbon target. The number of events is expected to be about $3 \cdot 10^6$. The foreseen measurements of importance for astroparticle physics are reactions on p+C at the energies of 30, 40, 50 and 400 GeV and π+C reactions at 158 and 400 GeV.

The study of the properties of hadronic interactions in EAS presented in this work (section 3.1 and 3.2) have formed the basis of the cosmic ray relevant part of the proposal for NA61. Other physics motivation for the planned experiment stems from neutrino physics and heavy ion physics. Neutrino beam experiments need a precise knowledge of secondary pion cross-section in p+A reactions, because the neutrino beam is provided by the decay of pions produced in p+A reactions. The goal of the heavy ion program of NA61 is the study of the properties of strong interacting matter in equilibrium and the investigation of the phases of this matter.

The first step to upgrade the previous experiment NA49 is the modernisation of the computer equipment and readout electronics as well as the replacements of the beam defining counter in the trigger system and of the beam position detectors. Apart from this, in a second upgrade step it is planned to increase the event rate of the data acquisition by a factor 20 by replacing the TPC readout by an ALICE-like system [57, 58]. Additional upgrades are planned to enlarge the TPC acceptance and to measure the number of non-interacting nucleons from a projectile nucleus in A+A collisions event by event.

An upgrade of the MIPP experiment [59, 60] at Fermilab is recently proposed. MIPP has similar measurement possibilities like NA61. The data acquisition of MIPP is faster but the separation of secondary kaons is not as good as the one of NA61. The MIPP experiment will provide reactions on p+C, π+C and K+C collisions at 20, 60 and 120 GeV/c.

4 The HARP experiment

4.1 Physics goals

The fixed target experiment HARP ("HAdRon Production", PS214) was constructed to measure the hadron production cross-sections of protons and charged pions on various nuclear targets [61]. Precise and comprehensive studies of the secondaries of these reactions at particle momenta of a few GeV/c are important for several areas of particle physics.

- In a neutrino factory the neutrinos are decay products of charged pions which are produced in a reaction of a high-intensity proton beam with a nuclear target. To use this high beam power efficiently and for creating an economic design of a neutrino factory precise knowledge of the number of produced pions is of great interest [62, 63, 64, 65].
- Reduction of the uncertainties in the knowledge of the atmospheric neutrino flux would improve the understanding of the neutrino oscillations ($\nu_\mu \rightarrow \nu_\tau$) [66]. The main uncertainty stems from the limited understanding of the interactions of hadrons with nitrogen and oxygen nuclei in the atmosphere. HARP measurements can contribute to a deeper understanding of these reactions [67, 68, 69, 70, 71, 72, 73].
- One of the main problems of conventional neutrino beams is the fact that their composition, flux and spectrum is not well known. This leads to a major limitation of experiments using those beams. The reason of these uncertainties are the limited knowledge of pion and kaon production yields. Three neutrino oscillation experiments are using HARP data. For MiniBooNE [74] and SciBooNE [75], p+Be data at 8.9 GeV/c were taken using a thick beryllium target. For K2K [76], a proton run at 12.9 GeV/c was performed and a thick aluminium target was used.
- The three requirements mentioned above benefit directly from a better theoretical understanding of hadronic interactions. Tuning and verifying hadronic interaction models need precise input data to enable more realistic results of Monte Carlo simulations [77, 78, 79].

4.2 Experimental setup

The HARP experiment [80] is located in the T9 beam-line of the East Area of the Proton Synchrotron (PS) at the European Organization for Nuclear Research CERN (French: Conseil Européen pour la Recherche Nucléaire) near Geneva, Switzerland. Protons with a momentum of $24\,\mathrm{GeV}/c$ are sent from the PS to the North branch of the East Area where they interact with a primary target (usually aluminium). A momentum and charge selected fraction of the produced particles is used as beam for the HARP experiment. At $12\,\mathrm{GeV}/c$ most of the positive particles are protons, the second largest fraction consists of π^+ and a small fraction are K^+, electrons and other particle types. The negative charge selected beam consists mainly of π^- and a few K^-. The momentum resolution of the secondary beam is about 1%[80].

Before the beam particles reach the HARP detector they pass the beam instrumentation. It is formed by a set of beam detectors and counters to provide the detection, tracking and identification of the incoming beam particle as well as to generate primary signals for the trigger logic. For the detailed layout, see Fig. 4.1.

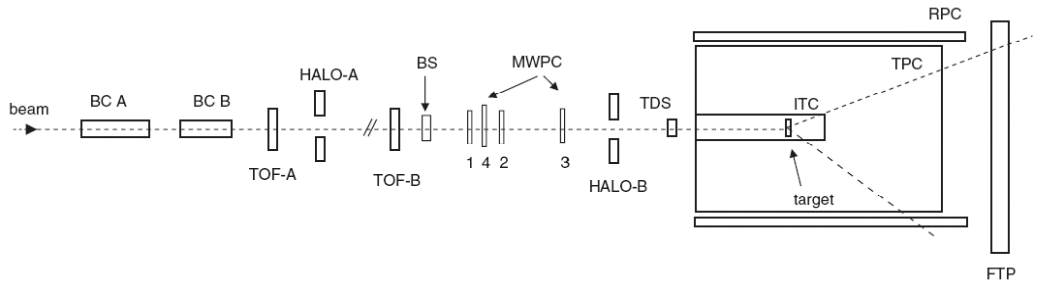

Figure 4.1: Schematic view of the beam instrumentation [80]. For the beam particle detection (tracking and particle identification), two time-of-flight detectors (TOF-A and TOF-B), two gas threshold Cherenkov counters (BC-A and BC-B) and a set of four multi-wire proportional chambers (MWPC1-4) are used. The trigger system consists of two scintillation halo counters (HALO-A and HALO-B) and two special scintillation counters (BS and TDS). Detailed descriptions are given in the text.

The following detectors are employed for the beam particle detection: A beam time-of-flight system consisting of two timing detectors (TOF-A, TOF-B) with an average time-of-flight resolution of 100 ps together with two gas threshold Cherenkov counters (beam counters: BCA, BCB) are used for beam particle identification. The beam counters also determine the interaction time at the target. The impact point and the direction of the beam particle are measured by a set of four multi-wire proportional

chambers (MWPCs) with an accuracy of <1 mm and <0.2 mrad per projection. The MWPCs are not only used for the tracking of the beam particle but also for the off-line reconstruction of the beam particle, the real time tuning and beam quality monitoring.

The trigger system upstream of the HARP detector selects a good beam particle. It consists of two scintillation halo counters (HALO-A, HALO-B) and two special scintillation counters called beam scintillator (BS) and target defining scintillator (TDS). The halo counters are made of two scintillator slabs with a central hole (diameter of the hole: HALO-A: 9 cm, HALO-B: 3 cm). HALO-A vetos all particles which did not pass through BCA and BCB. The final step to improve the purity of the beam is done by HALO-B as near to the target as possible. Thus the halo counters accept only single beam particles without any accompanying second particle in the halo of the beam. BS starts the decision logic of the trigger system and in coincidence with a TOF-B hit it represents the lowest-level trigger. Additionally the target is surrounded by two trigger detectors. The inner trigger cylinder (ITC) and the forward trigger plane (FTP) select events with interaction and provide a trigger for large-angle secondaries emerging from the target and for secondaries in the small angle region, respectively. A standard physics trigger condition for thin targets is BS $\times$ TOF-A $\times$ TOF-B $\times$ (NOT)HALO-A $\times$ (NOT)HALO-B $\times$ TDS $\times$ (ITC + FTP).

The HARP spectrometer consists of two main parts: a forward and a large-angle detection system. The target is housed inside the large-angle spectrometer which is composed of a time projection chamber (TPC) and a system of resistive plate chambers (RPC) both inside a solenoidal magnet. The TPC provides track, momentum and vertex measurements for charged secondary particles in an angular range from 20° up to 160° with respect to the beam direction. The particle identification is based on the measurement of the energy loss in the TPC as well as the time-of-flight measurement in the RPCs. The setup of the HARP detector is shown in Fig. 4.2.

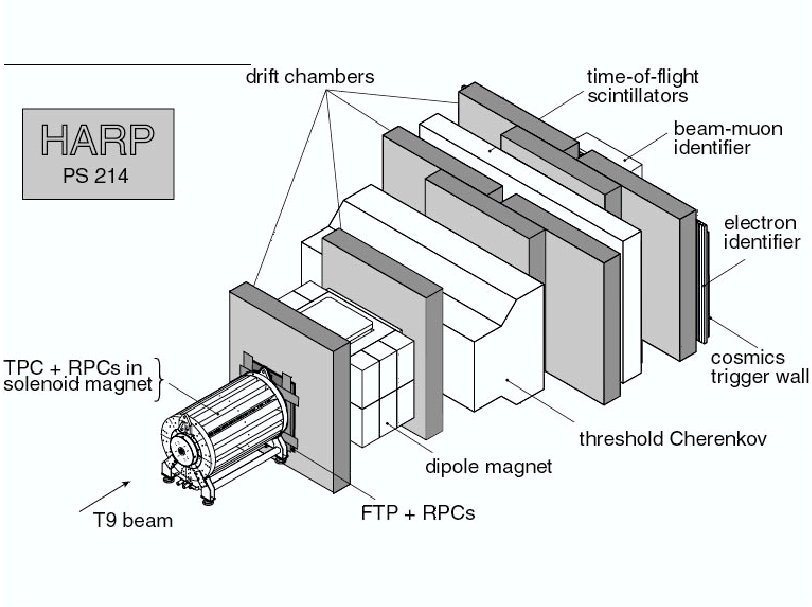

Figure 4.2: Schematic layout of the HARP spectrometer [81]. The different detector components are shown. The target is inserted inside the TPC.

Given the fact that this analysis is focused on the secondary particles in an angular range up to 13.75°, here the forward spectrometer is described in more detail than the large-angle detection system. For more details about the large-angle detection system see [80]. The forward spectrometer surrounds a dipole magnet with an integrated field of 0.66 Tm. It consists of three walls of large planar drift chambers for tracking and momentum analysis (The most downstream drift chambers are only partly equipped with electronics and not used for tracking.) and detectors for particle identification namely a threshold Cherenkov detector, a TOF-wall and an electromagnetic calorimeter. Additionally a beam muon identifier is placed behind the forward spectrometer in order to determine the number of muons in the pion beam.

4.3 Track and momentum reconstruction with the forward spectrometer

Five large drift chambers act as tracking device for forward going secondary particles. Originally they were built for the NOMAD experiment (WA96) [82]. Two chambers are placed directly upstream and downstream of the spectrometer magnet, three additional chambers are located further downstream in order to cover a large surface

between the Cherenkov detector and the TOF wall. Each drift chamber consists of four chamber components which are arranged in layers. This tracking system is shown in Fig. 4.3.

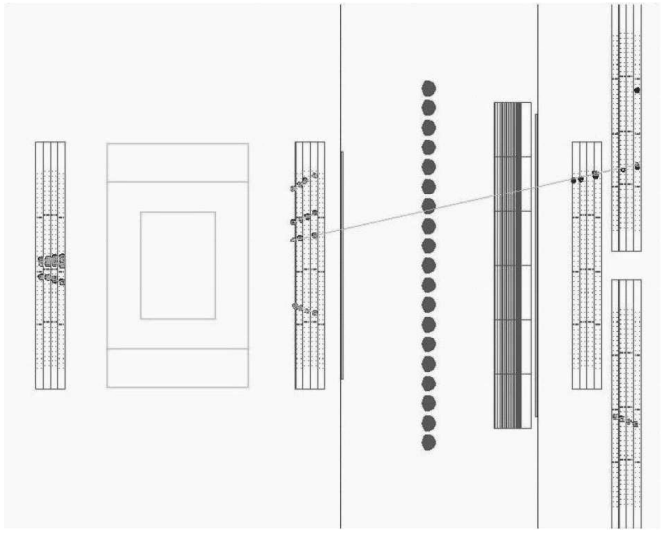

Figure 4.3: Event display [83] with the main detectors of the forward spectrometer from left to right: First drift chamber, dipole magnet, second drift chamber, threshold Cherenkov detector and a set of three drift chamber modules. The hits in the road which form the track segments for this event are visible in the chamber modules.

Track reconstruction proceeds as follows [81]. In a first step two-dimensional track segments are reconstructed in each chamber. At least seven hits are needed in one chamber to form such a track segment. These segments are combined to three-dimensional track fragments in a second iteration. Once this has been done, these fragments are merged with track segments in the other chambers into larger track fragments. Finally, downstream tracks, with respect to the spectrometer magnet, are extrapolated back to the target plane (This method is called VERTEX2.) or to a three-dimensional track segment (called VERTEX4) in the drift chamber upstream of the magnet. See Fig. 4.4. The downstream track efficiency is almost 100%, as it can be measured from the individual chamber efficencies.

There are two momentum reconstruction methods that are applied for this analysis [81]. The momentum estimator p_2 is extracted from downstream tracks extrapolated to the interaction vertex (VERTEX2). Only those tracks are accepted which have an extrapolated point at the target plane with a distance to the nominal centre of the target less than 20 cm. Another independent momentum estimator is defined as p_4. Hereby the momentum is measured connecting a downstream track segment with the segment

in NDC1 (VERTEX4).

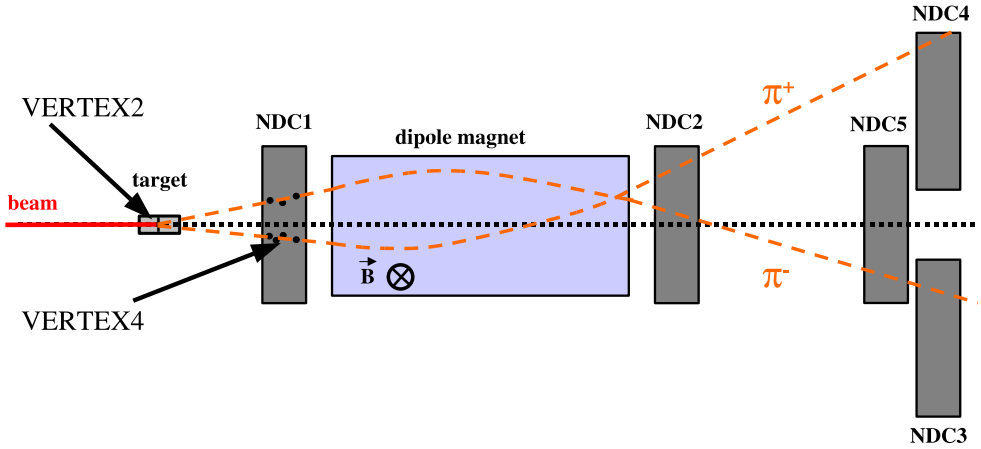

Figure 4.4: Two independent momentum reconstruction methods are applied [81]. For both methods downstream tracks are extrapolated to an upstream benchmark. In the case of VERTEX2 the target is used as upstream constraint, where VERTEX4 uses a track segment in the first drift chamber (NDC1).

The fact, that the two reconstruction methods provide independent momentum estimators and that $1/p_2$ and $1/p_4$ have a Gaussian distribution around the inverse true momentum $1/p$, allows a measurement of the tracking efficiency directly from data. (The curvature of a track is measured by its deflection Δx from a straight line which has a Gaussian distribution and is proportional to $1/p$.) One estimator is used for measuring the momentum and the other one for measuring the tracking efficiency. p_2 is preferred to determine the momentum since no track segment in the upstream chamber is necessary for its calculation and the track efficiency in this chamber is lower than in the downstream ones.

4.4 Particle identification

The particle identification for the forward spectrometer is based on the measurements of three different detector components [84]. The time-of-flight measurement, for which TOF-B in combination with the TOF wall system is used, allows pion–kaon and pion–proton separation to be performed up to 3 GeV/c and beyond 5 GeV/c, respectively. Fig. 4.5 gives an impression how well this method works for the proton–pion separation. The Cherenkov detector is used to separate pions from protons and kaons above 2.5 GeV/c and hadrons from electrons below 2.5 GeV/c. Additionally the separation of hadrons and electrons below 2.5 GeV/c is cross-checked by the signal in the

electron calorimeter in order to study the Cherenkov performance.

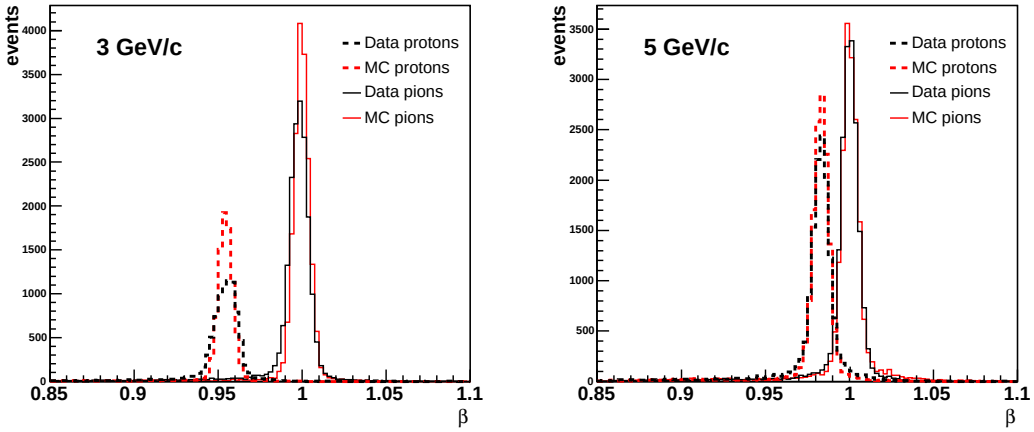

Figure 4.5: Time-of-flight (β) distributions for pions and protons with momenta 3 GeV$/c$ and 5 GeV$/c$, for both data and MC simulation [84]. The data set is a sample of beam particles, selected as pions or protons by the beam instrumentation, in the following chapters labeled as "empty target data". At 3 GeV$/c$ the two populations are completely separated, and the separation is still very good at 5 GeV$/c$.

4.5 Momentum calibration

The momentum calibration of the HARP forward spectrometer is done with three different methods [85]. The common idea behind these methods is to use data sets with tracks which have a known momentum. The primary method is the calibration of the momentum of the forward spectrometer with the beam particle penetrating through the detector without colliding with a target. This method is called "empty target" calibration. A second method is the use of known kinematical properties of the elastic scattering of a proton or pion on a proton in a hydrogen target. The third method is based on the precise time measurement of TOF wall. In the following the momentum resolution and scale corrections obtained with these three different methods are described. Fig. 4.6 shows the phase space covered by the different calibration methods.

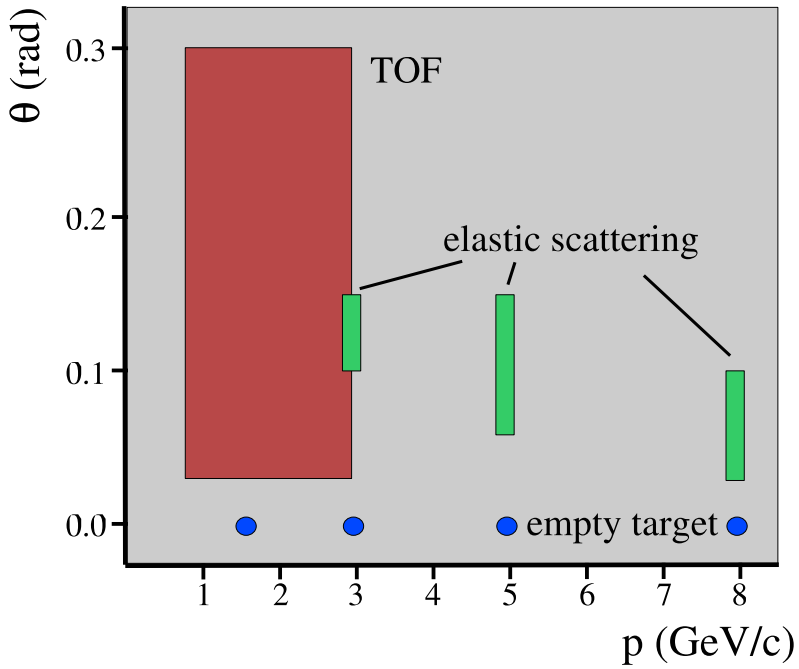

Figure 4.6: The phase space which is covered by the three calibration methods is indicated by boxes and circles in the θ-p plane.

4.5.1 Momentum calibration using empty target data sets

Initially it was foreseen to use the "empty target" method as main calibration method of the forward spectrometer. Empty target runs were taken for six energies starting from 1.5 GeV/c up to 15 GeV/c. But this method has several shortcomings. Only at fixed energies empty target measurements are available. The lowest momentum point is relatively high and the most serious problem is the fact that the direction of the beam is fixed and therefore the calibration is only done for a very small central part of the spectrometer. To cover larger angles the calibration is also performed with the use of elastic scattering events which is described in detail below.

4.5.2 Momentum calibration using elastic scattering events

The idea of this calibration method is the fact that if one of the kinematic observables of one particle (e.g. the momentum or scattering angle of the scattered or the recoil par-

ticle) is known, the other kinematic observables are determined by energy-momentum conservation. In this case the elastic scattering of two protons or a pion and a proton is regarded, assuming that the scattering angle is measured very precisely. As target a liquid hydrogen (H_2) target is used.

Energy conservation provides

$$E_{\text{target}} + E_{\text{beam}} = E_{\text{scat}} + E_{\text{recoil}} \quad . \tag{4.5.1}$$

With the relativistic energy–momentum relation $E^2 = p^2 + m^2$ (convention: speed of light $c = 1$) and the fact that the initial momentum of the target proton $p_{\text{target}} = 0$ follows

$$m_{\text{p}} + \sqrt{{m_{\text{b}}}^2 + {p_{\text{b}}}^2} = \sqrt{{m_{\text{b}}}^2 + {p_{\text{s}}}^2} + \sqrt{{m_{\text{p}}}^2 + {p_{\text{r}}}^2} \quad , \tag{4.5.2}$$

where m_{p} is the proton mass, m_{b} the mass of the beam particle (in this case a proton or a pion) and p_{b}, p_{s} and p_{r} are the momenta of the beam, elastically scattered and recoil particles.

Momentum conservation for the longitudinal momentum gives

$$\begin{aligned} p_{\text{b}\parallel} + p_{\text{t}\parallel} &= p_{\text{r}\parallel} + p_{\text{s}\parallel} && \text{with } p_{\text{b}\parallel} = p_{\text{b}} \text{ and } p_{\text{t}\parallel} = 0 \\ p_{\text{b}} &= p_{\text{r}} \cdot \cos\theta_{\text{r}} + p_{\text{s}} \cdot \cos\theta_{\text{s}} \end{aligned} \tag{4.5.3}$$

and for the transverse momentum follows

$$\begin{aligned} p_{\text{b}\perp} + p_{\text{t}\perp} &= p_{\text{r}\perp} + p_{\text{s}\perp} && \text{with } p_{\text{b}\perp} = 0 \text{ and } p_{\text{t}\perp} = 0 \\ 0 &= p_{\text{r}} \cdot \sin\theta_{\text{r}} + p_{\text{s}} \cdot \sin\theta_{\text{s}} \\ \theta_{\text{r}} &= \arcsin\Big(-\frac{p_{\text{s}} \cdot \sin\theta_{\text{s}}}{p_{\text{r}}}\Big) \quad . \end{aligned} \tag{4.5.4}$$

Inserting Eq. (4.5.4) in Eq. (4.5.3) yields

$$p_{\text{r}} \cdot \cos\Big[\arcsin\Big(-\frac{p_{\text{s}} \cdot \sin\theta_{\text{s}}}{p_{\text{r}}}\Big)\Big] = p_{\text{b}} - p_{\text{s}} \cdot \cos\theta_{\text{s}} \quad . \tag{4.5.5}$$

This equation is solved for p_{r}. After inserting p_{r} in Eq. (4.5.2) the relation between the momentum and the angle of the scattered particle is

$$\begin{aligned} p_{\text{theo}}(\theta) = \; & p_{\text{beam}}\Big[2\Big(m_{\text{beam}}^2 + m_{\text{p}}\sqrt{m_{\text{beam}}^2 + p_{\text{beam}}^2}\Big)\cos(\theta) \\ & + \sqrt{2}\Big\{\Big(m_{\text{beam}}^2 + m_{\text{p}}^2 + p_{\text{beam}}^2 + 2m_{\text{p}}\sqrt{m_{\text{beam}}^2 + p_{\text{beam}}^2}\Big) \\ & \Big(-m_{\text{beam}}^2 + 2m_{\text{p}}^2 + m_{\text{beam}}^2\cos(2\theta)\Big)\Big\}^{\frac{1}{2}}\Big] \\ & \Big/\Big[2\Big(m_{\text{beam}}^2 + m_{\text{p}}^2 + p_{\text{beam}}^2 + 2m_{\text{p}}\sqrt{m_{\text{beam}}^2 + p_{\text{beam}}^2} \\ & - p_{\text{beam}}^2\cos^2(\theta)\Big)\Big] \quad , \end{aligned} \tag{4.5.6}$$

where all momenta and angles are taken in the lab system. The dependence of the expected momentum of the scattered particle on the scattering angle is also shown in Fig. 4.7. The solid (red) curve describes elastic scattering for a proton beam, the dashed (blue) curve for a pion beam. The momenta of the scattered particles are very similar at small angles. For angles larger than 0.3 rad the mass difference between proton and pion becomes important.

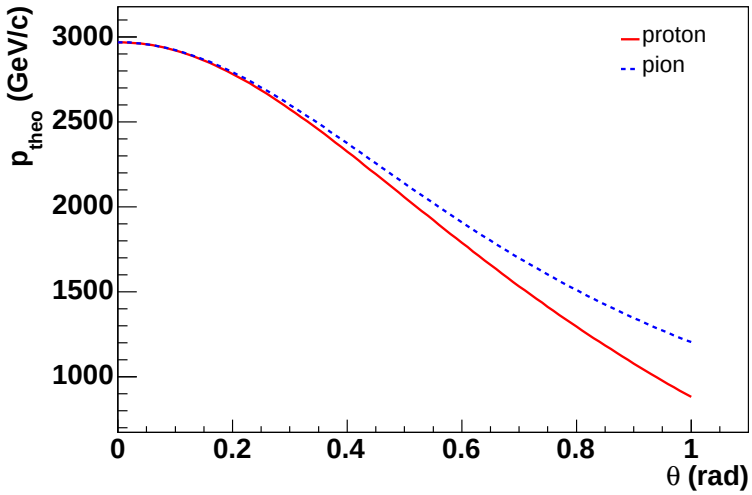

Figure 4.7: Momentum of a relativistic particle scattered on a proton in a hydrogen target as function of scattering angle (solid line: proton beam, dashed line: pion beam).

Elastic events can be readily selected from the data by imposing combined criteria in the large angle and forward spectrometer. The main selection criterion is the request of exactly one proton track in the TPC (recoil particle) and precisely one track in the forward spectrometer (scattered particle: proton or pion, depending on the beam particle type). Further constraints are applied and summarized in Table 4.1. It should be pointed out that no constraints on the momentum measurement of the forward track are set.

The accuracy of the determination of beam momentum and scattering angle is very good relative to the resolution of the secondary momentum. The beam momentum is known with an accuracy of 1% [80] and the angular resolution is about 1 mrad [81]. A reconstruction uncertainty of 1 mrad corresponds to a p_{theo} uncertainty of 0.12%. For $p < 8$ GeV the momentum resolution is only about 5% [85]. Using the predicted value of the momentum of the scattered particle, p_{theo}, at a fixed scattering angle and the corresponding measured momentum p_{scat}, spectra of the following observable are generated for different angular bins.

Table 4.1: Summary of the criteria for selection of elastic events from the data used for the momentum calibration.

Event selection	Beam angle < 0.005 rad Impact radius of beam < 8.0 mm FW trigger One and only one MWPC track reconstructed
Track selection	Reconstructed VERTEX2 Reconstruction quality of main vertex < 200.0 mm θ < 0.25 rad Particle reaches TOF wall 3 hits in road in NDC1 $\lvert\theta_y\rvert$ <0.1 rad

$$\Delta_{1/p_{\mathrm{scat}}} = \left(\frac{1}{p_{\mathrm{scat}}} - \frac{1}{p_{\mathrm{theo}}}\right) \cdot p_{\mathrm{theo}} \tag{4.5.7}$$

An example of these spectra is shown in Fig. 4.8 for proton–proton collisions using a proton beam with a momentum of 5 GeV/c and a 60 mm hydrogen target. Additionally similar spectra are analyzed for lower and higher beam momenta (3 and 8 GeV/c) and for a thicker target (180 mm at 3 and 8 GeV/c).

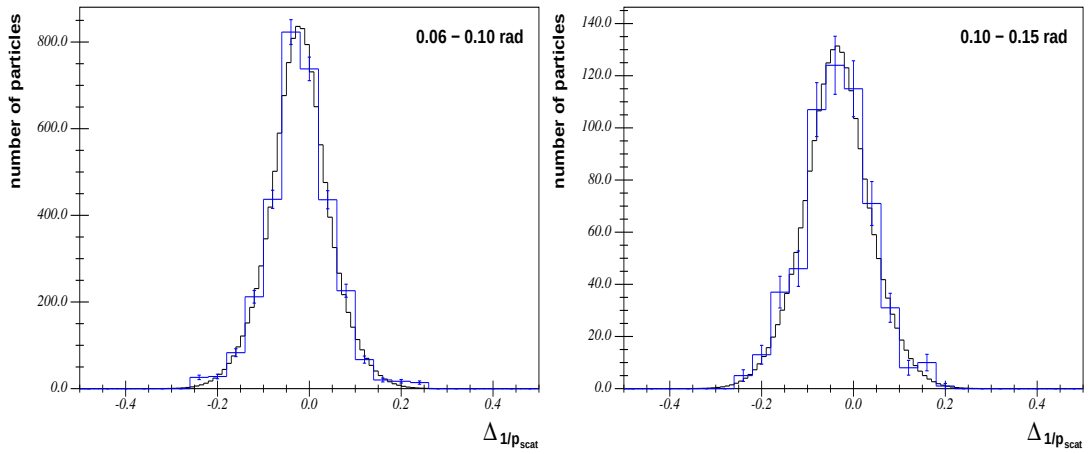

Figure 4.8: Example spectra of the variable $\Delta_{1/p_{\mathrm{scat}}}$ (Eq. 4.5.7) for a 5 GeV/c hydrogen data set (target: 60 mm). The spectra are generated for the angular bins: 0.06 -0.10 rad (left panel) and 0.10 -0.15 rad (right panel). Fit function: double Gaussian (Eq. 4.5.8).

These spectra are fitted with a double Gaussian function with the mean value μ of both single Gaussian functions being the same.

$$\begin{aligned} f_{\text{dgaussian}} &= f_0 + f_1 \\ f_0 &= \frac{A_0}{\sqrt{2\pi}\sigma_0}\exp\Big(-\frac{1}{2}\big(\frac{x-\mu}{\sigma_0}\big)^2\Big) \\ f_1 &= \frac{A_1}{\sqrt{2\pi}\sigma_1}\exp\Big(-\frac{1}{2}\big(\frac{x-\mu}{\sigma_1}\big)^2\Big) \end{aligned} \tag{4.5.8}$$

As result of the double Gaussian fit of the spectra at the three different momenta the momentum scale (equivalent to the mean of the fit function) and the momentum resolution (RMS, equivalent to the width of the spectra) are plotted as function of the momentum shown in Fig. 4.9. The RMS is defined as the weighted mean of the two single σ's.

$$\text{RMS} = \frac{A_0 \cdot \sigma_0 + A_1 \cdot \sigma_1}{A_0 + A_1} \tag{4.5.9}$$

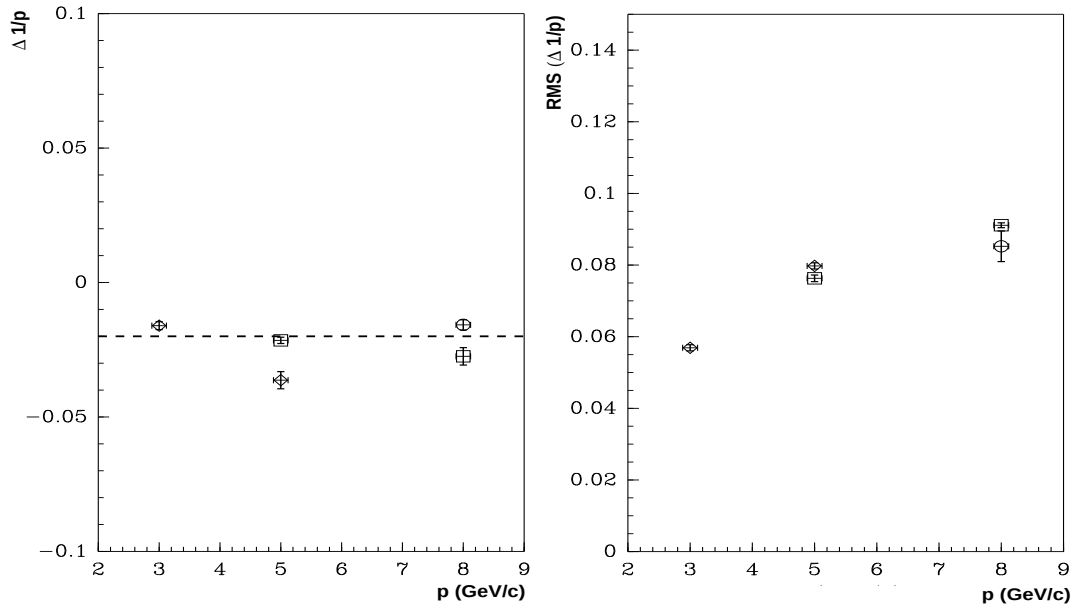

Figure 4.9: Momentum scale (left panel) and resolution (right panel) as function of beam momentum in three angular regions (circles: 30-60 mrad; squares:60-100 mrad; diamonds: 100- 150 mrad) [85].

The momentum scale decreases with larger angles but stays nearly constant for the momentum. The momentum resolution shows a decreasing trend for larger angles but increases with the momentum.

The momentum resolution and scale measured with the elastic scattering method extends the calibration toward larger angles than probed with the empty target method alone. Therefore, a larger range of the spectrometer is characterized by this method.

4.5.3 Momentum calibration using time-of-flight measurements

Time-of-flight measurements are used for a momentum calibration in the momentum range $0.7\,\mathrm{GeV}/c < p < 3.0\,\mathrm{GeV}/c$. In this momentum range, where the forward spectrometer has a good acceptance, pions are relativistic. Therefore the time-of-flight of pions depends only weakly on their momentum whereas the time-of-flight of protons shows a significant variation with momentum. This different dependence of the velocity β on momentum for pions and protons is caused by the mass difference of these particles. The TOF wall β resolution in the chosen momentum range is typically $\sigma(\beta)/\beta = 0.005$. The velocity β is calculated as ratio of the measured track length and the measured time-of-flight. The width of the β peak for a sample of protons selected in a small range in momentum shows a large sensitivity to the momentum resolution. To determine the momentum resolution in this way the time-response of the TOF wall has to be measured for pions and protons separately.

For this analysis two data sets are used, namely p+Al data set at $12.9\,\mathrm{GeV}/c$ and p+Be data set at $8.9\,\mathrm{GeV}/c$. From these data a very clean sample of secondary π^- is selected by using the different particle identification methods which are described in chapter 4.4. In a similar way a clean sample of secondary protons is selected. The negative pions also provide a perfect prediction for the behaviour of the TOF measurement of the positive pions. The data are divided into four angular bins (30-60 mrad, 60-100 mrad, 100-150 mrad, 150-200 mrad) and in small momentum bins. The size of the momentum bins is chosen to be of the order of the expected momentum resolution. In each of these bins a β spectrum is fitted by a double Gaussian function. The fit function takes into account the width of the momentum bins and the calibrated β resolution and uses the momentum resolution and momentum scale as free parameters. (The amplitude is also a free parameter but not important for this analysis.) The RMS of the fit result leads directly to the momentum resolution and the position of the β peak corresponds to the momentum scale. More detailed information about this calibration method can be found in [85].

Using the time-of-flight measurements the calibration range is extended to the region of low momenta. Combining information from the three calibration methods the full range of relevant angles and momenta is covered and the results indicate a good agreement in the overlapping phase space [85].

5 Analysis of pion production in p+C and $\pi^{\pm}$+C collisions

5.1 Data selection

The data sets which are used for the following analysis of the cross-section for positive and negative pion production in p+C and $\pi^{\pm}$+C reactions at 12 GeV/c were taken during two short run periods (each only two days) in June and September 2002. Over one million events with positive beam and more than half a million events with negative beam were collected. For detailed event statistics see Tab. 5.1.

The cylindric carbon target has a purity of 99.99%, a thickness of 18.94 mm, a diameter of 30.26 mm and its mass is 25.656 g. Derived from this the density of the target is 1.88 g/cm^3. (For comparison the density of graphite is 2.27 g/cm^3.) The thickness of the carbon target is equivalent to 5% nuclear interaction length (3.56 g/cm^2).

5.1.1 Event selection

First, for the analysis the favoured beam particle type is selected by using the beam time of flight system (TOF-A, TOF-B) and the Cherenkov counters (BCA, BCB) as described in chapter 4.2. The distribution of the position of beam particles extrapolated to the target is shown in Fig. 5.1. The position of the positive charge selected beam is shifted by about 5 mm in y-direction with respect to the nominal position ($x = 0; y = 0$) and covers a circular area of about 8 mm diameter. In the case of negatively charged beam particles the beam hits the target more centrally but it has a broader distribution of about 14 mm width in y-direction. To keep the selection efficiency high and not to take into account reactions at the target edge only particles within a radius of 12 mm are accepted for this analysis. Additionally the MWPC track is required to have a measured direction within 5 mrad of the nominal beam direction to further reduce halo particles. Applying these criteria the remaining number of events for data sets with

positive and negative beam are summarized in Tab. 5.1.

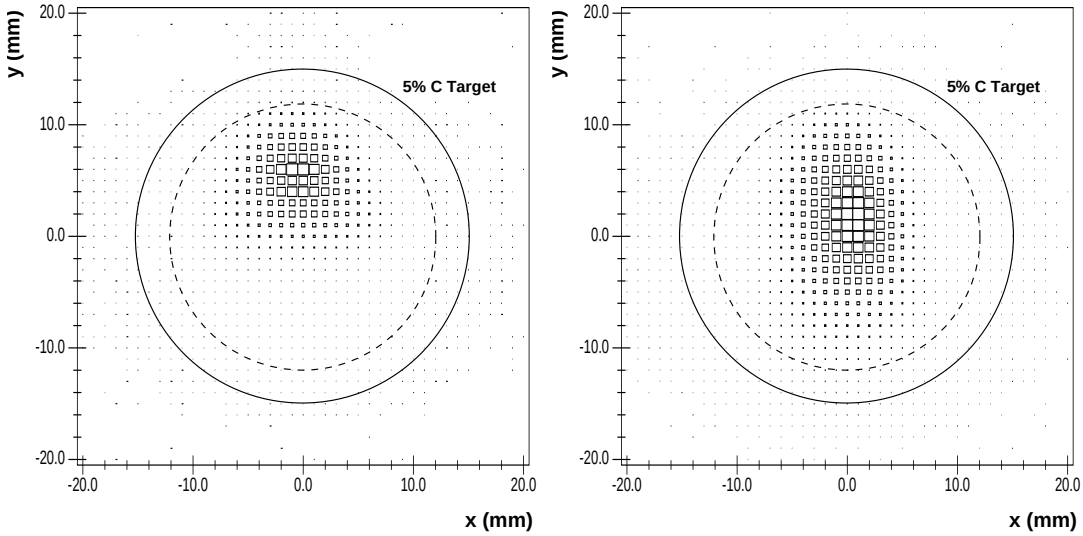

Figure 5.1: Reconstructed position of positively (left panel) and negatively (right panel) charged beam particles at the target plane. The solid circle gives the position and size of the carbon target (diameter: 30.26mm), the dashed circle indicates the region where beam particles are accepted (radius: 12mm).

Table 5.1: Total number of events in $12\,\mathrm{GeV}/c$ carbon target and empty target data sets (For explanation see chapter 5.2.) and in corresponding Monte Carlo simulations (See chapter 5.4).

	Carbon data	Empty target data	Monte Carlo
positive beam	1.062 k	886 k	23.4 M
accepted for p+C	467 k	287 k	20.3 M
accepted for π^++C	40 k	25 k	20.8 M
negative beam	646 k	531 k	23.4 M
accepted for π^-+C	350 k	214 k	20.8 M

5.1.2 Track selection

Secondary track selection criteria are optimized to ensure the quality of momentum reconstruction and a clean time-of-flight measurement while maintaining a high reconstruction efficiency. There are two kinds of acceptance criteria concerning the track reconstruction quality and the geometric characteristics of the tracks relative to the forward spectrometer. These criteria are described in the following and a summary of

track statistics for the three chosen data sets (p+C, π^++C, π^-+C) are given in Tab. 5.2. In the end about 5% to 6% of tracks in accepted events are used for the further analysis.

Reconstruction quality criteria

- Successful momentum reconstruction of secondary particle (momentum estimator p_2, see chapter 4.3).
- More than 3 hits in NDC2 and at least 5 hits in road in one of the chambers NDC3, 4, or 5 or at least 3 hits in one of the chambers NDC3, 4, 5 and more than 5 hits in road in NDC2.
- More than three hits in a road in NDC1 and average $\chi^2 \leq 30$ for these hits with respect to the track in NDC1 in order to reduce non-target interaction backgrounds. The distribution of number of hits in road in NDC1 is shown in Fig. 5.2.
- The track has a matched TOF wall hit.

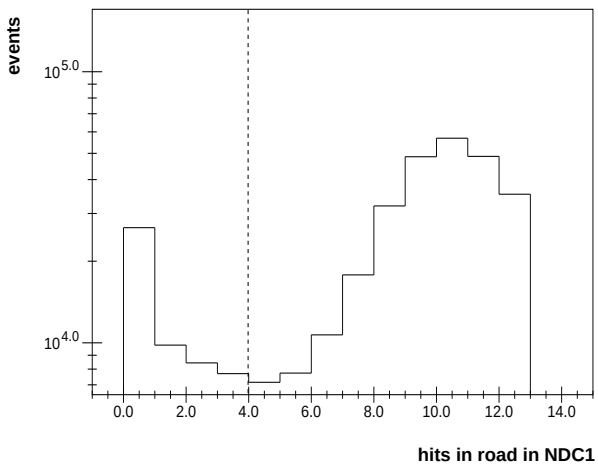

Figure 5.2: Number of hits in a road in the drift chamber NDC1. Only tracks with more than three hits in a road in NDC1 are accepted which is indicated by the dashed line. The unconsidered tracks are downstream tracks from secondary reactions which have a random association to NDC1 tracks.

Criteria on track geometry

- The angle θ of a secondary particle with respect to the beam axis is required to be less than 300 mrad. The distribution of θ is shown in Fig. 5.3 (left panel).

- The y-component θ_y of the angle θ is required to be between -100 and 100 mrad. See Fig. 5.3 (right panel).

- The extrapolation of a secondary track should point to the primary interaction point on the target plane within a radius of 200 mm.

- Only tracks which bend towards the beam direction are accepted as shown in Fig. 5.4. This is the case if the product of charge and θ_x is negative. This criteria is applied to avoid the positive θ_x region for positive charged secondary particles and the negative θ_x region for negative charged particles where the efficiency is momentum dependent.

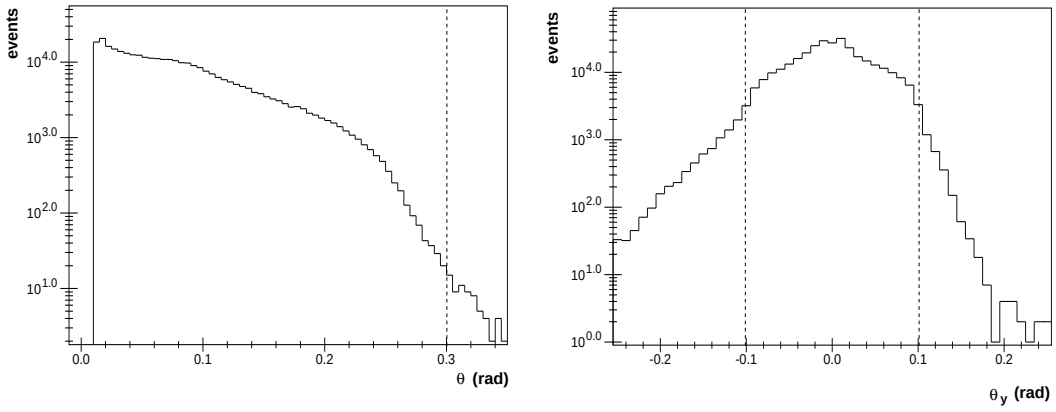

Figure 5.3: Distribution of θ (left panel) and θ_y (right panel). The acceptance criteria for this observables are indicated by dashed lines.

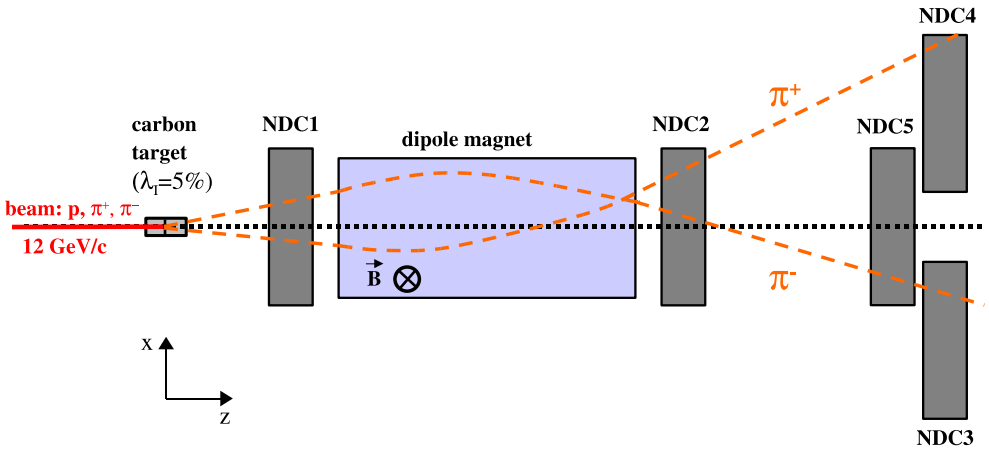

Figure 5.4: Only tracks which bend towards the beam direction are accepted. This means the product of charge and θ_x must be negative.

Table 5.2: Number of tracks in accepted events before and after the selection criteria for secondary tracks are applied. About 5% to 6% of all tracks are used for the analysis in this work.

	Total number of tracks	Number of selected tracks
p+C	2,057,420	100,035
π^++C	192,976	10,122
π^-+C	1,701,041	106,534

5.2 Empty target subtraction

Interactions of beam gas particles or interactions of beam particles outside the target, e.g. in one of the drift chambers, produce background to the interactions of beam particles on the target. This background is measured experimentally by taking data without a target. These measurements are called “empty target data”. The “empty target data” are also subject to the event and track selection criteria like the standard carbon data sets. The event statistics of these data sets can be taken from Tab. 5.1.

To take into account this background the number of particles of an observed particle type (π^+, π^-) in the “empty target data” are subtracted bin-by-bin (momentum and angular bins) from the number of particles of the same type in the carbon data. The uncertainty following from this method is discussed in chapter 5.5 and labeled “empty target subtraction”.

5.3 Calculation of cross-section

The goal of this analysis is to investigate the double differential, inclusive cross-section of negative and positive pions in p+C, π^++C and π^-+C reactions at 12 GeV/c in a broad range of secondary momentum and angle. It is calculated as follows

$$\frac{d^2\sigma^\alpha}{dpd\Omega}(p_i,\theta_j) = \frac{A}{N_A\rho t}\cdot\frac{1}{N_{\text{pot}}}\cdot\frac{1}{\Delta p_i\Delta\Omega_j}\cdot\sum_{p_i',\theta_j',\alpha'}\mathscr{M}^{\text{cor}}_{p_i\theta_j\alpha p_i'\theta_j'\alpha'}\cdot N^{\alpha'}(p_i',\theta_j')\,, \quad (5.3.1)$$

where

- $\frac{d^2\sigma^\alpha}{dpd\Omega}(p_i,\theta_j)$ is the cross-section in mb/(GeV/c sr) for the particle type α (p, π^+ or π^-) for each momentum and angle bin (p_i,θ_j) covered in this analysis,
- $N^{\alpha'}(p_i',\theta_j')$ is the number of particles of type α in bins of reconstructed momentum p_i' and angle θ_j' in the raw data,
- $\mathscr{M}^{\text{cor}}_{p\theta\alpha p'\theta'\alpha'}$ is a correction matrix which accounts for efficiency and resolution of the detector,
- $\frac{A}{N_A\rho t}$, $\frac{1}{N_{\text{pot}}}$ and $\frac{1}{\Delta p_i\Delta\Omega_j}$ are normalization factors, namely

  $\frac{N_A\rho t}{A}$ is the number of target nuclei per unit area [1],

  N_{pot} is the number of incident beam particles on target (particles on target),

  Δp_i and $\Delta\Omega_j$ are the bin sizes in momentum and solid angle, respectively [2].

5.4 Calculation of correction matrix

While the number of particles $N^{\alpha'}(p_i',\theta_j')$ is relatively easy to count in the raw data, the calculation of the correction matrix $\mathscr{M}^{\text{cor}}_{p_i\theta_j\alpha p_i'\theta_j'\alpha'}$ is much more complex. Various techniques are described in the literature to obtain this matrix. As mentioned in [81] and [85] for a p+Al analysis of HARP data at 12.9 GeV/c as well as for p+Be at 8.9 GeV/c, two complementary analyses have been performed to check internal consistency and possible biases in the respective procedures. The comparison of both analyses shows that the results are consistent within the overall systematic error [81].

[1] A = atomic mass, N_A = Avogadro number, ρ = target density and t = target thickness

[2] $\Delta p_i = p_i^{\max} - p_i^{\min}$, $\Delta\Omega_j = 2\pi(\cos(\theta_j^{\min}) - \cos(\theta_j^{\max}))$

In the first method the correction matrix $\mathscr{M}^{\mathrm{cor}}_{p_i\theta_j\alpha p'_i\theta'_j\alpha'}$ is decomposed into distinct independent contributions, which are computed mostly using the data themselves. The second method is the unfolding method introduced by D'Agostini [86]. It is based on the Bayesian unfolding technique [83]. A simultaneous (three dimensional) unfolding of momentum p, angle θ and particle type α is performed. The correction matrix is computed using a Monte Carlo simulation. This method is applied in the carbon analysis described here.

Caused by various error sources and limited acceptance and efficiency of an experiment, no measured observable represents the true physical value. The unfolding method tries to solve the problem to find the distribution of the corresponding true value to a measured observable. A main assumption is that the probability distribution function in the "true" physical parameters can be approximated by a histogram with discrete bins. Than the relation between the vector $\vec{x}$ of the true physical parameter and the vector $\vec{y}$ of the measured observable can be described by a matrix $\mathscr{M}_{\mathrm{mig}}$ which represents the mapping from the true value to the measured one. This matrix is named migration (smearing) matrix

$$\vec{y} = \mathscr{M}_{\mathrm{mig}} \cdot \vec{x} \quad . \tag{5.4.1}$$

The goal of the unfolding procedure is to determine a transformation for the measurement to obtain the expected values for $\vec{x}$ using the relation (5.4.1) [87]. The most simple and obvious solution is matrix inversion. But this method often provides unstable results. Large correlations between bins lead to large off-diagonal elements in the migration matrix $\mathscr{M}_{\mathrm{mig}}$ and the result is dominated by very large variances and strong negative correlation between neighbouring bins.

Within the method of D'Agostini, the unfolding is performed by the calculation of the unfolding matrix $\mathscr{M}^{\mathrm{UFO}} = \mathscr{M}^{\mathrm{cor}}$ in an iterative way which is used instead of $\mathscr{M}^{-1}_{\mathrm{mig}}$. $\mathscr{M}^{\mathrm{UFO}}$ is a two-dimensional matrix connecting the measurement space (effects) with the space of the true values (causes). Expected causes and measured effects are represented by one-dimensional vectors with entries $x_{\mathrm{exp}}(C_i)$ and $y(E_j)$ for each causes and effect bin C_i and E_j, respectively. It is

$$x_{\mathrm{exp}}(C_i) = \sum_j \mathscr{M}^{\mathrm{UFO}}_{ij} \; y(E_j) \quad . \tag{5.4.2}$$

The Bayes' theorem provides the conditional probability $P(C_i|E_j)$ for effect E_j to be caused by cause C_i

$$P(C_i|E_j) \propto P(E_j|C_i) \cdot P(C_i) \quad , \tag{5.4.3}$$

where $P(E_j|C_i)$ is the probability for cause C_i to produce effect E_j which corresponds to the migration matrix and could be calculated from Monte Carlo. $P(C_i)$ is the probability for cause C_i to happen. Eq. (5.4.3) is solved in an iteration process. The initial probability $P_0(C_i)$ could be assumed to be a uniform distribution. The so found

$P(C_i|E_j)$ is used as unfolding matrix in a first interaction step and leads to a first estimation of the expected values for causes

$$x_{\text{exp}}(C_i) = \sum_j P(C_i|E_j)\ y(E_j) \quad . \tag{5.4.4}$$

From $x_{\text{exp}}(C_i)$ a new probability $P_1(C_i)$ for cause C_i is calculated and insert in Eq. (5.4.3) for the next iteration step. Before this, the distribution of $P_1(C_i)$ can optionally be smoothed to reduce oscillations due to statistical fluctuations. Between two consecutive iteration steps a χ^2-test is applied. The iteration process is stopped when χ^2 is small. The number of iterations is dependent on the specific case. Too many iteration steps lead to the same kind of oscillating results as plain matrix inversion; for too few iteration steps, the results are strongly biased by the measurement.The final result of this method is the unfolded distribution of $x_{\text{exp}}(C_i)$ and its covariance matrix.

For this analysis, the original unfolding program provided by D'Agostini is used. $P_0(C_i)$ is assumed to be a uniform distribution, while $P(E_j|C_i)$ is calculated from the Monte Carlo simulation. In [83] it is shown that smoothing the distribution of $P_n(C_i)$ before inserting in the next iteration step does not lead to better (smoother) results than without. Therefore the smoothing process is not applied in this analysis. After four iteration steps the iteration process is stopped. The entries of the one-dimensional vectors $\vec{x}$ and $\vec{y}$ as well as the entries of the two-dimensional matrix $\mathscr{M}^{\text{UFO}}$ carry the information of angle, momentum and particle type. These original three dimensions are merged into one dimension as follows

$$n_{\theta,p,\alpha} = n_\theta + n_p \cdot n_\theta^{\max} + n_\alpha \cdot n_\theta^{\max} \cdot n_p^{\max} \quad , \tag{5.4.5}$$

where $n_{\theta,p,\alpha}$ is the bin number in the final vectors and in the unfolding matrix. n_θ, n_p and n_α are the bin numbers in the three dimensions θ, p and α, respectively. $n_\theta^{\max}$ and $n_p^{\max}$ are the total number of bins in the observables p and α.

The used Monte Carlo simulation is based on the Geant4 (GEometry ANd Tracking) [88] platform developed by CERN. The detector materials are accurately reproduced in this simulation as well as the relevant features of the detector response and the digitization process. All relevant physical processes are considered, including multiple scattering, energy-loss, absorption and re-interactions. The simulation is independent of the beam particle type because it only generates for each event exactly one secondary particle of a specific particle type inside the target material and propagates it through the target. Owing this the same simulation can be used for the three analyses of p+C, π^++C and π^-+C at 12 GeV/c.

The unfolding matrix for the p+C analysis calculated this way is shown in Fig. 5.5 in the left upper panel. The very good separation in the three particle types (π^-, π^+ and proton) can clearly be seen. The angular (right upper panel) and momentum (lower panels) unfolding matrices have a nearly diagonal structure as expected. The binning chosen for these matrices is the same as the one used for the particle spectra (see chapter 5.6). The unfolding matrices for the two other analyses (π^++C and π^-+C) are by construction very similar as the same Monte Carlo tracks are used, only the binning is different.

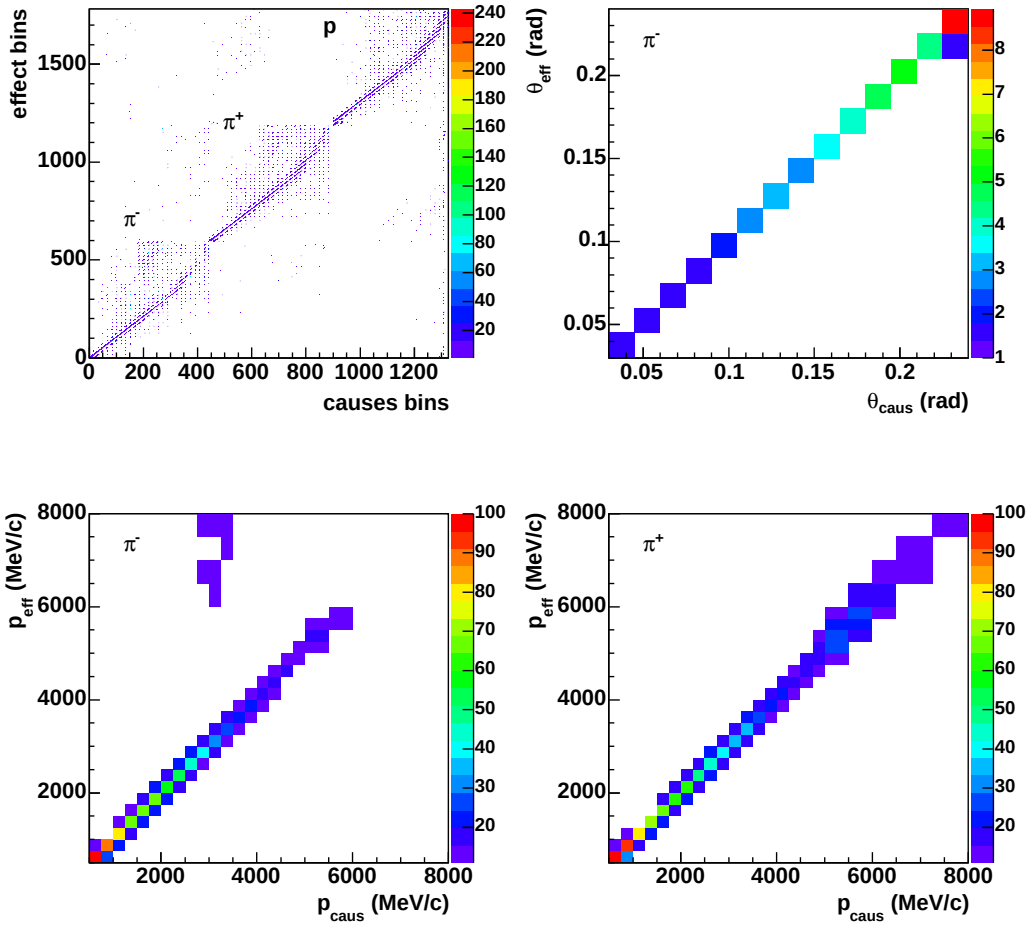

Figure 5.5: Unfolding matrices calculated for p+C analysis. The left upper panel shows the original unfolding matrix where the three dimensions angle, momentum and particle type are merged in one dimension as described by Eq. (5.4.5). The upper right panel shows an example of an angular unfolding matrix for π^- in one momentum causes-effects cell. The momentum unfolding matrices summed over θ for π^- (left) and π^+ (right) can be seen in the two lower panels.

5.5 Error estimation

5.5.1 Statistical errors

The total statistical error of the corrected data is composed of the statistical error of the raw data, but also of the statistical error of the unfolding procedure, because the unfolding matrix is obtained from the data themselves and hence contributes also to the statistical error. The statistical error provided by the unfolding program is equivalent to the propagated statistical error of the raw data. In order to calculate the statistical error of the unfolding procedure a separate analysis following [83] is applied, which is described below. The p+C data set is divided into two independent data samples *a* and *b*, one sample contains all events with odd and the other all events with even event numbers. These data samples are unfolded in three different ways.

1. Both samples are unfolded separately using the individually calculated unfolding matrix for each sample (set(1)).
2. Each of the two samples are unfolded with the unfolding matrix calculated by using the whole data set (set(2)).
3. The whole data set is unfolded two times, using the unfolding matrices generated for each part of the split data set (set(3)).

For all three sets the same Monte Carlo input is applied. The statistical error of the Monte Carlo simulation is negligible, because the Monte Carlo statistics is very high relative to the statistics of the raw data. Set(1) leads to the total statistical error of the unfolding result, set(2) to the the statistical error of the raw data and set(3) to the statistical error of the unfolding matrix. For all sets the difference between the unfolded result of data sample *a* and *b* is calculated and divided by the propagated statistical error of the raw data *a* and *b*,

$$\Delta_{ab} = \frac{a-b}{\sqrt{\sigma_a^2+\sigma_b^2}} \quad . \tag{5.5.1}$$

The distribution of Δ_{ab} shows for all three sets a Gaussian shape with a mean around zero. The width of the distribution of Δ_{ab} for set(1) is $k(\sigma_{\mathrm{stat}}) = 2.0$, for set(2) $k(\sigma_{\mathrm{stat}}^{\mathrm{data}}) = 0.98$ and for set(3) $k(\sigma_{\mathrm{stat}}^{\mathrm{UFO}}) = 1.77$. A consistency check gives

$$\begin{aligned} k(\sigma_{\mathrm{stat}}) &= \sqrt{k^2(\sigma_{\mathrm{stat}}^{\mathrm{data}}) + k^2(\sigma_{\mathrm{stat}}^{\mathrm{UFO}})} \\ 2.0 &\simeq \sqrt{0.98^2 + 1.77^2} \quad . \end{aligned} \tag{5.5.2}$$

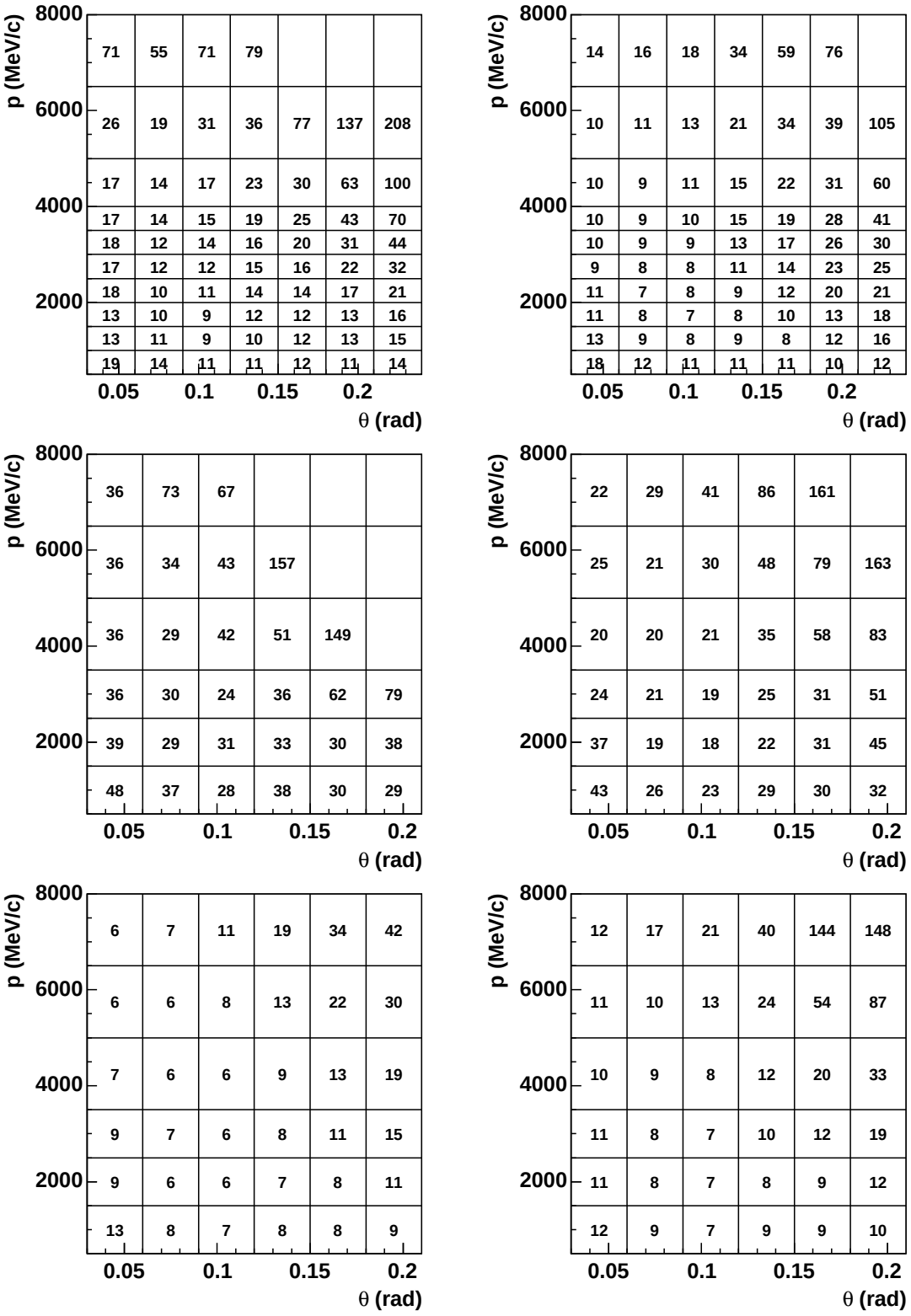

Figure 5.6: Statistical error in % for each momentum-angle bin. Left panels: secondary π^-, right panels: π^+. Top: p+C, middle: π^++C, bottom: π^-+C.

Concluding from this the statistical error provided by the unfolding procedure has to be multiplied globally by a factor 2, which is done for the three analyses (p+C, π^++C and π^-+C) described in this thesis.

Fig. 5.6 shows the calculated statistical errors in % for each momentum-angle bin for all three data sets and separately for secondary π^- and π^+. Due to the high statistics of the data set the binning for the p+C data set is chosen finer than for the other data sets. The limited statistics of the π^++C data is reflected in the relatively high statistical error. Generally, the statistical error increases slightly with larger angle and significantly with increasing momentum. The behaviour of statistical error as function of momentum can be seen in Fig. 5.7.

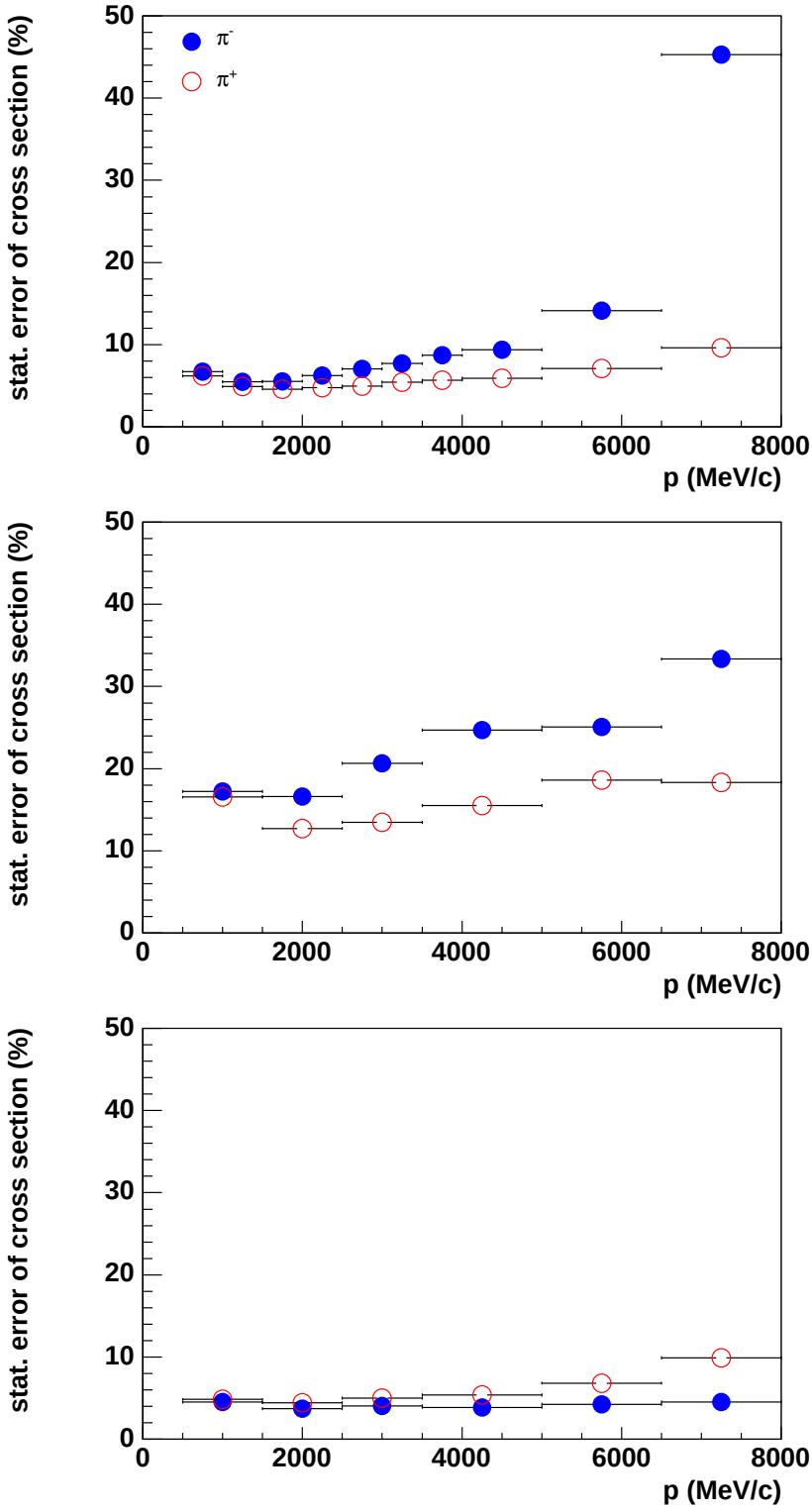

Figure 5.7: Statistical errors of π^- (filled circles) and π^+ (open circles) as function of momentum integrated over θ from 0.03 rad to 0.24 rad. Top: p+C, middle: π^++C, bottom: π^-+C.

5.5.2 Systematic errors

Different types of sources produce systematic errors for the analysis of the fixed target data described here. Namely they are track yield corrections, particle identification, momentum and angular reconstruction. Following mainly [89], the strategy to calculate these systematic errors is to find different solutions of the unfolding problem, i.e. different 'causes' result vectors. The difference vector is used to create a covariance matrix for a specific systematic error. Three different methods are applied to calculate these different causes vectors.

1. Variation of the normalization of causes vector.
2. Variation of the unfolding matrix.
3. Variation of the raw data.

The first method is used for the estimation of the systematic error of the track reconstruction efficiency. The uncertainties in the efficiency are estimated from the variation observed with the elastic scattering data and the difference of efficiency observed for the data and the simulations for protons.

The second method is applied for most of the systematic error estimations. The loss of secondary particles has to be considered due to particle decay and absorption in the detector materials as well as additional background particles generated in secondary reactions. These effects are simulated by Monte Carlo methods: Two single particle Monte Carlo simulations are generated, in one simulation these effects are taken into account and in another simulation not. Both Monte Carlo simulations are used for unfolding data and the results are compared. Uncertainties in the absorption of secondaries in the material of and close to the ITC of the TPC are taken into account by a variation of 10% of this effect in the simulation. The uncertainty in the production of background due to tertiary particles is larger. A 30% variation of the secondary production was applied [89].

The performance of particle identification, momentum and angular measurements are correlated due to the simultaneous unfolding process of these observables as described in chapter 5.4. The calculation of systematic errors of particle identification, angular and momentum resolution as well as of momentum scale is done by varying the acceptance criteria for these observables and their resolutions and scale in the raw data and in Monte Carlo simulated data. For the momentum resolution possible discrepancies up to 10% of the resolution are taken into account [89]. A potential bias in the mo-

mentum determination is estimated to be of the order of 2% using the elastic scattering analysis [89].

Electrons are not considered in the particle identification method. Instead, they are suppressed by a cut on the signal of the Cherenkov detector for particles with momenta below $2.5\,\mathrm{GeV}/c$, called "electron veto" [84]. This veto introduces a loss of efficiency for pions and protons. To calculate the systematic error of the electron veto method two samples of raw data are used. For both only the best matched track per event is selected. At the first sample no selection on the particle type is made, the second sample only consists of particles identified as electrons. The electron sample is subtracted from the hadron control sample. The subtracted sample (i.e. non-electrons) and the unselected sample (all particles including electrons) are unfolded independently. The difference of these unfolding results is associated with the systematic error of the electron veto method.

The third method is introduced for the estimation of the systematic error of the empty target subtraction. In addition to the standard empty target subtraction only 95% of the calculated empty target value is subtracted from the raw data. The systematic error is taken from the difference of these two results.

Due to the fact that kaons are not taken into account by the particle identification method, an additional error source are misidentified secondary kaons [84]. However, most of the kaons are rejected by the particle selection criteria of the TOF and the Cherencov detectors and kaons with low momenta decay. Therefore, the background effect caused by kaon misidentification is small. Nevertheless, to reduce this effect a specific Monte Carlo simulation only with secondary kaons is generated. The so found migration matrix is added to the pion migration matrix and this data sample is unfolded. This is equivalent to assuming that the kaon momentum and angular distributions are similar to the distributions of pions. The classification of these simulated kaons as particle types known by the particle identification method reflects the effect of misidentified kaons in the data.

Following [89] an overall normalization of the results is calculated relative to the number of incident beam particles accepted by the selection.

As result of these systematic error studies each error source is represented by a covariance matrix. The sum of these matrices describes the total systematic error. The diagonal elements of the covariance matrix of the total systematic error are shown for each momentum-angular bin in Fig. 5.8. In Fig. 5.9 the total systematic error can be seen as function of momentum and integrated over θ. For the π^++C and π^-+C data sets the systematic error has a nearly flat distribution and is of the order of 6%. For the p+C data set the systematic error increases for higher momenta but stays also nearly

constant around 8% at low momenta until 6 GeV/c.

To inspect in detail the specific systematic error sources the particular error δ_{diff} on the double-differential cross-section and the error δ_{int} on the cross-section integrated over the entire pion phase space are calculated.

First, the dimensionless quantity δ_{diff}, expressing the typical error on the double-differential cross-section, is defined as follows

$$\delta_{\text{diff}} = \frac{\sum_i (\delta[d^2\sigma^\pi/(dpd\Omega)])_i}{\sum_i (d^2\sigma^\pi/(dpd\Omega))_i} \quad , \tag{5.5.3}$$

where the index i labels a given momentum-angular bin (p,θ), $(d^2\sigma^\pi/(dpd\Omega))_i$ is the central value for the double-differential cross-section measurement in that bin, and $(\delta[d^2\sigma^\pi/(dpd\Omega)])_i$ is the error associated with this measurement.

Second, the dimensionless quantity δ_{int} is defined, expressing the fractional error on the integrated pion cross-section σ^π in the momentum range 0.5 GeV/$c < p <$ 8.0 GeV/c and the angular range 0.03 rad$< \theta <$0.24 rad for the p+C data and in the range 0.03 rad$< \theta <$0.21 rad for the $\pi^\pm$+C data, as follows

$$\delta_{\text{int}} = \frac{\sqrt{\sum_{i,j} (\Delta p \Delta\Omega)_i C_{ij} (\Delta p \Delta\Omega)_j}}{\sum_i (d^2\sigma^\pi/dpd\Omega)_i (\Delta p \Delta\Omega)_i} \quad , \tag{5.5.4}$$

where $(d^2\sigma^\pi/dpd\Omega)_i$ is the double-differential cross-section in bin i, $(\Delta p\Delta\Omega)_i$ is the corresponding phase space element, and C_{ij} is the covariance matrix of the double-differential cross-section. $\sqrt{C_{ii}}$ corresponds to the error $(\delta[d^2\sigma^\pi/(dpd\Omega)])_i$ in Eq. (5.5.3).

δ_{diff} as well as δ_{int} are summarized for all specific systematic error sources in Tab. 5.3 for p+C data, in Tab. 5.4(top) for π^++C data and in Tab. 5.4(bottom) for π^-+C data. The systematic errors are of the same order for all three data sets, δ_{diff} = 9-11% and δ_{int} = 5-8%. The most dominant error sources are particle absorption and the subtraction of tertiary particles. The errors of momentum and angular reconstruction are less important and the errors caused by the particle misidentification are negligible. For the data sets with positively charged beam the systematic error is smaller for π^+ and for the π^-+C data set it is smaller for π^-.

Systematic and statistical errors are of the same order for the p+C and the π^-+C data. For the π^++C data set the statistical error is dominating the total error. The π^-+C data have the smallest total error caused by the most convenient relation between data statistics and chosen bin width.

Table 5.3: Summary of the uncertainties affecting the double-differential and integrated cross-section measurements of p+C data.

Error category	Error source	$\delta^{\pi^-}_{\text{diff}}$(%)	$\delta^{\pi^-}_{\text{int}}$(%)	$\delta^{\pi^+}_{\text{diff}}$(%)	$\delta^{\pi^+}_{\text{int}}$(%)
Statistical	Data statistics	12.8	3.2	10.8	2.5
Track yield corrections	Reconstruction efficiency	1.6	1.3	1.1	0.5
	Pion, proton absorption	4.2	3.7	3.7	3.2
	Tertiary subtraction	9.8	4.2	8.6	3.7
	Empty target subtraction	1.2	1.2	1.2	1.2
	Subtotal	10.8	5.9	9.5	5.1
Particle identification	Electron veto	<0.1	<0.1	<0.1	<0.1
	Pion, proton ID correction	<0.1	0.1	0.1	0.1
	Kaon subtraction	<0.1	<0.1	<0.1	<0.1
	Subtotal	0.1	0.1	0.1	0.1
Momentum reconstruction	Momentum scale	2.6	0.4	2.8	0.3
	Momentum resolution	0.7	0.2	0.8	0.3
	Subtotal	2.7	0.5	2.9	0.4
Angle reconstruction	Angular scale	0.5	0.1	1.3	0.5
Systematic error	Subtotal	11.2	5.9	10.0	5.1
Overall normalization	Subtotal	2.0	2.0	2.0	2.0
All	Total	17.1	7.0	14.9	6.1

Table 5.4: Summary of the uncertainties affecting the double-differential and integrated cross-section measurements of π^++C data (top table) and π^-+C data (bottom table).

Error category	Error source	$\delta^{\pi^-}_{\text{diff}}$(%)	$\delta^{\pi^-}_{\text{int}}$(%)	$\delta^{\pi^+}_{\text{diff}}$(%)	$\delta^{\pi^+}_{\text{int}}$(%)
Statistical	Data statistics	41.8	6.4	34.5	7.2
Track yield corrections	Reconstruction efficiency	1.4	0.7	0.9	0.5
	Pion, proton absorption	4.0	2.1	3.3	2.7
	Tertiary subtraction	9.3	4.7	7.6	6.3
	Empty target subtraction	1.0	0.7	1.0	1.0
	Subtotal	10.3	5.2	8.4	6.9
Particle identification	Electron veto	<0.1	<0.1	<0.1	<0.1
	Pion, proton ID correction	0.1	<0.1	0.2	0.2
	Kaon subtraction	<0.1	<0.1	<0.1	<0.1
	Subtotal	0.1	0.1	0.2	0.2
Momentum reconstruction	Momentum scale	3.2	0.2	3.6	0.5
	Momentum resolution	0.9	0.2	1.1	0.3
	Subtotal	3.3	0.3	3.8	0.6
Angle reconstruction	Angular scale	1.7	0.1	1.3	0.5
Systematic error	Subtotal	10.9	5.3	9.2	7.0
Overall normalization	Subtotal	2.0	2.0	2.0	2.0
All	Total	43.7	8.5	35.8	10.2

Error category	Error source	$\delta^{\pi^-}_{\text{diff}}$(%)	$\delta^{\pi^-}_{\text{int}}$(%)	$\delta^{\pi^+}_{\text{diff}}$(%)	$\delta^{\pi^+}_{\text{int}}$(%)
Statistical	Data statistics	8.5	2.2	10.0	1.9
Track yield corrections	Reconstruction efficiency	1.3	1.1	0.7	0.4
	Pion, proton absorption	3.5	3.1	3.8	2.3
	Tertiary subtraction	7.9	6.8	9.0	5.3
	Empty target subtraction	0.9	0.8	0.9	0.6
	Subtotal	8.8	7.6	9.8	5.8
Particle identification	Electron veto	<0.1	<0.1	<0.1	<0.1
	Pion, proton ID correction	0.1	0.1	0.1	0.1
	Kaon subtraction	<0.1	<0.1	<0.1	<0.1
	Subtotal	0.1	0.1	0.1	0.1
Momentum reconstruction	Momentum scale	2.3	0.7	2.7	0.3
	Momentum resolution	0.6	0.2	0.5	0.2
	Subtotal	2.4	0.7	2.7	0.4
Angle reconstruction	Angular scale	0.6	0.3	0.7	<0.1
Systematic error	Subtotal	9.1	7.6	10.2	5.8
Overall normalization	Subtotal	2.0	2.0	2.0	2.0
All	Total	12.6	8.2	14.4	6.5

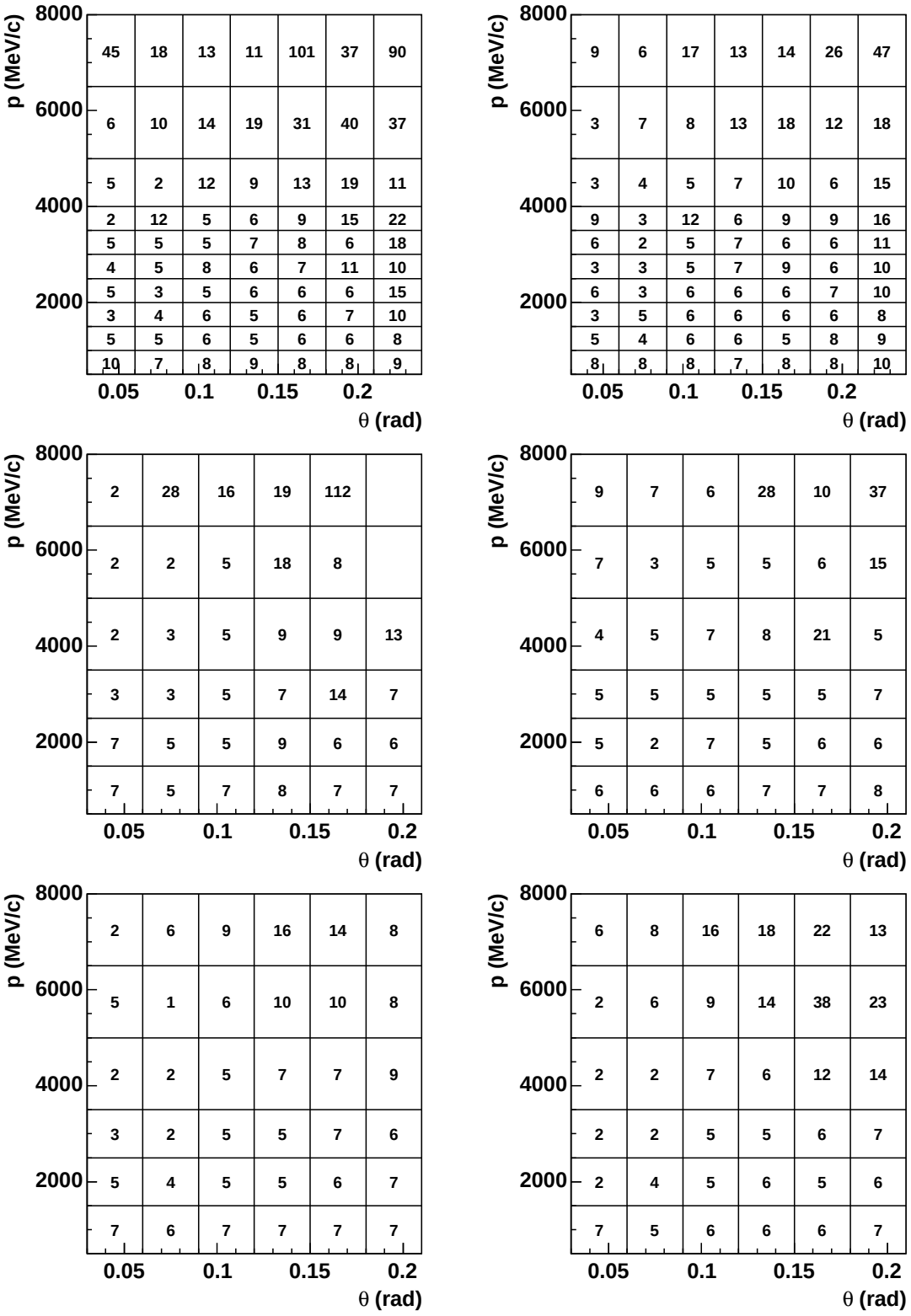

Figure 5.8: Total systematic error in % for each momentum-angular bin. Left panels: secondary π^-, right panels: π^+. Top: p+C, middle: π^++C, bottom: π^-+C.

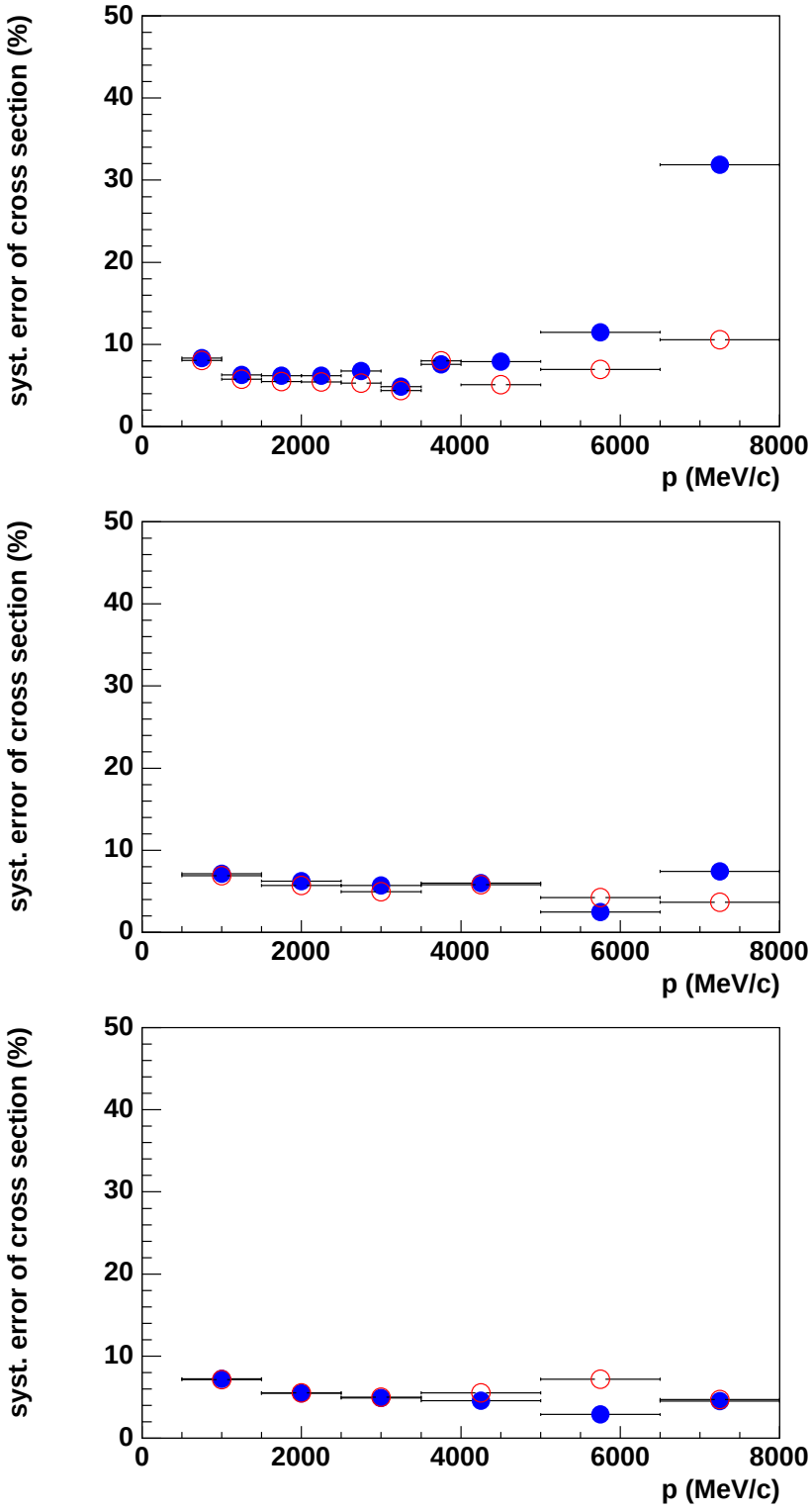

Figure 5.9: Total systematic error of π^- (filled circles) and π^+ (open circles) as function of momentum integrated over θ from 0.03 rad to 0.24 rad. Top: p+C, middle: π^++C, bottom: π^-+C.

5.6 Particle production spectra

The derived double-differential, inclusive cross-sections for positive and negative pion production in p+C [90], π^++C and π^-+C reactions at $12\,\mathrm{GeV}/c$ in the laboratory system are presented as function of momentum for various angular bins in Fig. 5.10, Fig. 5.11 and Fig. 5.12, respectively. The kinematic range of the measurements covers the momentum region from $0.5\,\mathrm{GeV}/c$ to $8.0\,\mathrm{GeV}/c$ and the polar angular range from 0.03 rad to 0.24 rad for p+C and from 0.03 rad to 0.21 rad for π^++C and π^-+C data. The error bars correspond to the combined statistical and systematic error as described in chapter 5.5.

The shapes of the momentum spectra are similar for secondary π^+ and π^- as well as for the different data sets. For small angles the spectra are harder than for larger angles and show a leading particle effect for produced π^+ in p+C and π^++C reactions and for π^- in π^-+C reactions. The distribution of secondary π^+ in π^++C reactions show a very similar behaviour as the distribution of secondary π^- in π^-+C reactions as expected caused by the isospin symmetry of $\pi^+ + \mathrm{C} \rightarrow \pi^+ + X$ and $\pi^- + \mathrm{C} \rightarrow \pi^- + X$. The corresponding behaviour can be seen for π^- in π^++C and π^+ in π^-+C collisions.

In the following section a Sanford-Wang parametrization of the momentum spectra is given and in chapter 6 a comparison with predictions of hadronic interaction models also used for air shower simulations with CORSIKA is presented. Additionally, a comparison with momentum spectra of secondary pions in p+N_2 and p+O_2 reactions at the same energy is discussed.

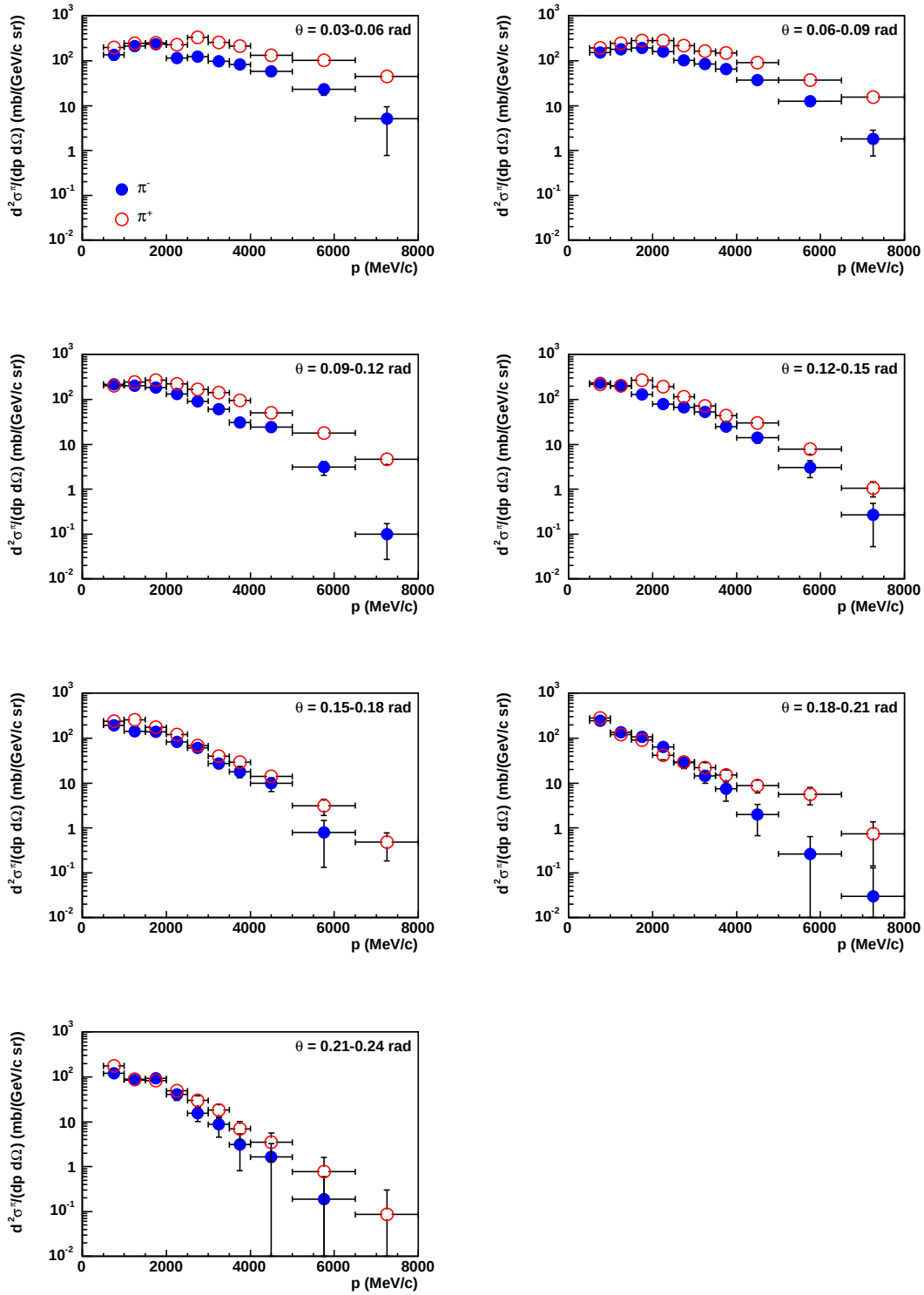

Figure 5.10: Momentum spectra of secondary π^- (filled circles) and π^+ (open circles) mesons in p+C reactions at 12 GeV/c measured with the HARP spectrometer at the PS accelerator at CERN. The seven different panels show the spectra in different angular bins from 0.03 rad to 0.24 rad.

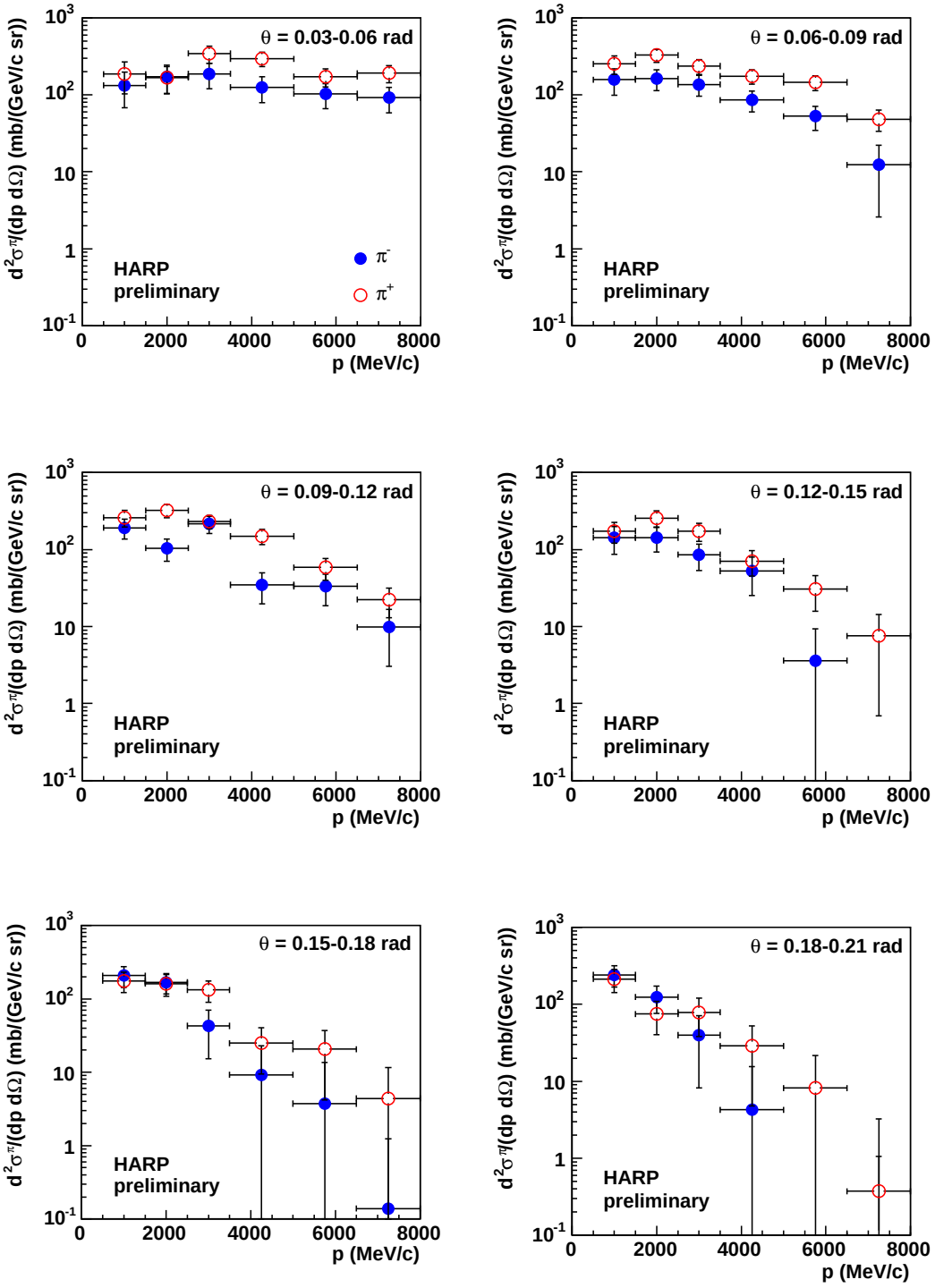

Figure 5.11: Preliminary momentum spectra of secondary π^- (filled circles) and π^+ (open circles) mesons in π^++C reactions at 12 GeV/c measured with the HARP spectrometer at the PS accelerator at CERN. The six different panels show the spectra in different angular bins from 0.03 rad to 0.21 rad.

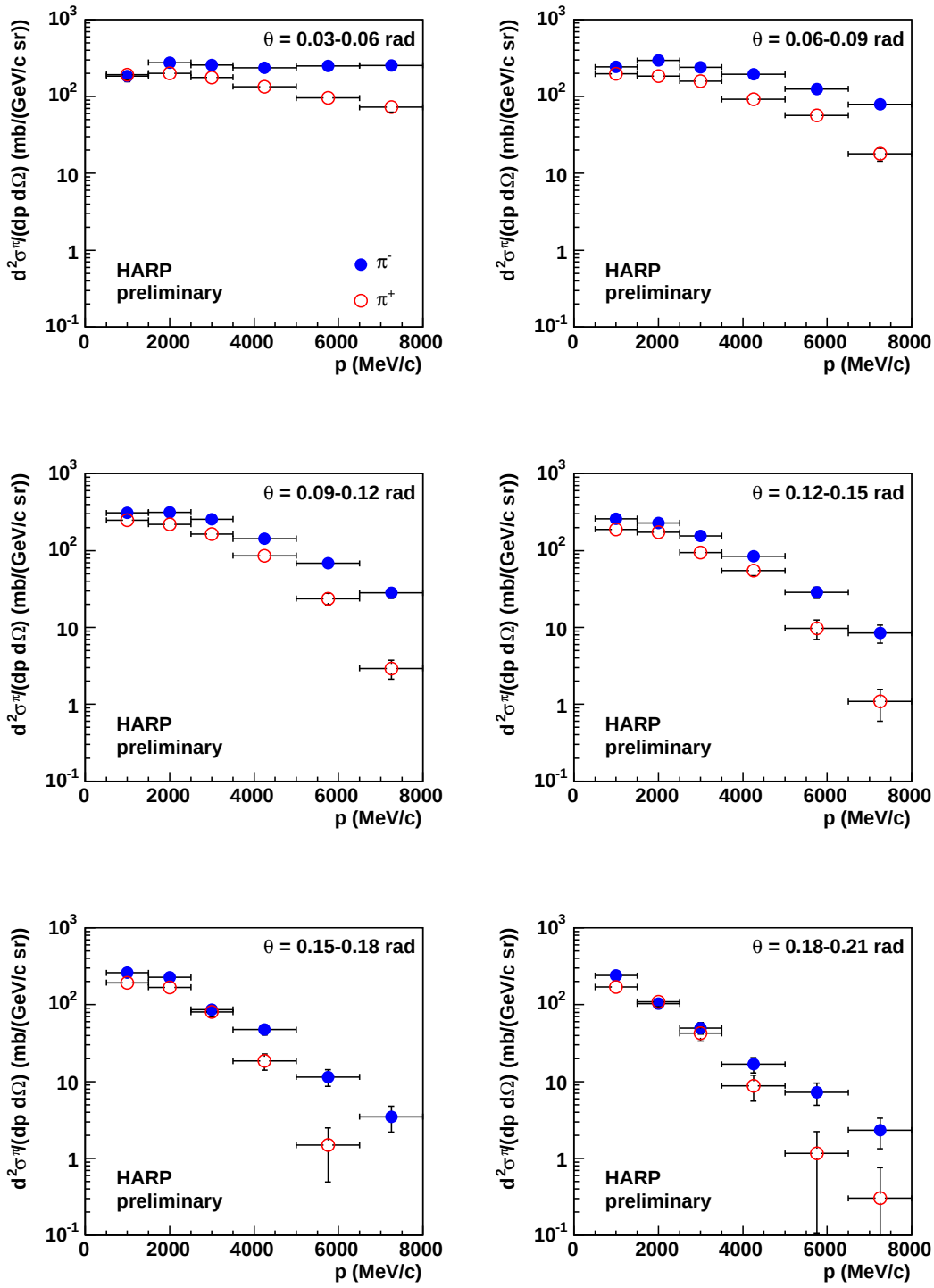

Figure 5.12: Preliminary momentum spectra of secondary π^- (filled circles) and π^+ (open circles) mesons in π^-+C reactions at 12 GeV/c measured with the HARP spectrometer at the PS accelerator at CERN. The six different panels show the spectra in different angular bins from 0.03 rad to 0.21 rad.

5.7 Sanford-Wang parametrization

Usually, for the modification and tuning of hadronic interaction models a parametrization of accelerator data is used. Therefore, a Sanford-Wang parametrization [91] of the momentum spectra of secondary pions produced in p+C, π^++C and π^-+C reactions measured with the HARP detector is given in the following. The Sanford-Wang parametrization is an empirical parametrization with eight free parameters, describing the production cross-sections of mesons in proton-nucleus interactions. Its functional form is:

$$\frac{d^2\sigma^\pi}{dpd\Omega}(p,\theta) = c_1 p^{c_2}\left(1-\frac{p}{p_{\text{beam}}}\right)\exp\left[-c_3\frac{p^{c_4}}{p_{\text{beam}}^{c_5}}-c_6\theta\left(p-c_7 p_{\text{beam}}\cos^{c_8}\theta\right)\right] \quad , \tag{5.7.1}$$

where

- $\frac{d^2\sigma^\pi}{dpd\Omega}(p,\theta)$ is the cross-section in mb/(GeV/c sr) for secondary pions as function of momentum p (in GeV/c) and angle θ (in radians) of the secondary particles,
- p_{beam} is the beam momentum in GeV/c,
- c_1, ..., c_8 are free parameters obtained from fits to meson production data.

The parameter c_1 is an overall normalization factor, the four parameters c_2, c_3, c_4, c_5 can be interpreted as describing the momentum distribution of the secondary pions, and the three parameters c_6, c_7, c_8 as describing the angular distribution for fixed secondary and beam momenta, p and p_{beam}.

This empirical formula has been fitted to the momentum spectra of π^+ and π^- production in p+C, π^++C and π^-+C reactions at 12 GeV/c reported in this thesis. As start values for these fits the parameters of the Sanford-Wang fit of the p+Al HARP analysis at 12.9 GeV/c are taken from [81]. In the χ^2 minimization procedure the full error matrix is used. Concerning the Sanford-Wang parameters estimation, the values of Sanford-Wang parameters are reported in Tab. A.7, Tab. A.8 and Tab. A.9 in the appendix (p. 108-109). The measured secondary momentum spectra of π^- and π^+ in p+C, π^++C and π^-+C reactions are compared to the Sanford-Wang parametrization in Fig. 5.13, Fig. 5.14 and Fig. 5.15, respectively. The Sanford-Wang parametrization is not able to describe some of the data spectral features especially at low and at high momenta. The goodness-of-fit of the Sanford-Wang parametrization hypothesis for the measured spectra can be assessed by considering χ^2 per degrees of freedom, see Tab. A.7-A.9 in the appendix. A discussion of the fit results is given in chapter 6.

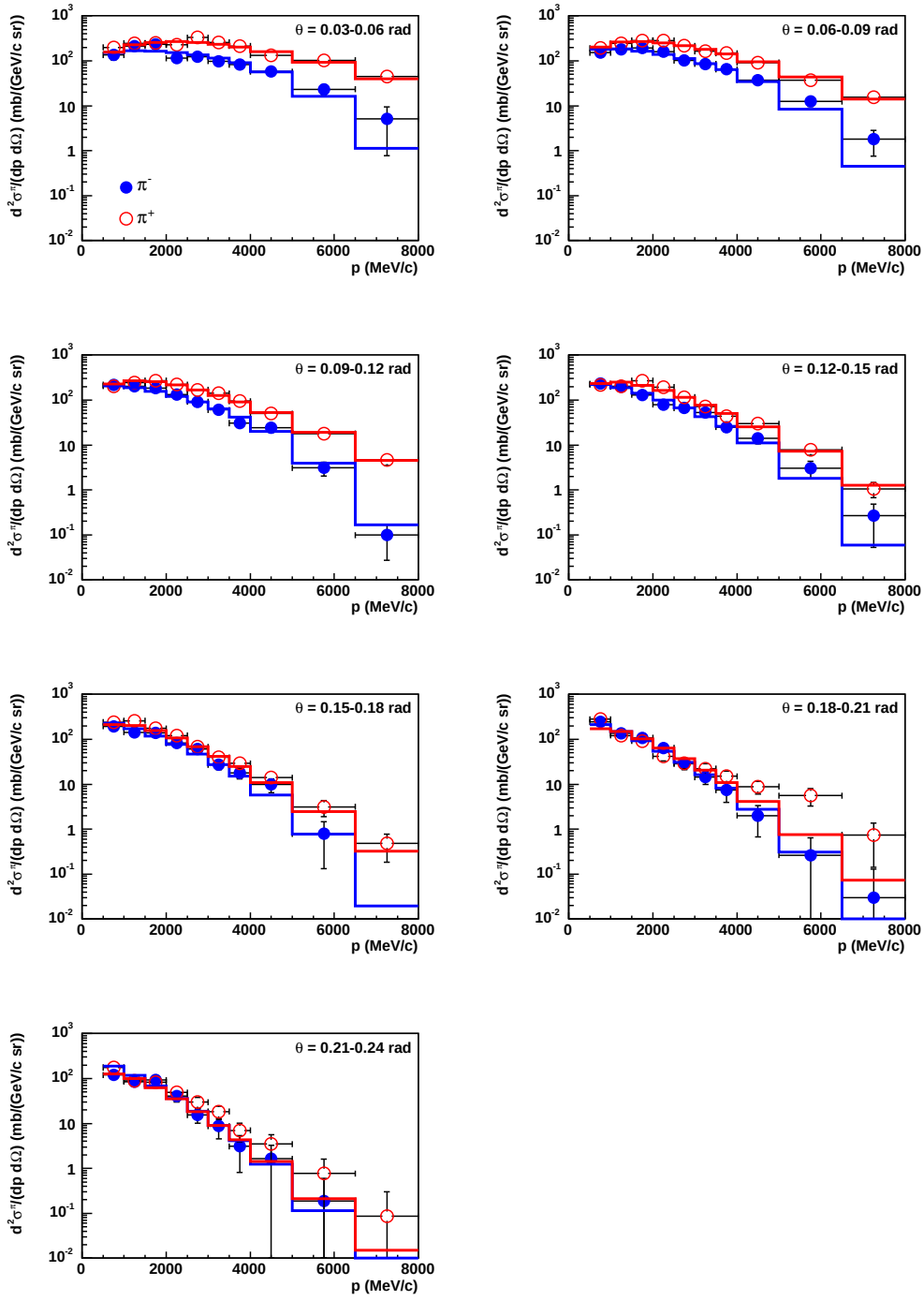

Figure 5.13: Sanford-Wang parametrization for pion momentum spectra in p+C reactions at 12 GeV/c.

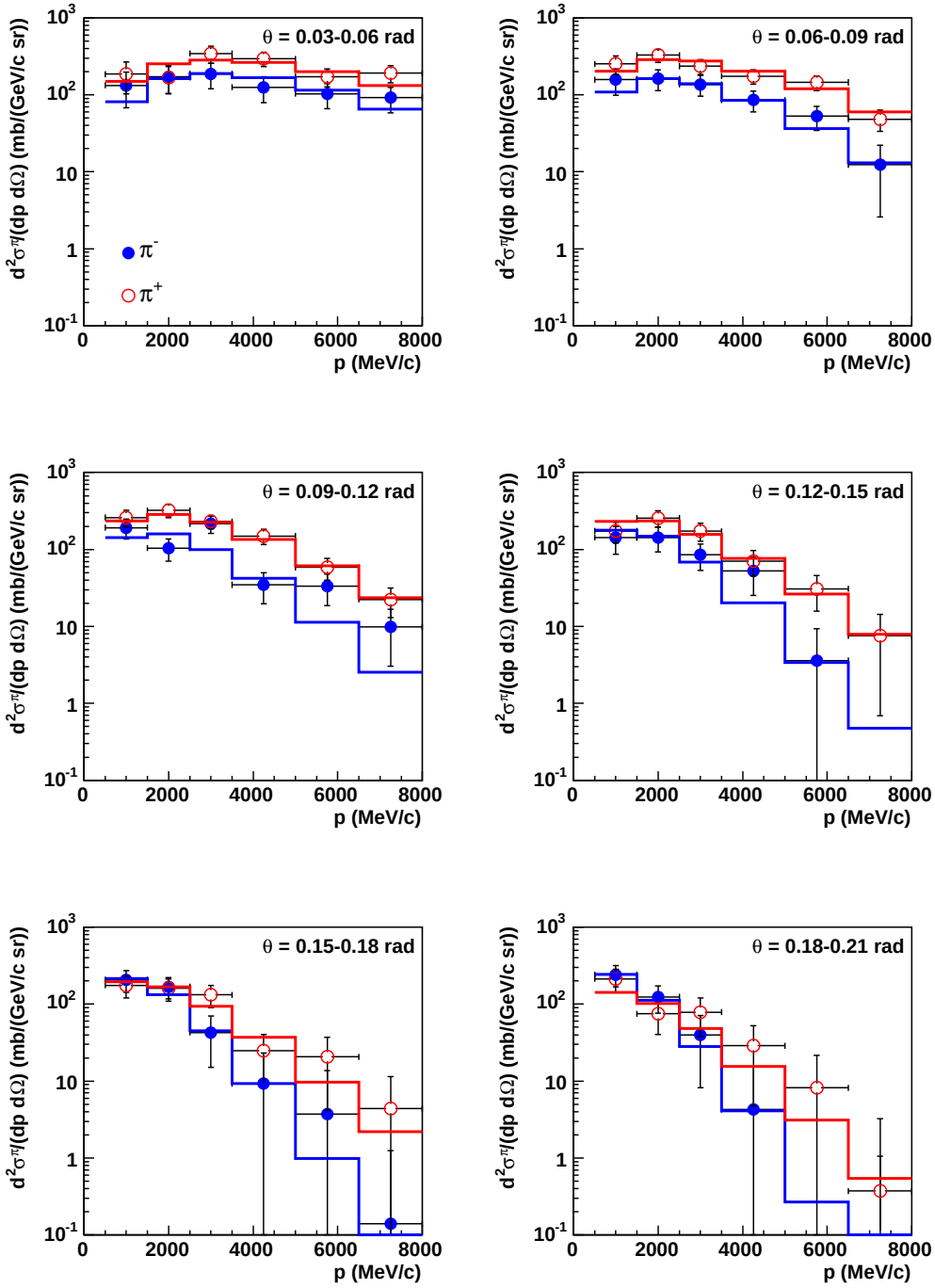

Figure 5.14: Sanford-Wang parametrization for pion momentum spectra in π^++C reactions at 12 GeV/c.

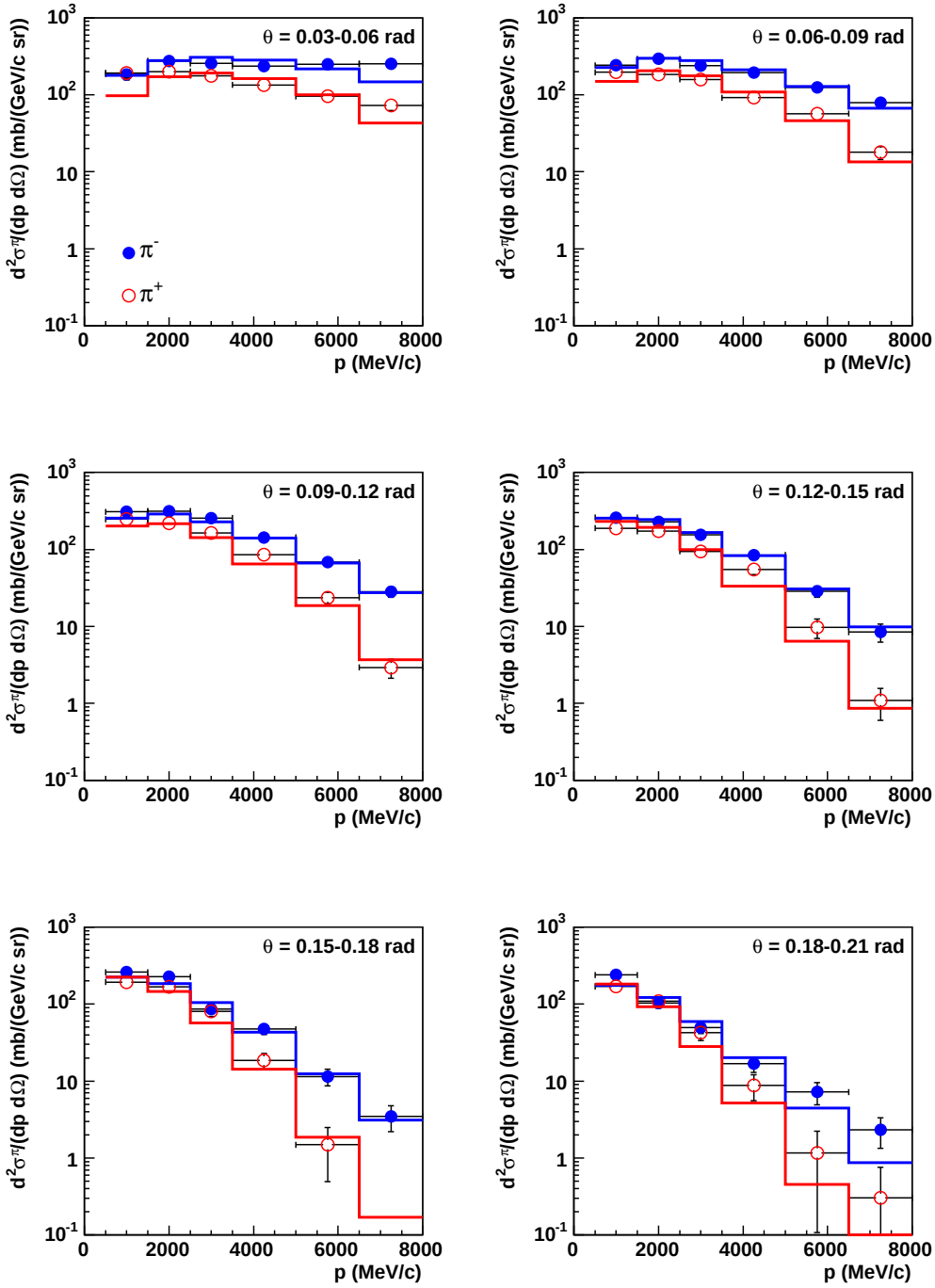

Figure 5.15: Sanford-Wang parametrization for pion momentum spectra in π^-+C reactions at 12 GeV/c.

6 Discussion of HARP data

6.1 Comparison of p+C HARP data at 12 GeV/c with model predictions

A comparison of π^- and π^+ momentum spectra produced in p+C reactions at 12 GeV/c with different model predictions is shown in Fig. 6.1 and Fig. 6.2. The spectra are plotted with linear scale to make deviations between data and models more visible at low momenta. The three hadronic interaction models are GHEISHA [21], UrQMD [32] and DPMJET-III [36]. These are models typically used in air shower simulations. GHEISHA and UrQMD are implemented in CORSIKA as low energy models (below 80 GeV), whereas DPMJET-III is mostly used at higher energies but is also able to make predictions at lower energies. Comparing the predictions of these models to the measured data, distinct discrepancies at low and high momenta become visible. Especially the decrease of the cross-section to very low momenta is not well described by the models. For π^+, the prediction of DPMJET-III seems relatively good, however, DPMJET-III underestimates the π^- production at low momenta. At large momenta the three models are more similar to each other, but none of the models provides an acceptable description of the data.

As already mentioned in section 5.7, for tuning and modifying models, often a parametrization of data like the Sanford-Wang formula [91] is used. This is a suitable method to interpolate between measured energy and phase space regions. However, this method has some shortcomings. The reliability of parametrizations for extrapolating to energy and phase space regions where no data are given is unclear.

Fig. 6.3 shows a comparison of π^- and π^+ momentum spectra in p+C reactions with a continuous Sanford-Wang fit [91]. Concluding from this comparison, at high momenta and in particular at large angles, the parametrization does not describe the data very well. Especially for π^+ momentum spectra at angles larger than 0.18 rad, the Sanford-Wang fit deviates considerably from the data and should not be used in an angular range above 0.18 rad.

Physics wise a very similar behaviour of π^+ and π^- spectra are expected at low secondary momenta, because at low momenta the leading particle effect is not dominant. This is confirmed by the DPMJET-III predictions, see Fig. 6.4 (top panel). However, the Sanford-Wang parametrization significantly differs between π^+ and π^-, see Fig. 6.4 (bottom panel), which might be a technical artifact as there are no data in this range. This indicates that the Sanford-Wang parametrization should not be extrapolated to low momenta.

To consider the comparison of the Sanford-Wang parametrization and DPMJET model predictions, in Fig. 6.5 and Fig. 6.6 the predictions of DPMJET-III for π^- and π^+ momentum spectra is shown together with their Sanford-Wang parametrization for several angular bins. For large angles the spectra predicted by DPMJET-III are harder than the parametrization of the data.

This comparison shows that parametrizations such as the Sanford-Wang fit have to be used with caution. One can not expect that this parametrization gives a reliable extrapolation to unmeasured phase space regions.

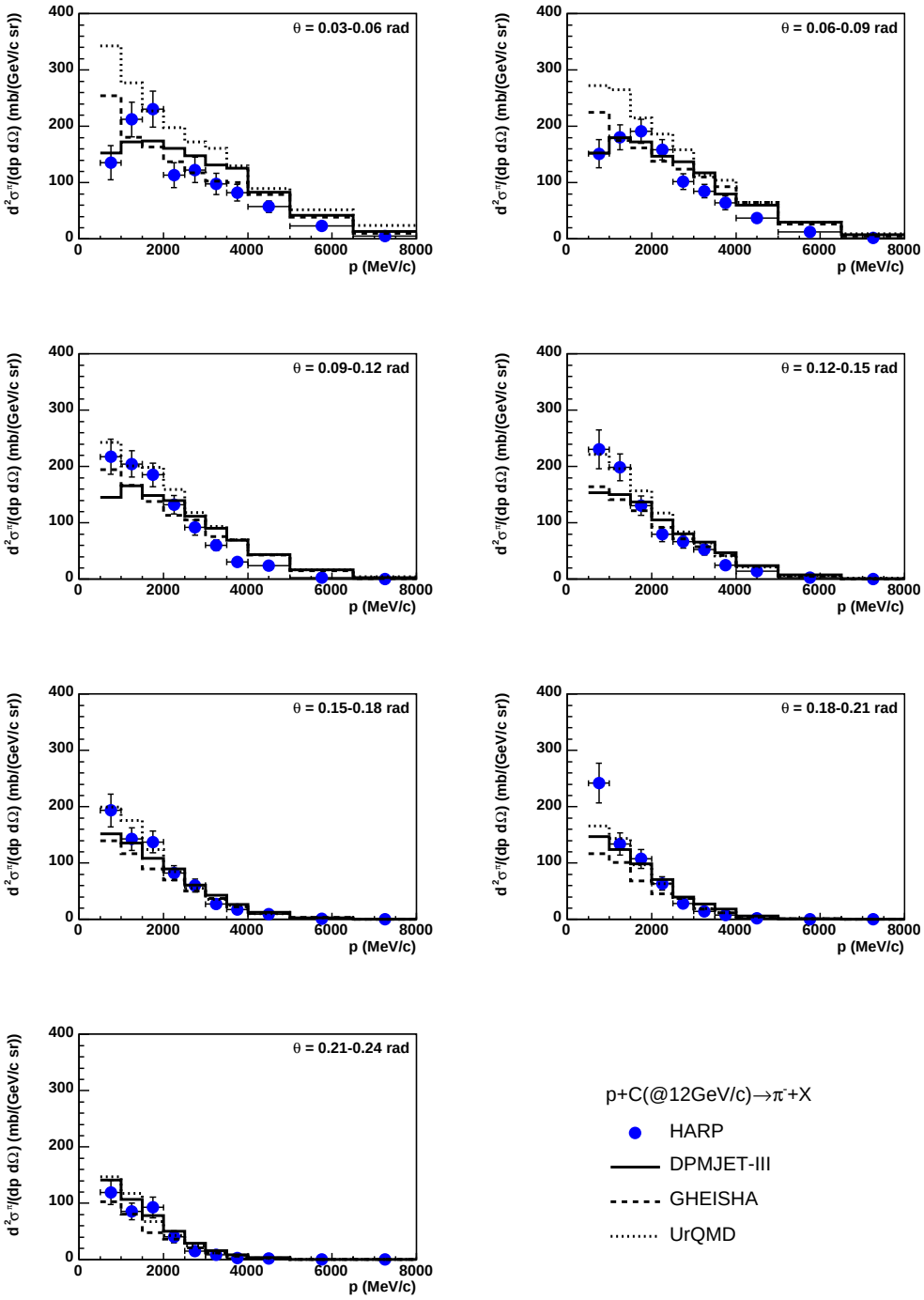

Figure 6.1: Comparison of π^- momentum spectra in p+C reactions at 12 GeV/c with model predictions.

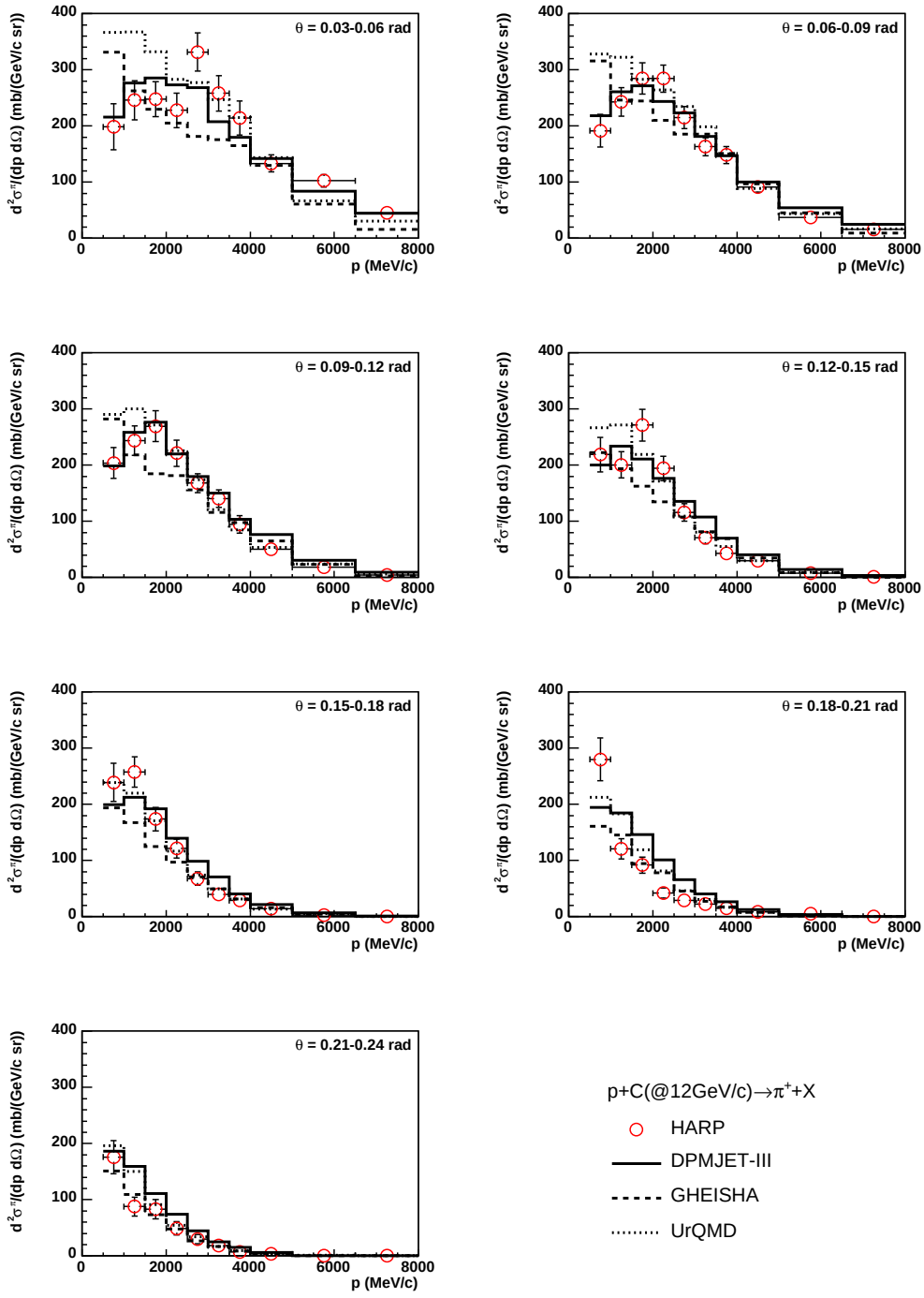

Figure 6.2: Comparison of π^+ momentum spectra in p+C reactions at 12 GeV/c with model predictions.

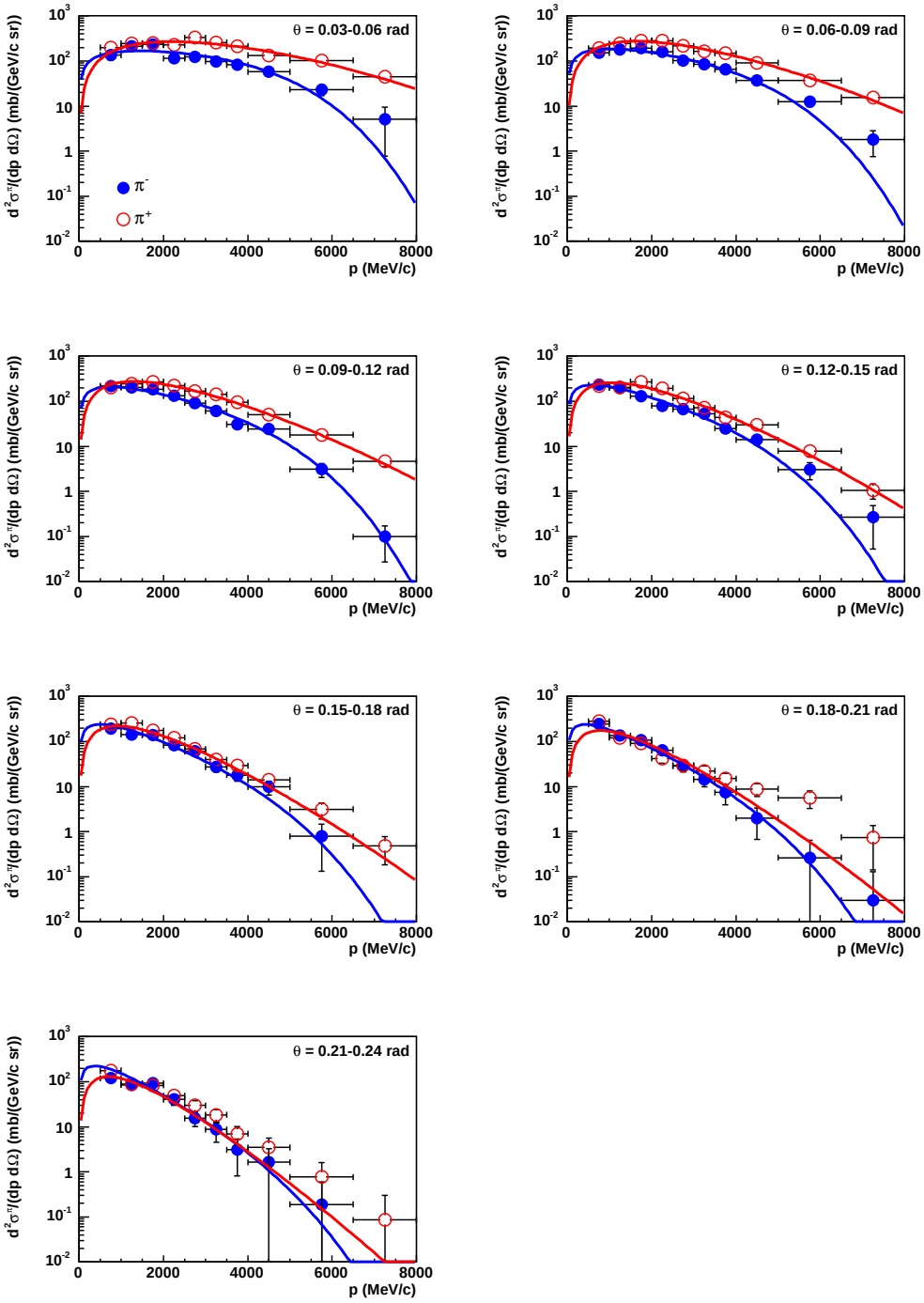

Figure 6.3: Continuous Sanford-Wang fit for pion momentum spectra in p+C reactions at 12 GeV/c.

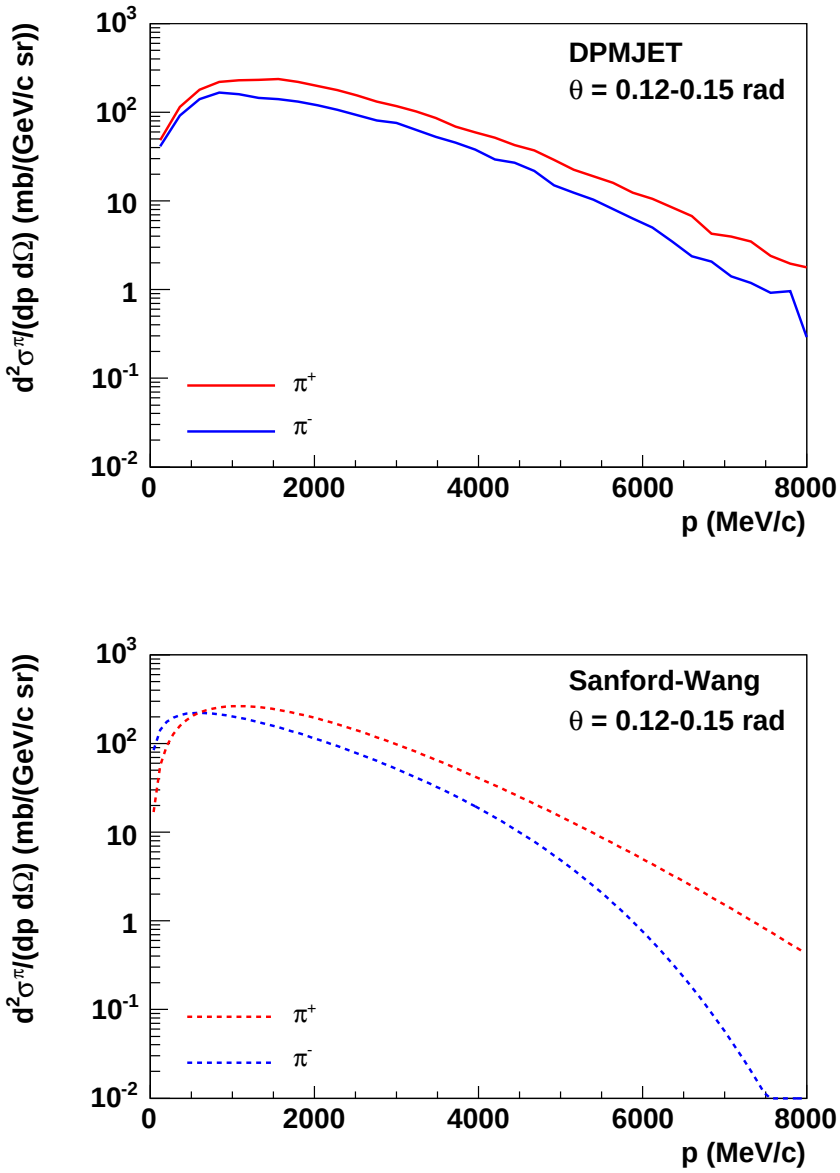

Figure 6.4: Comparison of DPMJET model predictions (top panel) of π^+ and π^- momentum spectra and the Sanford-Wang parametrization of the data (bottom panel). In the chosen angular range (0.12-0.15 rad) the Sanford-Wang fit differs distinctly for π^+ and π^- at low momenta.

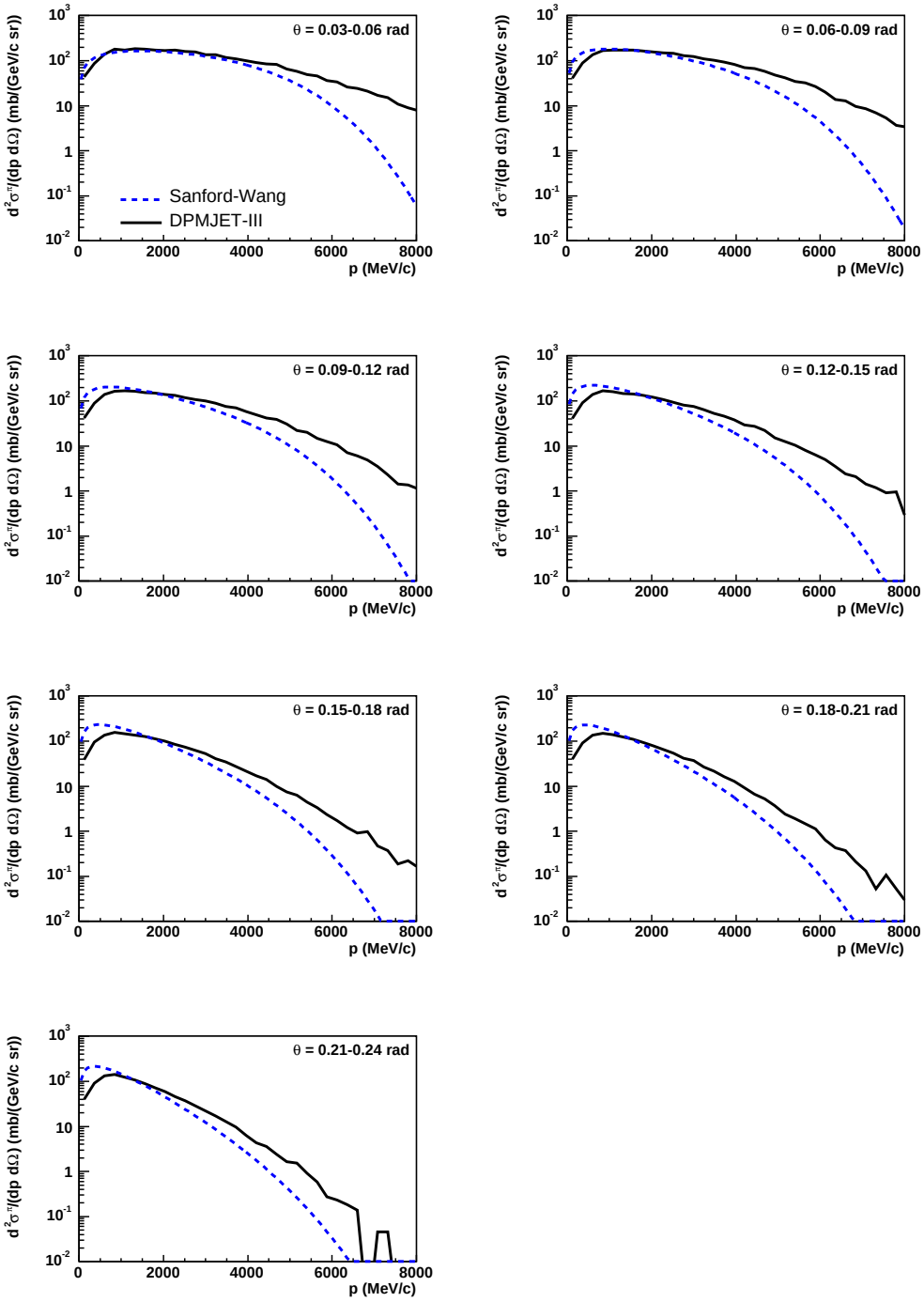

Figure 6.5: Comparison of Sanford-Wang parametrization for π^- momentum spectra in p+C reactions with predictions of DPMJET-III model.

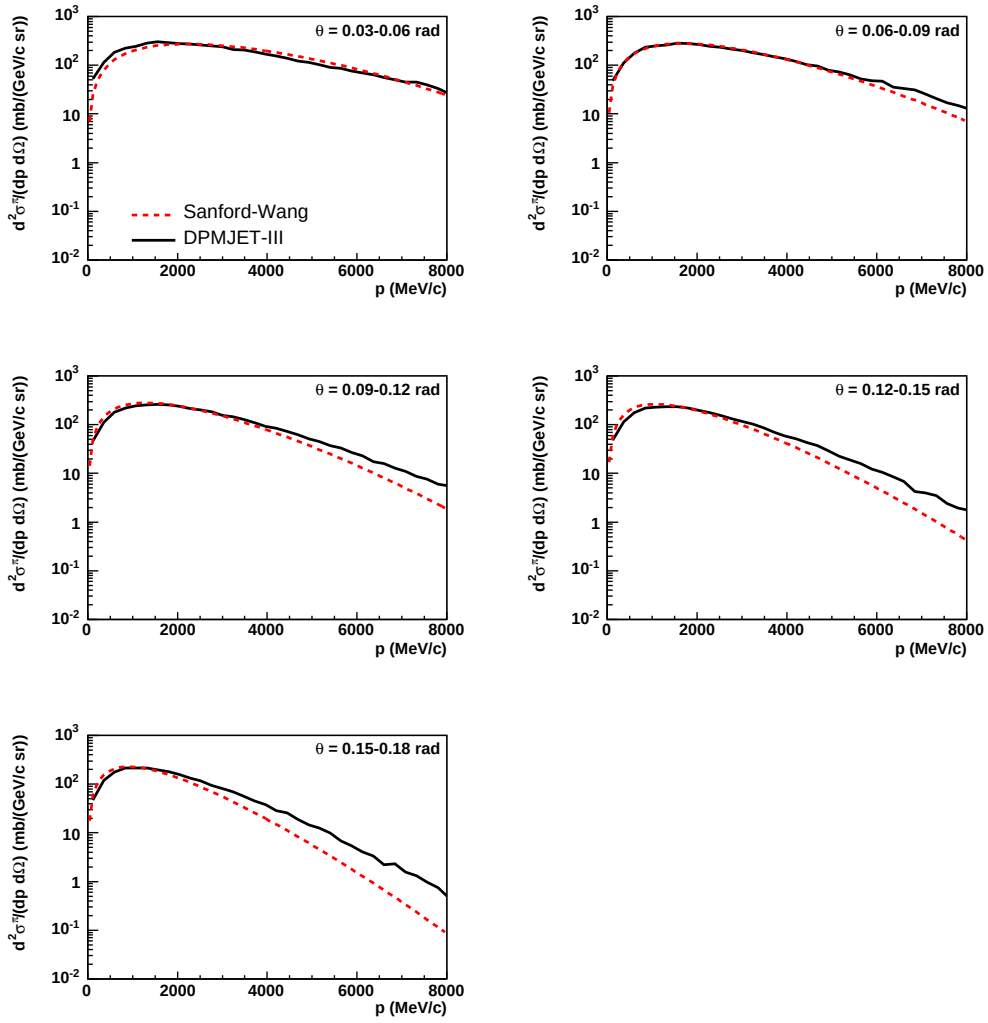

Figure 6.6: Comparison of Sanford-Wang parametrization for π^+ momentum spectra in p+C reactions with predictions of DPMJET-III model. Due to the considerable deviation of the Sanford-Wang parametrization from the data for angles larger than 0.18 rad, these spectra are not shown.

6.2 Comparison of p+C data with preliminary p+O_2 and p+N_2 data

For completeness in the following first, very preliminary results on pion production in p+N_2 and p+O_2 at 12 GeV/c [92] measured by HARP are shown, which became available just prior to submitting this thesis. These reactions are more difficult to provide by experiments, because fluid targets are more complicated to handle and even the analysis of those data is more complex. Still, the analysis is based on the analysis tools developed in this thesis and described for p+C data in chapter 5.

Fig. 6.7 and Fig. 6.8 show a compilation of π^- and π^+ momentum spectra in p+C, p+N_2 and p+O_2 for four angular regions. Due to the lower statistics, a coarser binning for p+N_2 and p+O_2 data is chosen in relation to the binning used for the p+C analysis in chapter 5 and the binning of p+C data is adapted for this comparison. The spectra look very similar for the different reactions. The shape of the spectra are nearly identical, only a different normalization factor can be noticed because of the different nuclear masses of the target materials. This result confirms the model predictions for p+C and p+air reactions, see Fig. 3.7 and Fig. 3.8 (p. 29).

This is an important result for future planned experiments needed for measuring reference data for cosmic ray physics. Owing to the agreement of pion production in reactions of protons with air nuclei (N_2 and O_2) and the pion production in p+C reactions, solid carbon targets, which are easier to handle, can often be used instead.

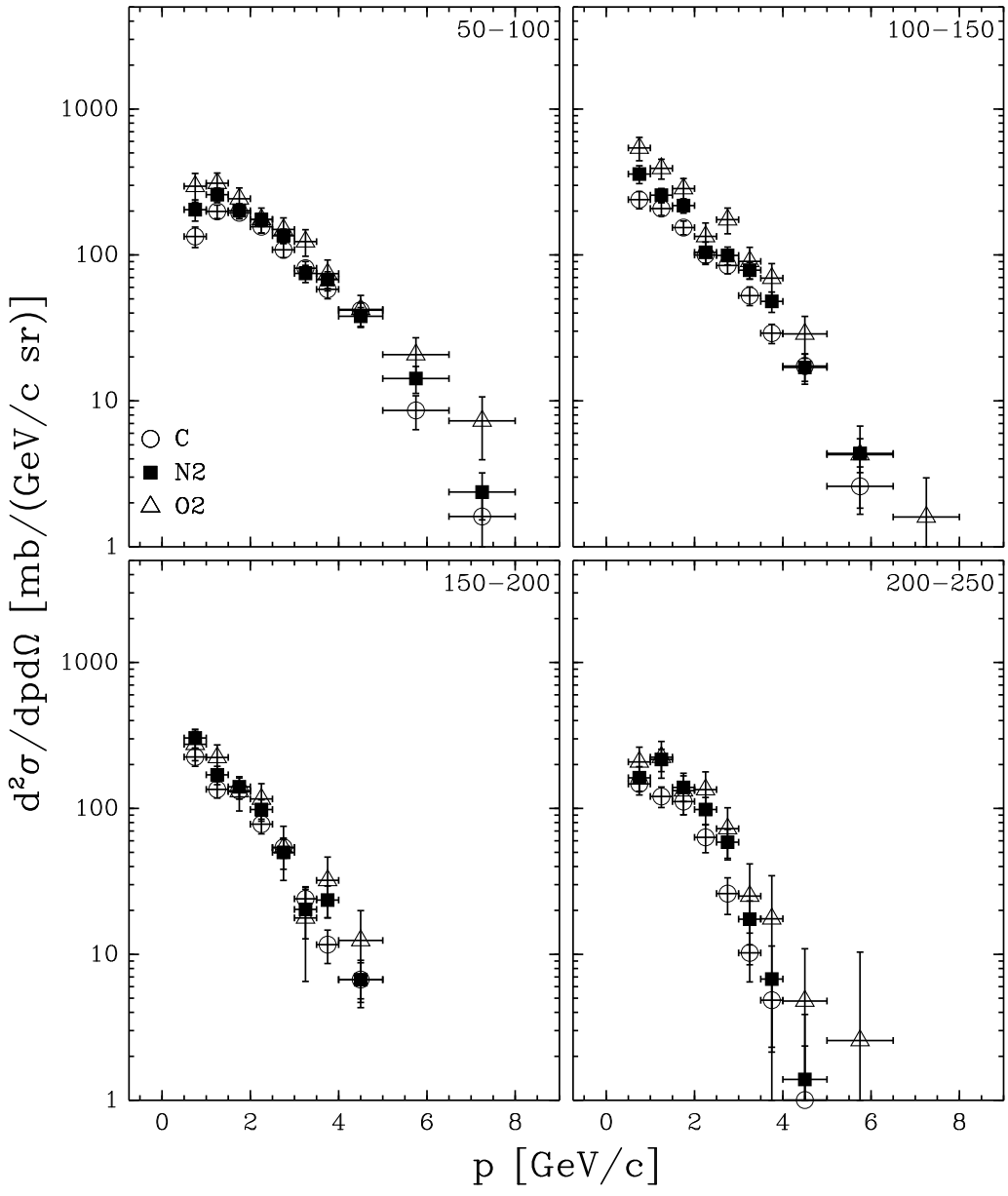

Figure 6.7: Comparison of π^- momentum spectra in p+C reactions at 12 GeV/c with π^- momentum spectra in p+N_2 and p+O_2 reactions at the same energy. Angular range from upper left to lower right: 50-100 mrad, 100-150 mrad, 150-200 mrad, 200-250 mrad.

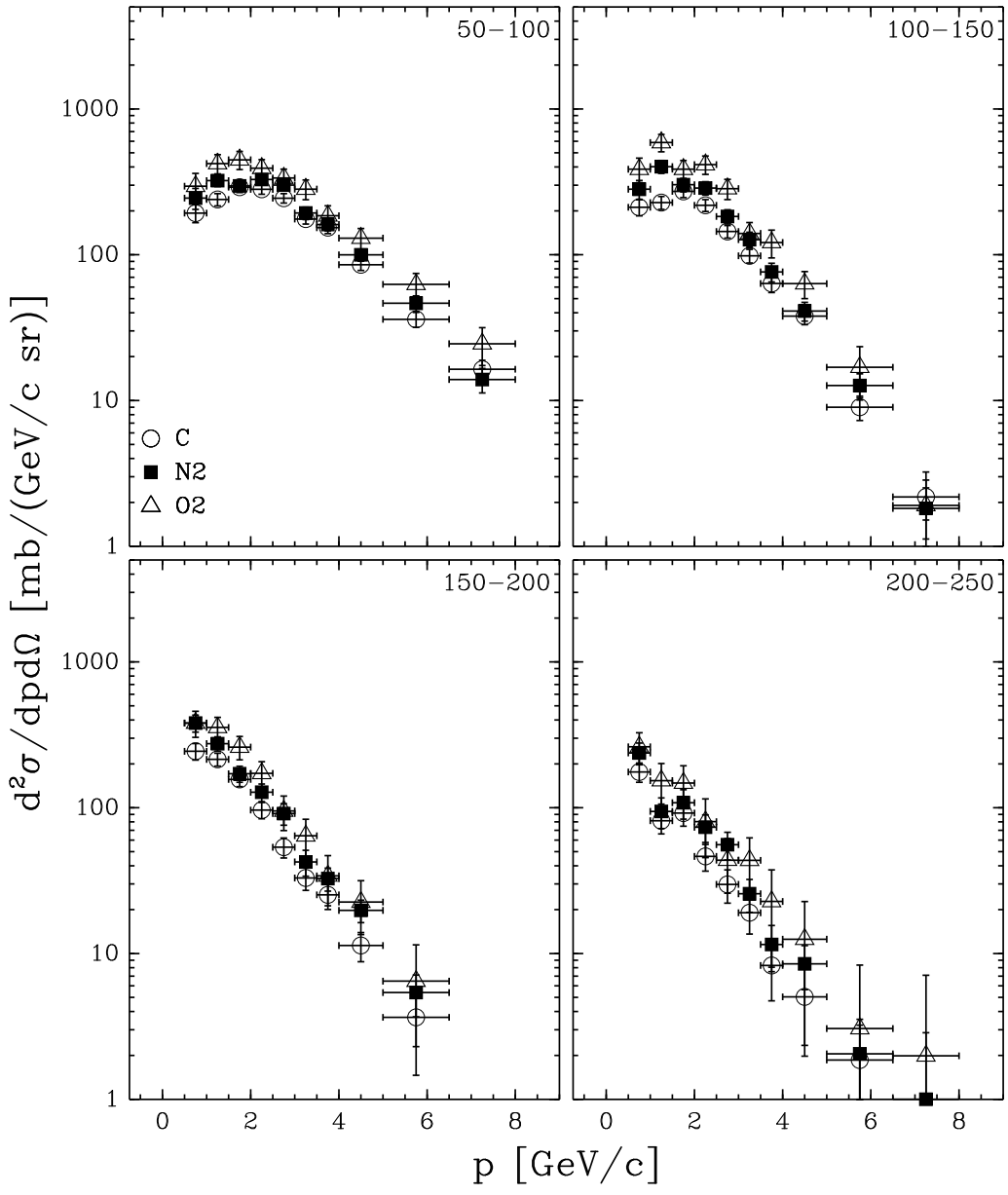

Figure 6.8: Comparison of π^+ momentum spectra in p+C reactions at 12 GeV/c with π^+ momentum spectra in p+N_2 and p+O_2 reactions at the same energy. Angular range from upper left to lower right: 50-100 mrad, 100-150 mrad, 150-200 mrad, 200-250 mrad.

7 Conclusions and outlook

The results reported in this thesis contribute to the improvement of our understanding of EAS simulations and hadronic interactions at low energy. They will help to improve the reliability of the interpretation of measurements of air shower arrays.

Using simulations of showers in the knee energy range made with a modified version of the air shower simulation package CORSIKA, the hadronic interactions in an EAS are studied which are important for the muon production in EAS. Most of the muons are generated as decay products of charged pions and kaons at an altitude of about 5 km. About five consecutive hadronic interactions in an EAS take place before a meson decays into a muon. Most frequently the hadron initiating the hadronic interaction, in which a meson leading to a muon is produced, is a charged pion and about 21% of this interactions are initiated by nucleons. The most important energy range of these reactions is from about 10 to 1000 GeV, whereas the phase space of importance for muon production covers the most forward direction ($y/y_{\text{beam}} = 0.3 - 1.1$, $p_t = 0 - 1\text{GeV}/c$).

These energy and phase space regions are accessible by fixed target experiments. By surveying all existing data, it has been shown that most of experiments done in the past were using proton beams on beryllium targets and that their data are very limited in statistics and phase space coverage. In 2006 p+C data provided by the CERN experiment NA49 have become available in a large acceptance range. Within the work of this thesis, measurements of p+C, π^++C and π^-+C interactions at 12 GeV/c have been added to the available data sets with a carbon target. As simulations show that collisions of protons with a carbon target are very similar to p+air interactions, these data sets can be used for tuning models needed in astroparticle physics simulations.

The fixed target experiment HARP at the PS accelerator at CERN has been shown to be ideally suited for the measurement of hadron production using proton and pion beams with momenta between 1.5 and 15 GeV/c and various targets from light to heavier elements. Due to the fact that the HARP apparatus consists of two parts, a forward and a large angle spectrometer, it covers nearly the complete secondary particle phase space.

A central part of this thesis is the analysis of p+C, π^++C and π^-+C data at 12 GeV/c measured with the HARP spectrometer. The p+C data cover secondary momenta of π^+ and π^- from 0.5 GeV/c to 8 GeV/c and an angular range from 30 mrad to 240 mrad, whereas the π+C data have an angular acceptance from 30 mrad to 210 mrad. After calibrating the momentum reconstruction of the HARP forward spectrometer, momentum spectra of π^- and π^+ are derived for different angular bins and with statistical and systematic error of the order of less than 10% in the most important regions. For the latter a detailed analysis of systematic errors has been performed.

To check the reliability of hadronic interaction models which are used for air shower simulations, the spectra are compared to predictions of these models. None of the models is able to describe satisfactorily and in detail the measured spectra. Discrepancies are found especially at low and high momenta.

Many models rely on parametrizations of accelerator data. Therefore a Sanford-Wang parametrization is given for all measured spectra. From the comparison of the Sanford-Wang fits with model predictions it is concluded that a very careful use of such parametrizations is advisable, if the parametrization is extrapolated to regions where no data are measured.

The p+C data at 12 GeV/c are compared to first, very preliminary results from an analysis of HARP data on p+N_2 and p+O_2 at the same energy. The comparison shows that indeed secondary momentum spectra of π^+ and π^- of p+C and p+N_2 (p+O_2) reactions are nearly identical up to the overall cross-section normalization. This shows that for future experiments, which are planned to measure reference data for cosmic ray physics, carbon targets are a good replacement for the difficult to handle gaseous or liquid N_2 or O_2 targets.

Finally, it should be mentioned that the presented simulation studies of the properties of hadronic interactions in EAS, which are of importance for the muon production, formed the basis on the cosmic ray part of the proposal of using the former NA49 detector for a new fixed target experiment. Early this year the proposal was accepted by CERN and the new NA61 experiment will take first p+C data at 30 GeV in autumn of 2007. The foreseen measurements of importance for astroparticle physics are reactions of p+C at the energies 30, 40, 50 and 400 GeV and π+C at 158 and 400 GeV.

A Additional information on HARP data

A.1 Tables of cross-section for π^+ and π^- production in p+C, π^++C and π^-+C reactions at 12 GeV/c

$\theta_{\min}$ (mrad)	$\theta_{\max}$ (mrad)	$p_{\min}$ (GeV/c)	$p_{\max}$ (GeV/c)	$d^2\sigma^{\pi^+}/(dpd\Omega)$ (mb/(GeV/c sr))
30	60	0.5	1.0	198.5 ± 40.8
		1.0	1.5	245.8 ± 35.0
		1.5	2.0	248.2 ± 31.1
		2.0	2.5	227.9 ± 31.0
		2.5	3.0	331.6 ± 34.2
		3.0	3.5	258.2 ± 31.4
		3.5	4.0	214.1 ± 30.5
		4.0	5.0	133.5 ± 15.1
		5.0	6.5	102.6 ± 11.0
		6.5	8.0	45.2 ± 7.8
60	90	0.5	1.0	191.7 ± 29.1
		1.0	1.5	243.2 ± 25.4
		1.5	2.0	284.9 ± 27.9
		2.0	2.5	284.4 ± 24.3
		2.5	3.0	214.9 ± 19.8
		3.0	3.5	163.1 ± 15.8
		3.5	4.0	148.4 ± 15.2
		4.0	5.0	91.4 ± 9.3
		5.0	6.5	36.9 ± 5.0
		6.5	8.0	15.6 ± 2.7
90	120	0.5	1.0	204.0 ± 27.8
		1.0	1.5	243.7 ± 26.2
		1.5	2.0	269.4 ± 27.7
		2.0	2.5	221.3 ± 23.4
		2.5	3.0	168.0 ± 17.0
		3.0	3.5	140.5 ± 15.2
		3.5	4.0	94.8 ± 15.6
		4.0	5.0	50.2 ± 6.3
		5.0	6.5	18.0 ± 2.9
		6.5	8.0	4.7 ± 1.2
120	150	0.5	1.0	218.8 ± 30.6
		1.0	1.5	200.6 ± 23.4
		1.5	2.0	271.3 ± 28.5
		2.0	2.5	194.3 ± 21.6
		2.5	3.0	115.7 ± 15.6
		3.0	3.5	71.0 ± 10.7
		3.5	4.0	43.4 ± 7.4
		4.0	5.0	29.9 ± 5.0
		5.0	6.5	7.9 ± 2.1
		6.5	8.0	1.1 ± 0.4

θ_{min} (mrad)	θ_{max} (mrad)	p_{min} (GeV/c)	p_{max} (GeV/c)	$d^2\sigma^{\pi^+}/(dpd\Omega)$ (mb/(GeV/c sr))
150	180	0.5	1.0	238.9 ± 34.1
		1.0	1.5	257.5 ± 26.9
		1.5	2.0	173.7 ± 20.8
		2.0	2.5	121.3 ± 16.7
		2.5	3.0	67.9 ± 11.8
		3.0	3.5	39.7 ± 7.4
		3.5	4.0	28.9 ± 6.3
		4.0	5.0	14.1 ± 3.5
		5.0	6.5	3.1 ± 1.2
		6.5	8.0	0.5 ± 0.3
180	210	0.5	1.0	280.1 ± 38.2
		1.0	1.5	121.0 ± 18.2
		1.5	2.0	91.8 ± 14.2
		2.0	2.5	42.0 ± 9.1
		2.5	3.0	29.3 ± 7.1
		3.0	3.5	22.2 ± 6.1
		3.5	4.0	15.1 ± 4.5
		4.0	5.0	8.9 ± 2.9
		5.0	6.5	5.6 ± 2.3
		6.5	8.0	0.7 ± 0.6
210	240	0.5	1.0	175.8 ± 29.2
		1.0	1.5	87.9 ± 16.8
		1.5	2.0	82.8 ± 17.1
		2.0	2.5	49.1 ± 11.7
		2.5	3.0	29.9 ± 8.2
		3.0	3.5	18.3 ± 6.1
		3.5	4.0	7.0 ± 3.1
		4.0	5.0	3.5 ± 2.2
		5.0	6.5	0.8 ± 0.8
		6.5	8.0	0.1 ± 0.2

Table A.1: HARP results for the double-differential π^+ production cross-section in the laboratory system, $d^2\sigma^{\pi^+}/(dpd\Omega)$, for p+C interactions at 12 GeV/c. Each row refers to a different $(p_{\mathrm{min}} \leq p < p_{\mathrm{max}}, \theta_{\mathrm{min}} \leq \theta < \theta_{\mathrm{max}})$ bin, where p and θ are the pion momentum and polar angle, respectively. The central value as well as the square-root of the diagonal elements of the covariance matrix are given.

$\theta_{\min}$ (mrad)	$\theta_{\max}$ (mrad)	$p_{\min}$ (GeV/c)	$p_{\max}$ (GeV/c)	$d^2\sigma^{\pi^-}/(dpd\Omega)$ (mb/(GeV/c sr))
30	60	0.5	1.0	135.4 ± 30.5
		1.0	1.5	212.5 ± 30.8
		1.5	2.0	230.6 ± 32.1
		2.0	2.5	113.6 ± 21.9
		2.5	3.0	122.6 ± 22.6
		3.0	3.5	98.1 ± 18.9
		3.5	4.0	82.3 ± 14.8
		4.0	5.0	57.5 ± 10.4
		5.0	6.5	23.2 ± 6.2
		6.5	8.0	5.1 ± 4.3
60	90	0.5	1.0	151.3 ± 24.9
		1.0	1.5	180.6 ± 22.0
		1.5	2.0	191.6 ± 21.3
		2.0	2.5	158.2 ± 18.0
		2.5	3.0	101.7 ± 14.0
		3.0	3.5	85.1 ± 12.0
		3.5	4.0	64.5 ± 12.2
		4.0	5.0	37.2 ± 5.5
		5.0	6.5	12.5 ± 2.8
		6.5	8.0	1.8 ± 1.0
90	120	0.5	1.0	217.4 ± 31.2
		1.0	1.5	204.7 ± 23.2
		1.5	2.0	185.1 ± 21.0
		2.0	2.5	132.1 ± 16.5
		2.5	3.0	91.8 ± 13.8
		3.0	3.5	60.5 ± 9.2
		3.5	4.0	30.7 ± 5.1
		4.0	5.0	24.4 ± 5.2
		5.0	6.5	3.1 ± 1.1
		6.5	8.0	0.1 ± 0.1
120	150	0.5	1.0	230.5 ± 34.5
		1.0	1.5	198.9 ± 23.7
		1.5	2.0	130.7 ± 17.4
		2.0	2.5	79.7 ± 12.7
		2.5	3.0	66.7 ± 11.3
		3.0	3.5	52.5 ± 9.6
		3.5	4.0	24.9 ± 5.2
		4.0	5.0	14.0 ± 3.5
		5.0	6.5	3.1 ± 1.3
		6.5	8.0	0.3 ± 0.2

θ_{min} (mrad)	θ_{max} (mrad)	p_{min} (GeV/c)	p_{max} (GeV/c)	$d^2\sigma^{\pi^-}/(dpd\Omega)$ (mb/(GeV/c sr))		
150	180	0.5	1.0	193.4	$\pm$	28.9
		1.0	1.5	142.8	$\pm$	20.0
		1.5	2.0	137.6	$\pm$	19.3
		2.0	2.5	82.1	$\pm$	13.1
		2.5	3.0	60.2	$\pm$	11.2
		3.0	3.5	27.3	$\pm$	6.2
		3.5	4.0	17.9	$\pm$	5.0
		4.0	5.0	9.8	$\pm$	3.3
		5.0	6.5	0.8	$\pm$	0.7
		6.5	8.0	0.005	$\pm$	0.018
180	210	0.5	1.0	242.0	$\pm$	35.1
		1.0	1.5	134.0	$\pm$	19.8
		1.5	2.0	107.6	$\pm$	16.8
		2.0	2.5	63.7	$\pm$	11.9
		2.5	3.0	28.4	$\pm$	7.2
		3.0	3.5	14.4	$\pm$	4.6
		3.5	4.0	7.4	$\pm$	3.4
		4.0	5.0	2.0	$\pm$	1.3
		5.0	6.5	0.3	$\pm$	0.4
		6.5	8.0	0.03	$\pm$	0.1
210	240	0.5	1.0	119.4	$\pm$	21.3
		1.0	1.5	85.4	$\pm$	14.9
		1.5	2.0	92.6	$\pm$	18.4
		2.0	2.5	40.3	$\pm$	10.6
		2.5	3.0	15.5	$\pm$	5.4
		3.0	3.5	8.7	$\pm$	4.2
		3.5	4.0	3.1	$\pm$	2.3
		4.0	5.0	1.6	$\pm$	1.6
		5.0	6.5	0.2	$\pm$	0.4
		6.5	8.0	0.001	$\pm$	0.013

Table A.2: HARP results for the double-differential π^- production cross-section in the laboratory system, $d^2\sigma^{\pi^-}/(dpd\Omega)$, for p+C interactions at 12 GeV/c. Each row refers to a different $(p_{\mathrm{min}} \leq p < p_{\mathrm{max}}, \theta_{\mathrm{min}} \leq \theta < \theta_{\mathrm{max}})$ bin, where p and θ are the pion momentum and polar angle, respectively. The central value as well as the square-root of the diagonal elements of the covariance matrix are given.

θ_{min} (mrad)	θ_{max} (mrad)	p_{min} (GeV/c)	p_{max} (GeV/c)	$d^2\sigma^{\pi^+}/(dpd\Omega)$ (mb/(GeV/c sr))
30	60	0.5	1.5	186.1 ± 82.6
		1.5	2.5	168.1 ± 63.3
		2.5	3.5	344.1 ± 85.9
		3.5	5.0	293.6 ± 61.9
		5.0	6.5	172.8 ± 45.6
		6.5	8.0	191.3 ± 47.2
60	90	0.5	1.5	251.8 ± 68.7
		1.5	2.5	327.7 ± 64.0
		2.5	3.5	236.2 ± 52.4
		3.5	5.0	174.4 ± 36.4
		5.0	6.5	145.5 ± 31.9
		6.5	8.0	48.3 ± 14.9
90	120	0.5	1.5	260.6 ± 63.1
		1.5	2.5	322.7 ± 63.5
		2.5	3.5	230.8 ± 46.1
		3.5	5.0	148.8 ± 33.6
		5.0	6.5	58.5 ± 18.4
		6.5	8.0	22.4 ± 9.4
120	150	0.5	1.5	173.9 ± 53.2
		1.5	2.5	256.8 ± 60.1
		2.5	3.5	173.2 ± 45.0
		3.5	5.0	71.0 ± 25.5
		5.0	6.5	30.9 ± 15.1
		6.5	8.0	7.5 ± 6.8
150	180	0.5	1.5	176.0 ± 54.7
		1.5	2.5	161.1 ± 52.1
		2.5	3.5	132.4 ± 42.8
		3.5	5.0	25.0 ± 15.6
		5.0	6.5	20.7 ± 16.5
		6.5	8.0	4.4 ± 7.1
180	210	0.5	1.5	212.9 ± 71.3
		1.5	2.5	75.0 ± 34.6
		2.5	3.5	78.9 ± 40.9
		3.5	5.0	28.7 ± 24.0
		5.0	6.5	8.2 ± 13.4
		6.5	8.0	0.4 ± 2.9

Table A.3: HARP results for the double-differential π^+ production cross-section in the laboratory system, $d^2\sigma^{\pi^+}/(dpd\Omega)$, for π^++C interactions at 12 GeV/c. Each row refers to a different $(p_{\mathrm{min}} \leq p < p_{\mathrm{max}}, \theta_{\mathrm{min}} \leq \theta < \theta_{\mathrm{max}})$ bin, where p and θ are the pion momentum and polar angle, respectively. The central value as well as the square-root of the diagonal elements of the covariance matrix are given.

θ_{min} (mrad)	θ_{max} (mrad)	p_{min} (GeV/c)	p_{max} (GeV/c)	$d^2\sigma^{\pi^-}/(dpd\Omega)$ (mb/(GeV/c sr))
30	60	0.5	1.5	132.9 ± 64.6
		1.5	2.5	172.6 ± 69.3
		2.5	3.5	187.9 ± 68.2
		3.5	5.0	125.4 ± 46.1
		5.0	6.5	103.1 ± 37.2
		6.5	8.0	92.1 ± 33.4
60	90	0.5	1.5	157.4 ± 58.8
		1.5	2.5	161.5 ± 48.8
		2.5	3.5	136.7 ± 41.3
		3.5	5.0	85.7 ± 25.7
		5.0	6.5	52.6 ± 18.3
		6.5	8.0	12.3 ± 9.7
90	120	0.5	1.5	192.1 ± 55.9
		1.5	2.5	104.3 ± 33.6
		2.5	3.5	216.0 ± 53.6
		3.5	5.0	34.8 ± 15.0
		5.0	6.5	33.4 ± 14.8
		6.5	8.0	9.9 ± 6.8
120	150	0.5	1.5	143.3 ± 56.2
		1.5	2.5	142.8 ± 50.1
		2.5	3.5	85.8 ± 32.1
		3.5	5.0	52.7 ± 27.3
		5.0	6.5	3.6 ± 5.7
		6.5	8.0	0.1 ± 0.4
150	180	0.5	1.5	207.8 ± 64.7
		1.5	2.5	168.6 ± 52.2
		2.5	3.5	42.8 ± 27.6
		3.5	5.0	9.2 ± 13.8
		5.0	6.5	3.7 ± 9.9
		6.5	8.0	0.1 ± 1.1
180	210	0.5	1.5	241.5 ± 74.0
		1.5	2.5	124.2 ± 48.1
		2.5	3.5	39.8 ± 31.6
		3.5	5.0	4.3 ± 11.3
		5.0	6.5	0.01 ± 0.26

Table A.4: HARP results for the double-differential π^- production cross-section in the laboratory system, $d^2\sigma^{\pi^-}/(dpd\Omega)$, for π^++C interactions at 12 GeV/c. Each row refers to a different $(p_{\mathrm{min}} \leq p < p_{\mathrm{max}}, \theta_{\mathrm{min}} \leq \theta < \theta_{\mathrm{max}})$ bin, where p and θ are the pion momentum and polar angle, respectively. The central value as well as the square-root of the diagonal elements of the covariance matrix are given.

θ_{min} (mrad)	θ_{max} (mrad)	p_{min} (GeV/c)	p_{max} (GeV/c)	$d^2\sigma^{\pi^+}/(dpd\Omega)$ (mb/(GeV/c sr))
30	60	0.5	1.5	192.6 ± 27.9
		1.5	2.5	201.0 ± 23.5
		2.5	3.5	176.9 ± 21.6
		3.5	5.0	134.1 ± 14.9
		5.0	6.5	95.7 ± 11.0
		6.5	8.0	72.4 ± 10.1
60	90	0.5	1.5	196.2 ± 21.1
		1.5	2.5	183.9 ± 17.6
		2.5	3.5	158.5 ± 14.2
		3.5	5.0	92.0 ± 8.8
		5.0	6.5	56.9 ± 6.9
		6.5	8.0	17.9 ± 3.5
90	120	0.5	1.5	247.1 ± 25.4
		1.5	2.5	220.1 ± 19.9
		2.5	3.5	164.3 ± 15.5
		3.5	5.0	85.9 ± 9.7
		5.0	6.5	23.7 ± 4.0
		6.5	8.0	2.9 ± 0.8
120	150	0.5	1.5	189.7 ± 21.0
		1.5	2.5	172.4 ± 18.5
		2.5	3.5	94.4 ± 11.5
		3.5	5.0	54.6 ± 7.5
		5.0	6.5	9.8 ± 2.8
		6.5	8.0	1.1 ± 0.5
150	180	0.5	1.5	193.3 ± 22.5
		1.5	2.5	168.3 ± 18.7
		2.5	3.5	80.3 ± 11.5
		3.5	5.0	18.5 ± 4.5
		5.0	6.5	1.5 ± 1.0
		6.5	8.0	0.02 ± 0.04
180	210	0.5	1.5	170.2 ± 21.4
		1.5	2.5	109.4 ± 15.0
		2.5	3.5	42.5 ± 8.8
		3.5	5.0	8.8 ± 3.2
		5.0	6.5	1.2 ± 1.1
		6.5	8.0	0.3 ± 0.5

Table A.5: HARP results for the double-differential π^+ production cross-section in the laboratory system, $d^2\sigma^{\pi^+}/(dpd\Omega)$, for π^-+C interactions at 12 GeV/c. Each row refers to a different $(p_{\mathrm{min}} \leq p < p_{\mathrm{max}}, \theta_{\mathrm{min}} \leq \theta < \theta_{\mathrm{max}})$ bin, where p and θ are the pion momentum and polar angle, respectively. The central value as well as the square-root of the diagonal elements of the covariance matrix are given.

θ_{min} (mrad)	θ_{max} (mrad)	p_{min} (GeV/c)	p_{max} (GeV/c)	$d^2\sigma^{\pi^-}/(dpd\Omega)$ (mb/(GeV/c sr))
30	60	0.5	1.5	184.3 ± 27.9
		1.5	2.5	276.9 ± 30.5
		2.5	3.5	256.4 ± 26.3
		3.5	5.0	235.3 ± 19.1
		5.0	6.5	250.5 ± 21.4
		6.5	8.0	253.6 ± 16.9
60	90	0.5	1.5	242.1 ± 25.9
		1.5	2.5	294.0 ± 23.9
		2.5	3.5	240.6 ± 18.3
		3.5	5.0	194.7 ± 13.2
		5.0	6.5	125.6 ± 9.1
		6.5	8.0	78.8 ± 7.9
90	120	0.5	1.5	308.2 ± 32.2
		1.5	2.5	316.4 ± 26.7
		2.5	3.5	256.5 ± 21.4
		3.5	5.0	142.8 ± 12.2
		5.0	6.5	68.2 ± 7.1
		6.5	8.0	28.2 ± 4.1
120	150	0.5	1.5	260.3 ± 29.0
		1.5	2.5	228.7 ± 21.5
		2.5	3.5	155.4 ± 16.1
		3.5	5.0	84.7 ± 10.0
		5.0	6.5	28.8 ± 4.9
		6.5	8.0	8.5 ± 2.2
150	180	0.5	1.5	260.3 ± 29.8
		1.5	2.5	226.5 ± 23.0
		2.5	3.5	86.9 ± 11.7
		3.5	5.0	47.5 ± 7.2
		5.0	6.5	11.5 ± 2.8
		6.5	8.0	3.5 ± 1.3
180	210	0.5	1.5	240.0 ± 28.7
		1.5	2.5	103.1 ± 13.9
		2.5	3.5	50.0 ± 8.5
		3.5	5.0	16.7 ± 3.7
		5.0	6.5	7.2 ± 2.3
		6.5	8.0	2.3 ± 1.0

Table A.6: HARP results for the double-differential π^- production cross-section in the laboratory system, $d^2\sigma^{\pi^-}/(dpd\Omega)$, for π^-+C interactions at 12 GeV/c. Each row refers to a different $(p_{\mathrm{min}} \leq p < p_{\mathrm{max}}, \theta_{\mathrm{min}} \leq \theta < \theta_{\mathrm{max}})$ bin, where p and θ are the pion momentum and polar angle, respectively. The central value as well as the square-root of the diagonal elements of the covariance matrix are given.

A.2 Fit results of Sanford-Wang parametrization

In Tabs. A.7, A.8 and A.9 the results of the Sanford-Wang fit on the π^+ and π^- momentum spectra of p+C, π^++C and π^-+C data are summarized. For these fits the Sanford-Wang function (Eq. (5.7.1) on page 81) has been integrated over momentum and angular bin widths of the data. However, the results are nearly identical to the fit results without integration over individual bins.

Several parameters are strongly correlated resulting in large errors of the extracted parameters. Further assumptions would have to be made to reduce the number of parameters as has been done, for example, in the p+Al and p+Be HARP analyses [81, 85]. This is not done here as the parametrization does not give an adequate description of the spectra at high momenta and large angles.

Table A.7: Sanford-Wang parameters and errors obtained by fitting the p+C dataset.

Parameter	π^-	π^+
c_1	136.12$\pm$ 135.16	143.67$\pm$ 164.87
c_2	0.55 $\pm$ 0.76	1.17 $\pm$ 0.67
c_3	0.24 $\pm$ 2.54	2.46 $\pm$ 1.09
c_4	4.29 $\pm$ 3.16	1.73 $\pm$ 0.42
c_5	2.29 $\pm$ 2.88	1.68 $\pm$ 0.15
c_6	6.22 $\pm$ 3.50	6.90 $\pm$ 3.03
c_7	0.16 $\pm$ 0.17	0.21 $\pm$ 0.16
c_8	21.41 $\pm$ 39.03	37.43 $\pm$ 29.15
χ^2	50	72
ndf[a]	62	62

[a]ndf = number of degrees of freedom

Table A.8: Sanford-Wang parameters and errors obtained by fitting the π^++C dataset.

Parameter	π^-	π^+
c_1	52.24 ± 162.85	87.22 ± 165.98
c_2	1.88 ± 1.97	1.35 ± 1.49
c_3	0.94 ± 1.96	0.95 ± 78.23
c_4	1.50 ± 0.60	0.87 ± 17.57
c_5	2.02 ± 0.56	1.20 ± 9.79
c_6	10.71 ± 6.65	6.10 ± 4.59
c_7	0.18 ± 0.19	0.30 ± 0.29
c_8	7.73 ± 28.64	43.44 ± 50.36
χ^2	20	15
ndf[a]	28	28

[a]ndf = number of degrees of freedom

Table A.9: Sanford-Wang parameters and errors obtained by fitting the π^-+C dataset.

Parameter	π^-	π^+
c_1	117.17 ± 8.00	44.81 ± 38.07
c_2	1.14 ± 0.05	1.57 ± 0.51
c_3	0.0004 ± 88.46	0.11 ± 4.37
c_4	0.30 ± 98.91	4.83 ± 6.35
c_5	1.63 ± 50.29	3.22 ± 4.37
c_6	5.71 ± 0.33	9.08 ± 1.96
c_7	0.26 ± 0.01	0.26 ± 0.08
c_8	38.85 ± 4.93	27.24 ± 13.19
χ^2	87	101
ndf[a]	28	28

[a]ndf = number of degrees of freedom

Bibliography

[1] T. Antoni *et al.* (KASCADE Collab.), Nucl. Instrum. Meth. A513 (2003) 490.

[2] J. Abraham *et al.* (Pierre Auger Collab.), Nucl. Instrum. Meth. A523 (2004) 50.

[3] T. Antoni *et al.* (KASCADE Collab.), Astropart. Phys. 24 (2005) 1 and astro-ph/0505413.

[4] D. Heck, J. Knapp, J. Capdevielle, G. Schatz, and T. Thouw, Wissenschaftliche Berichte FZKA 6019, Forschungszentrum Karlsruhe, 1998.

[5] J. Blümer, R. Engel, and J. R. Hörandel, "Cosmic rays from the knee to highest energies", to be published in "Progress in Part. and Nucl. Phys.", 2007.

[6] A. M. Hillas, J. Phys. G31 (2005) R95.

[7] H. Völk and E. Berezhko, Astron. and Astroph. 451 (2006) 981.

[8] S. G. Lucek and A. R. Bell, Mon. Not. R. Astron. Soc. 314 (2000) 65.

[9] A. M. Hillas, Ann. Rev. Astron. Astrophys. 22 (1984) 425.

[10] J. Blümer and K. H. Kampert, Physikalische Blätter 56 (2000) 3.

[11] R. Engel, Nucl. Phys. B (Proc. Suppl.) 151 (2006) 437–461 and astro-ph/0504358.

[12] H. Ulrich *et al.* (KASCADE Collab.), Eur. Phys. J. C33 (2004) 944.

[13] A. Haungs *et al.* (KASCADE-Grande Collab.), Czech. J. Phys. 56 (2006) A 241 Proc. of XIV ISVHECRI 2006, Weihai, China.

[14] P. Sommers (Pierre Auger Collab.), astro-ph/0507150 Proc. of 29th ICRC, Pune, India, 3-11 Aug 2005, p. 387.

[15] A. De Rujula, Nucl. Phys. B (Proc. Suppl.) 165 (2007) 93 and hep-ph/0608092.

[16] M. Nagano and A. A. Watson, Rev. Mod. Phys. 72 (2000) 689.

[17] K. Greisen, Phys. Rev. Lett. 16 (1966) 748.

[18] G. T. Zatsepin and V. A. Kuzmin, Pis'ma Zh. Eksp. Teor. Fiz. 4 (1966) 114.

[19] W. Yao *et al.* (Particle Data Group Collab.), J. Phys. G33 (2006) 1.

[20] M. Risse, Acta Phys. Polon. B35 (2004) 1787 and astro-ph/0402300.

[21] H. Fesefeldt, report PITHA-85/02, RWTH Aachen, 1985.

[22] N. N. Kalmykov, S. S. Ostapchenko, and A. I. Pavlov, Nucl. Phys. B (Proc. Suppl.) 52B (1997) 17.

[23] R. S. Fletcher, T. K. Gaisser, P. Lipari, and T. Stanev, Phys. Rev. D50 (1994) 5710.

[24] R. Engel, T. K. Gaisser, P. Lipari, and T. Stanev, Proc. of the 26th Int. Cosmic Ray Conf. (Salt Lake City) vol. 1, p. 415, 1999.

[25] A. Fasso, A. Ferrari, J. Ranft, and R. P. Sala, in Proc. of Int. Conf. on Advanced Monte Carlo for Radiation Physics, Particle Transport Simulation and Applications (MC 2000), Lisbon, Portugal, 23-26 Oct 2000, A. Kling, F. Barao, M. Nakagawa, L. Tavora, P. Vaz eds., Springer-Verlag Berlin, p. 955, 2001.

[26] J. Blümer *et al.* (Pierre Auger Collab.), Proc. of the 28th Int. Cosmic Ray Conf.(Tsukuba, 2003) p415.

[27] T. Abu-Zayyad *et al.* (HiRes-MIA Collab.), Phys. Rev. Lett. 84 (2000) 4276 and astro-ph/9911144.

[28] H.-J. Drescher and G. R. Farrar, Astropart. Phys. 19 (2003) 235 and hep-ph/0206112.

[29] D. Heck *et al.*, Proc. of 28th Int. Cosmic Ray Conf. (2003), Tsukuba, Japan, 31 Jul - 7 Aug 2003, p. 279.

[30] National Aeronautics and Space Administration (NASA), NASA-TM-X-74335, 1976.

[31] W. Nelson, H. Hirayama, and D. W. O. Rogers, SLAC-265, Stanford Linear Accelerator Center, 1985.

[32] M. Bleicher *et al.*, J. Phys. G: Nucl. Part. Phys. 25 (1999) 1859.

[33] J. N. Capdevielle, J. Phys. G: Nucl. Part. Phys. 15 (1989) 909.

[34] S. Ostapchenko, Phys. Lett. B636 (2006) 40 and hep-ph/0602139.

[35] S. Ostapchenko, Phys. Rev. D74 (2006) 014026 and hep-ph/0505259.

[36] S. Roesler, R. Engel, and J. Ranft, in Proc. of Int. Conf. on Advanced Monte Carlo for Radiation Physics, Particle Transport Simulation and Applications (MC 2000), Lisbon, Portugal, 23-26 Oct 2000, A. Kling, F. Barao, M. Nakagawa, L. Tavora, P. Vaz eds., Springer-Verlag Berlin, p. 1033-1038 (2001), 2000.

[37] S. Ostapchenko, T. Thouw, and K. Werner, Nucl. Phys. B (Proc. Suppl.) 52B (1997) 3.

[38] V. N. Gribov, Sov. Phys. JETP 26 (1968) 414.

[39] Application Software Group, CERN Program Libary Long Writeup W1013, CERN, Genf, 1994.

[40] R. J. Glauber and G. Matthiae, Nucl. Phys. B 21 (1970) 135.

[41] C. Meurer, J. Blümer, R. Engel, A. Haungs, and M. Roth, Czech. J. Phys. 56 (2006) A211 and astro-ph/0512536.

[42] C. Meurer, J. Blümer, R. Engel, A. Haungs, and M. Roth, Proc. of 29th Int. Cosmic Ray Conf. (Pune, India) vol. 9, p. 17, astro-ph/0506755, 2005.

[43] C. Meurer, J. Blümer, R. Engel, A. Haungs, M. Roth, and HARP Collab., astro-ph/0612157 Proc. of ISVHECRI2006, to appear in Nucl. Phys. B (Proc. Suppl.).

[44] D. Dekkers *et al.*, Phys. Rev. 137 (1965) B962.

[45] J. V. Allaby *et al.*, CERN Yellow Report 70-12, 1970.

[46] T. Eichten *et al.*, Nucl. Phys. B44 (1972) 333.

[47] D. Antreasyan *et al.*, Phys. Rev. D19, N3 (1979) 764.

[48] W. F. Baker *et al.*, Phys. Rev. Lett. 7 (1961) 101.

[49] Y. Cho *et al.*, Phys. Rev. D4 (1971) 1967.

[50] G. Ambrosini *et al.* (SPY Collab.), Phys. Lett. B425 (1998) 208.

[51] G. Collazuol, A. Ferrari, A. Guglielmi, and P. R. Sala, Nucl. Instrum. Meth. A 449 (2000) 609.

[52] D. S. Barton *et al.*, Phys. Rev. D27 (1983) 2580.

[53] M. G. Catanesi *et al.* (HARP Collab.), CERN-SPSC-99-35, 1999.

[54] S. Afanasev *et al.* (NA49 Collab.), Nucl. Instrum. Meth. A430 (1999) 210.

[55] N. Antoniou *et al.* (NA61 Collab.), CERN-SPSC/2006-001 and SPSC-I-235, 2006.

[56] C. Alt *et al.* (NA49 Collab.), Eur. Phys. J. C49 (2007) 897 and hep-ex/0606028.

[57] C. Garabatos *et al.* (ALICE Collab.), Nucl. Instrum. Meth. A535 (2004) 197.

[58] R. Esteve Bosch *et al.* (ALICE Collab.), Prepared for 8th Workshop on Electronics for LHC Experiments, Colmar, France, 9-13 Sep 2002.

[59] R. Raja, hep-ex/0501005, 2005.

[60] http://ppd.fnal.gov/experiments/e907/.

[61] M. G. Catanesi *et al.* (HARP Collab.), Proposal to study hadron production for the neutrino factory and atmospheric neutrino flux, CERN-SPSC/99-35, 1999.

[62] B. Autin and A. Blondel, (Eds.), CERN 99-02, ECFA 99-197, 1999.

[63] S. Ozaki *et al.*, (Eds.), Feasibility Study-II of a Muon-based Neutrino Source, Report BNL-52623, 2001.

[64] A. Blondel *et al.*, CERN-2004-02, ECFA/04/230, 2004.

[65] M. Alsharoa *et al.*, Phys. Rev. ST. Accel. Beams 6 (2003) 081001.

[66] T. K. Gaisser and M. Honda, Ann. Rev. Nucl. Part. Sci. 52 (2002) 153 and hep-ph/0203272.

[67] Y. Fukuda *et al.* (Super-Kamiokande Collab.), Phys. Rev. Lett. 81 (1998) 1562 and hep-ex/9807003.

[68] Y. Fukuda *et al.* (Super-Kamiokande Collab.), Phys. Rev. Lett. 82 (1999) 2644 and hep-ex/9812014.

[69] G. Battistoni, Nucl. Phys. B (Proc. Suppl.) 100 (2001) 101.

[70] T. Stanev, AIP Conference Proceedings 516 (2000) 247 Prepared for 26th International Cosmic Ray Conference (ICRC 99), Salt Lake City, Utah, 17-25 Aug 1999.

[71] T. K. Gaisser, Nucl. Phys. B (Proc. Suppl.) 87 (2000) 145 and hep-ph/0001027.

[72] R. Engel, T. K. Gaisser, and T. Stanev, Phys. Lett. B472 (2000) 113 and hep-ph/9911394.

[73] M. Honda, Nucl. Phys. B (Proc. Suppl.) 77 (1999) 140–145 and hep-ph/9811504.

[74] H. L. Ray (MiniBooNE Collab.), hep-ex/0701040 (2007).

[75] K. Hiraide (SciBooNE Collab.), Nucl. Phys. B (Proc. Suppl.) 159 (2006) 85.

[76] M. H. Ahn *et al.* (K2K Collab.), Phys. Rev. Lett. 90 (2003) 041801 and hep-ex/0212007.

[77] T. K. Gaisser *et al.*, Phys. Rev. D54 (1996) 5578 and hep-ph/9608253.

[78] R. Engel, Nucl. Phys. Proc. Suppl. 122 (2003) 437 and hep-ph/0212340.

[79] A. Haungs, L. W. Jones, and H. Rebel, NEEDS Workshop, Karlsruhe April 18 - 20, 2002, http://www-ik.fzk.de/ needs/, 2002.

[80] M. G. Catanesi *et al.* (HARP Collab.), Nucl. Instrum. Meth. A571 (2007) 527.

[81] M. G. Catanesi *et al.* (HARP Collab.), Nucl. Phys. B 732 (2006) 1.

[82] J. Altegoer *et al.* (NOMAD Collab.), Nucl. Instrum. Meth. A428 (1999) 299.

[83] A. Großheim, “Particle production yields induced by multi-GeV protons on nuclear targets”, Ph.D. thesis, University of Dortmund, Germany, CERN-THESIS-2004-010, 2004.

[84] M. G. Catanesi *et al.* (HARP Collab.), Nucl. Instrum. Meth. A572 (2007) 899.

[85] M. G. Catanesi *et al.* (HARP Collab.), hep-ex/0702024.

[86] G. D’Agostini, DESY 94-099, ISSN 0418-9833, 1994.

[87] V. Blobel and E. Lohrmann, ”Statistische und numerische Methoden der Datenanalyse”, Stuttgart: Teubner, 1998, ISBN 3-519-03243-0.

[88] S. Agostinelli *et al.* (GEANT4 Collab.), Nucl. Instrum. Meth. A506 (2003) 250.

[89] M. G. Catanesi *et al.* (HARP Collab.), “Measurement of production of charged pions by protons on a tantalum target”, in preparation (2007).

[90] C. Meurer, J. Blümer, R. Engel, A. Haungs, M. Roth, and HARP Collab., AIP Conf. Proc.(2006), vol. 896, p 158.

[91] J. R. Sanford and C. L. Wang, Brookhaven National Loboratory, AGS internal report (1967).

[92] J. Panman, private communication (2007).

Acknowledgements

I am indebted to Prof. Dr. J. Blümer for giving me the opportunity to work on my Ph.D. at the Forschungszentrum Karlsruhe, for supporting my work in many ways and for giving me the possibility to present the results of my work at several conferences.

Many thanks to Prof. Dr. G. Quast for taking over the report as co-referee and for interesting discussions during my teaching assistance for an undergraduate lab-class on physics at the University of Karlsruhe.

I would like to express my deep gratitude to Dr. R. Engel for guiding me through the course of this thesis and for always supporting my activities.

I am very grateful to Dr. J. Panman for giving me the opportunity to join the HARP collaboration, for working together on the data analysis and for teaching me a lot during the many weeks I stayed at CERN in the last year.

I thank Dr. A. Großheim for introducing me to the unfolding method of the HARP data analysis.

I am grateful to Dr. A. Haungs and Dr. M. Roth for many fruitful discussions.

I am thankful to Dr. D. Heck for help with modifying CORSIKA to include the muon ancestor information.

Many thanks to my roommates Dr. T. Pierog and T. Bergmann for the very pleasant working atmosphere during the last three years.

I am thankful to the members in my department: Dr. B. Keilhauer, Dr. H. Klages, I. Maris, K. Mora, A. Obermeier, T. Schmidt, F. Schüssler, Dr. H. Ulrich, R. Ulrich, Dr. M. Unger, Dr. J. Van Buren, Dr. T. Waldenmaier and all others for helping me in one way or the other during my thesis.

I also wish to express my gratitude to all members of the HARP collaboration, NA61

collaboration, KASCADE collaboration and of the Auger collaboration.

Last, and most important, special thanks to my parents and my boy-friend T. Aßmus for supporting me in many ways during my Ph.D. time, for being good friends at my side and for many, many beautiful moments.